Faculty of Science and Engineering

Department of Electrical and Electronic Engineering

Magnetic Equivalent Circuit Approach for AC Copper Loss Calculation and Optimal Winding Design for Electrical Machines

by

Yixiang Yuan, M.Sc.

Thesis submitted to the University of Nottingham for the degree of

Doctor of Philosophy

Supervised by

Prof. He Zhang

A/Prof. Xiaochen Zhang

Prof. David Gerada

October 2024

Abstract

The rapidly growing interest in aircraft electrification, known as more electric aircraft (MEA), has propelled the development of high-power-density machines, which are characterized by high-speed or high pole-pair number. These machines inherently encounter significant AC copper losses due to the high frequency of input voltage. The AC copper loss in electrical machines refers to the additional copper losses in the windings that occur due to alternating current (AC) effects, which are not present under direct current (DC) conditions. This phenomenon will not only cause partial overheating in the winding but also accelerate insulation aging, ultimately resulting in additional challenges in thermal dissipation or winding failure, which severely restricted the further improvement of power density of an electrical machine.

To reduce the burden on thermal management systems and increase the power density of electrical machines, various techniques for mitigating AC copper loss have been extensively studied, especially for innovative winding structures. However, the current solutions are not sufficiently satisfactory. For example, litz wire can effectively reduce the AC copper loss up to several kHz, at the cost of low copper filling factor and high manufacturing price, which severely restricts its further application in electrical machines.

In addition, a novel winding structure using transposed rectangular bundle with rectangular conductors and its design procedure are proposed to provide another optimal solution for high power density machines. The proposed winding can effectively reduce the AC copper loss in electrical machines without

significantly compromising slot fill factor, thus enhancing power density.

The thesis comprises the following contributions:

1) **Proximity Loss Calculation Method**: Based on mesh-based magnetic equivalent circuit (M-MEC), a novel method is proposed to calculate the proximity loss and magnetic flux leakage according to precise slot positions of the conductors in electrical machines. This method demonstrates high flexibility and can be extended to accommodate slots of various shapes. Using an existing machine as an example, the modelling process of the proposed method is illustrated, showing close alignment and efficiency compared with FEA. Experimental tests on a motorette further validate the effectiveness of the proximity loss calculation method.

2) **Circulating Current Loss Calculation Method:** Based on the flux leakage calculation method mentioned above, a rapid circulating current calculation method is introduced. This method involves the electrical circuit of each strand and calculating parameters using M-MEC. The process is illustrated with a baseline machine, demonstrating shorter computation times and comparable precision to FEA. Experimental validation on a motorette further confirms the validity of the circulating current loss calculation method.

3) **Innovative Winding Structure**: A new winding structure aiming at reducing AC copper loss in high-frequency electrical machines is presented. This winding can suppress circulating current loss without significantly compromising slot fill factor. The optimization process, involving the calculation of circulating current loss for form-wound windings with different

strand numbers and transpositions, is illustrated on the baseline machine. Experimental results validate the effectiveness of the optimized winding in reducing circulating current loss.

Key words: High power density machines, flux leakage, mesh-based magnetic equivalent circuit (M-MEC), AC copper loss, proximity, circulating current, winding design.

Research Achievements

During my Ph.D., I published one journal article and one conference paper, applied for a patent invention. The research achievements are detailed below.

Published article:

1. **Y. Yuan**, M. A. Darmani, Y. Bao, X. Zhang, D. Gerada and H. Zhang. "Analysis of Proximity Loss of Electrical Machines Using Mesh-Based Magnetic Equivalent Circuit." *IEEE Transactions on Transportation Electrification*, 2024, early access. **(SCI, JCR Q1, IF: 7)**

2. **Y. Yuan**, M. A. Darmani, Y. Bao, X. Zhang, D. Gerada and H. Zhang. "Fast Calculation of Proximity Loss Induced by Harmonic Current in Electrical Machines Using Magnetic Equivalent." In 27th *IEEE International Conference on Electrical Machines and Systems*, IEEE, 2024. (Accepted)

Patent:

1. He Zhang, Xiaochen Zhang, Jing Li, Xiaoyan Huang, Yuanli Kang, and **Yixiang Yuan**. "Insulation failure detection and positioning method for aviation motor", CN116593833A, Chinese invention patent, Issued patent.

Acknowledgement

First and foremost, I would like to express my gratitude to my supervisors, Professor He Zhang, Dr. Xiaochen Zhang, Professor David Gerada, and Dr. Mostafa Ahmadi Darmani. Professor He Zhang is not only rich in professional knowledge and has a broad vision, but he also provides guidance that always gets straight to the point. What is more important is, he respects his students and always prioritizes their development. Dr. Xiaochen Zhang's deep understanding of electric machines and attention to detail are truly impressive. His philosophical insights into electric machines and continuous guidance in writing have been invaluable to me. Professor David Gerada is highly knowledgeable and gave me the initial opportunity to pursue my PhD at the University of Nottingham, providing patient guidance throughout the process. Dr. Mostafa Ahmadi Darmani offered tremendous assistance with writing, from whom I learned almost all my skills and ideas to academic writing. During my exchange period in the UK, he warmly helped me adapt quickly to life there. The experience of pursuing my PhD has been a precious treasure in my life, and I am deeply grateful to all my supervisors.

I would like to thank Dr. Yuli Bao, Dr. Weiduo Zhao, and Dr. Yatai Ji, whose help compensated for my lack of experimental experience and enabled me to solve many unexpected problems in the experiments. Without you, I would have spent more time and faced more setbacks in the lab. I am also grateful to Dr. Yinli Wang and Dr. Xiaocheng Wei, whose discussions with me about the research topics pointed out shortcomings in my ideas, and I benefited greatly

from it.

Finally, I want to thank my parents. They have always supported me and given me the freedom to focus on my PhD studies without any distractions. Without your support, I would not have achieved the success I have today. A significant part of my achievements can be attributed to you. I really appreciate it.

Table of Contents

List of Figures

XII

List of Tables

Chapter 1 Introduction

1.1 Research Background

1.1.1 More Electric Aircraft (MEA)

The aviation market has been growing rapidly in recent years. Along with the rapid development, the emission of greenhouse gas have also increased significantly. Each year, the aviation industry produces more than 900 million metric tons of CO2, accounting for 2%-2.5% of global CO2 emissions [1]. The overall effect of aviation industry on global warming, as it is quantified in [2], accounts for 3.5% among all different industries.

The amount of carbon dioxide generated in the aviation industry is enormous, and it is likely to continue growing in the future. According to Japan Aircraft Development Corporation, greenhouse gas generated from aviation industry in 2040 is projected to be 2.1 times higher than those in 2019 [3]. This projection aligns with the prediction by Airbus Corporation that the global number of aircraft in 2037 will double compared to 2018 [4].

It is evident that reducing greenhouse gas emissions in the aviation industry is crucial for decreasing overall emissions. In this context, the concept of More Electric Aircraft (MEA) was proposed and has gained increasing attention and popularity from the research community since the 1990s [5]. In an MEA, sub-systems such as hydraulic, pneumatic, and mechanical systems are replaced by electrical systems, thereby eliminating several energy conversion processes [6]. As a result, greenhouse gas emissions are significantly reduced in MEAs

compared to conventional aircraft. The European-funded Power Optimized Aircraft (POA) project demonstrated that MEAs can reduce non-propulsive power consumption by more than 35% [7] and total power consumption by 9% [8]. The Boeing 787 Dreamliner, with the MEA initiative and a much higher electrical load than Airbus 320, achieved significantly lower energy consumption per passenger [9]. Moreover, the overall mass of an MEA is also lower than that of conventional aircraft, resulting in maintenance cost savings due to the elimination of bleed systems, which previously accounted for a significant portion of maintenance costs [10].

There are numerous benefits for the MEA compared to conventional aircrafts, and MEAs are believed to have the potential to revolutionize the aviation industry [11]. Consequently, there has been a dramatic surge in research on MEAs in recent years, along with growing public interest and investment in advancing this innovative technology.
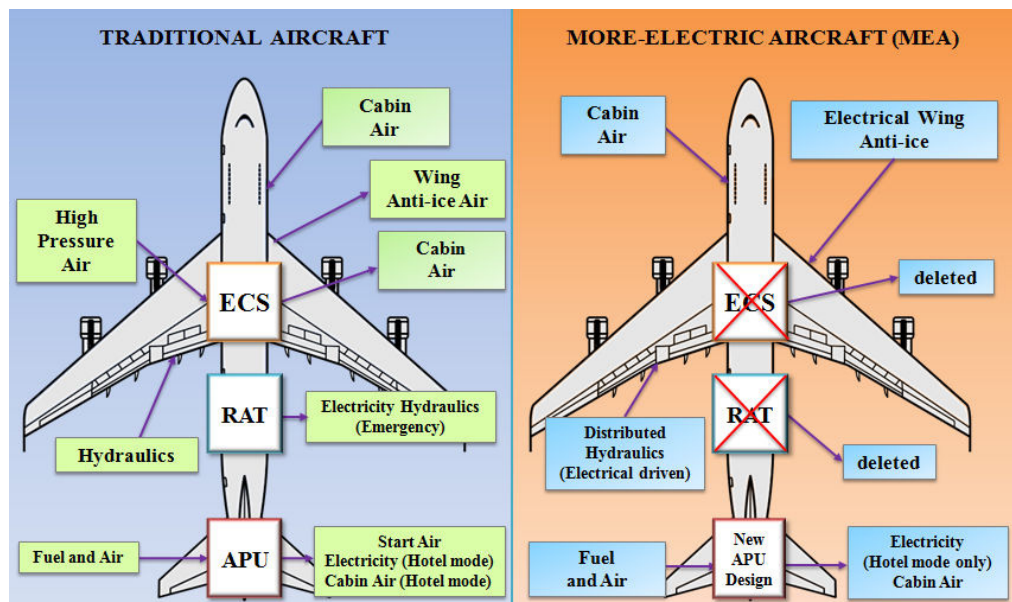
Figure 1.1 Comparison of a Conventional Aircraft and More Electric Aircraft [12]

1.1.2 High Power Density Electrical Machines in MEA

The electrical machines are one of the most important components in MEAs. Besides the strict reliability and safety requirement, high power density is also a crucial feature for electrical machines in MEAs due to the limited space and load capacity of aircraft. Although the definition of power density of an electrical machine may differ among different organizations and manufacturers, it is undeniable that the most essential requirement to achieve higher level of aircraft electrification is to enhance the power density of the drive system, where the electrical machine constitutes a significant part of the weight [13].

Goals of power density of the electrical machines have been presented by various organizations related to aviation industry. Taking the propulsion system as an example, the power density requirements of the electrical systems, comprising electrical machines and power electronics, are discussed and reported by the National Academies of Sciences, Engineering, and Medicine (NASEM), as illustrated in Table 1.1.

Table 1.1 Power density requirements for the electrical propulsion system in various aircraft types and architectures [14]

Aircraft type	Aircraft Architecture	Power density (kW/kg)
General aviation and commuter	Parallel hybrid	>3.0
	Turbo-electric	>6.5
Regional and single aisle	Parallel hybrid	>3.0
	Turbo-electric	>6.5
Twin aisle	Turbo-electric	>10

In addition to NASEM, other organizations and companies have also presented their future plans for high power density electrical machine to achieve aircraft electrification. The power density goals of the electrical machines set by different organizations are shown in Table 1.2.

Table 1.2 Power density goal of the electrical machine for aviation electrification [15]

Organization	Goal power density	Time to achieve
NASA	13 kW/kg	10 years
	16 kW/kg	15 years
U.S. Air Force	5 kW/kg	20 years
Airbus	10–15 kW/kg	15 years

Despite the ambitious power density objectives, the power density of the most advanced propulsion machine significantly falls far below the target value. As is illustrated in Figure 1.2, the power density of most electrical machines is below 6 kW/kg. For the electrical machines which reach a power density of more than 6 kW/kg, complicated cooling systems are adopted, and the weight of cooling device is not taken into account.
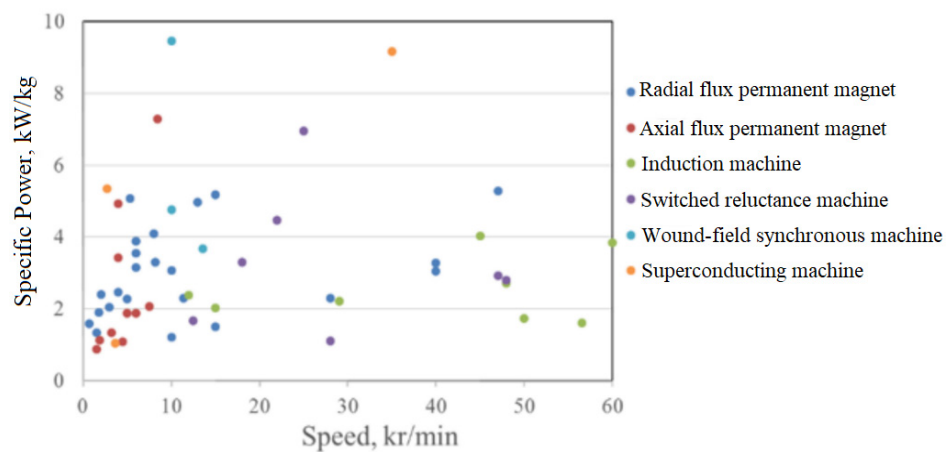
Figure 1.2 Power density of the propulsion machines for aircrafts [16]

As demonstrated, the power density of the state-of-art electrical machines significantly lags behind the set goals. There is an urgent need for substantial enhancement in power density of these machines to fulfill the demands of higher level of aircraft electrification.

1.1.3 Losses in Electrical Machines

Losses in electrical machines are critical because of their influence on efficiency, operational costs, thermal management and reliability. For high power density machines, these losses are even more important because low efficiency can lead to unexpected heat and increased operating temperature. The situation requires more robust cooling systems, which can be costly and complex. The device of the cooling system will dramatically reduce the overall power density of the overall system. Additionally, excessive heat can degrade insulation materials and other components, potentially leading to premature failure. Therefore, improving the reliability, durability, and efficiency of electrical machines by understanding and mitigating losses is essential.

Generally, the power losses in electrical machines are composed of following components [17]:

1) Copper losses: Losses that occur in the stator (armature) and rotor (field) windings of the machines.

2) Core losses: Losses occur in the magnetic core of the machine due to the alternating magnetic field.

3) Mechanical losses: Losses associated with mechanical effects such as friction and windage.

4) Additional losses: The losses which cannot be placed in one of the previous categories.

Among these losses, copper losses are more directly related to the operational load and have an evident impact on thermal management design [18]. Therefore, mitigating copper loss is one of the most effect techniques to enhance the power density of electrical machines, highlighting the importance of research in this area.

1.1.4 Copper Losses

The mitigation of AC copper loss remains challenging and has been the focus of extensive recent research because it is prominent and seriously limiting further improvements in power density. AC copper loss significantly impacts on the electrical machine in two key areas: efficiency and thermal management. For high frequency machines, AC copper loss dramatically reduces efficiency. It is reported that with improper winding, AC copper could be more than 5 times larger than DC copper loss in an electrical machine, and subsequently decreasing the efficiency by more than 1.2% [19]. Another example is demonstrated in [20], which shows that AC copper loss takes a portion of 1% of the overall input energy when the electrical machine in that paper is working at its rated power with 336 W DC copper loss.

Additionally, AC copper loss complicates the thermal management of the high power density machines, particularly in the MEAs. In high power density machines, the losses are relatively high in a small volume with reduced thermal capacity, imposing strict requirements on the thermal management system [21].

6

An example illustrating this point is provided in Figure 1.3, which shows the temperature distribution at different operating states of the same electrical machine. The outer diameter of the interior permanent magnet 8-pole 24-slot machine is 355 mm, and its maximum rotating speed is 15,000 rpm.
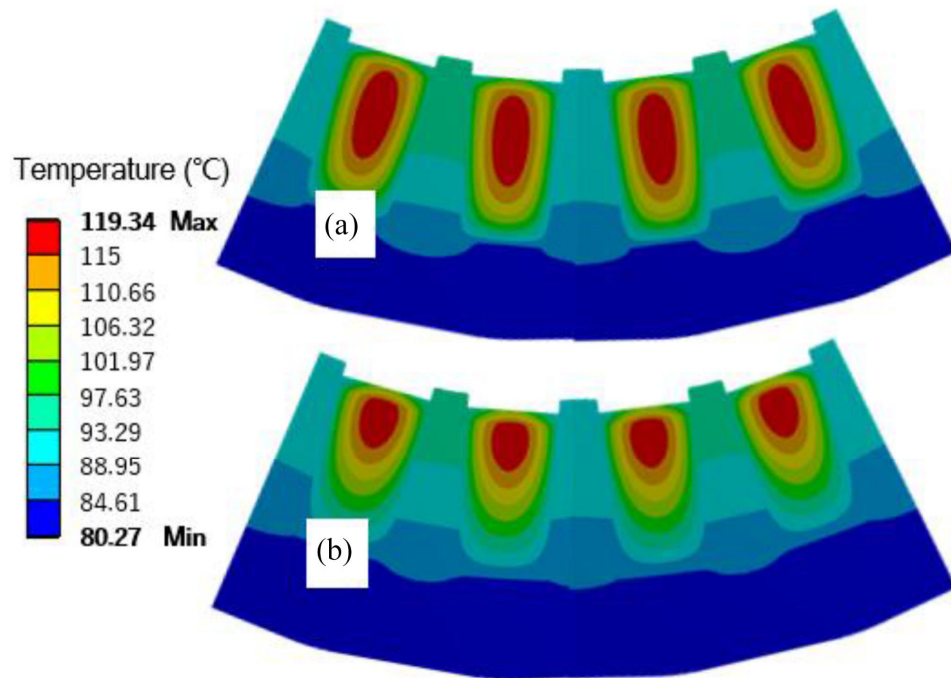
Figure 1.3 Position of the hotspots of a high power density machine at different operating state. (a) $f = 200$ Hz, $I_m = 14$ Arms. (b) $f = 800$ Hz, $I_m = 8$ Arms. [22]

At an operating frequency of 200 Hz, AC copper loss is relatively small, resulting in a more evenly distributed temperature within the slot. The input current that reaches the maximum temperature under this condition is 14 Arms. However, when the machine operates at 800 Hz, AC copper loss significantly increases, leading to a highly uneven temperature distribution, particularly near the slot opening. Furthermore, the input current required to reach the same maximum temperature at 800 Hz is only 8 Arms, substantially less than the 14 Arms needed at 200 Hz. By comparing these two operating conditions, it is evident that with the same thermal management system, the input current at 800

Hz is significantly restricted due to the AC copper loss. Conversely, if the input current remains constant at both operating frequencies, the thermal load at 800 Hz is considerably higher due to the AC copper loss.

In summary, it is crucial to mitigate AC copper losses in high power density electrical machines to improve their efficiency and thermal management. Addressing these losses is essential for enhancing the performance and reliability of these machines, particularly in applications like MEAs, where space and thermal constraints are significant.

1.2 Research Objectives

The overall aim of this thesis is to propose a novel winding for high power density machines that minimize AC copper loss. To achieve this optimization, a rapid calculation method for AC copper loss is necessary because extensive computation for various winding structures is required, and using Finite Element Analysis (FEA) is very time-consuming. To develop a rapid calculation method on AC copper loss, it is necessary to establish rapid calculation approaches for its primary components, i.e. proximity effect and circulating current (skin effect is excluded, as it is negligible in most electrical machines under 1400 Hz). Following this, the utilization of the developed method should be explored for winding optimization design aiming at AC copper loss minimization.

Based on the discussion above, in this context, the following objectives have been identified:

(1) Objective 1:

The thesis aims to develop a rapid calculation method for proximity loss in

electrical machines, taking into account the precise position of the conductors, the size of the conductors, and the shape of the slot.

(2) Objective 2:

The thesis intends to propose a swift calculation method for circulating current loss in electrical machines, considering the precise position of the conductors, the impact of the rotor, and different winding connections.

(3) Objective 3:

The thesis further explores a novel winding structure, which can effectively mitigate AC copper loss for the electrical machines at approximately 1000 Hz operating frequency. The winding should be designed to reduce AC copper loss through precise transposition instead of compromising the slot fill factor.

1.3 Thesis Outline

This section presents the overall structure of the thesis, briefly outlining the main content and key innovations of each chapter as follows.

1) Chapter 1: Introduction

This chapter introduces the research background, research objectives, and the research roadmap of the thesis.

2) Chapter 2: Literature review

In this chapter, an introduction on losses in electrical machine is presented, followed by a detailed literature review of AC copper loss calculation methods and the wire technologies.

3) Chapter 3: Swift proximity loss calculation method

This chapter introduces the calculation method for proximity loss in

electrical machines using the MEC. Several cases are calculated using MEC and FEA for validation, along with an experiment.

4) Chapter 4: Analytical model on circulating current loss calculation

This chapter presents an analytical model for circulating current loss. The method is applied to an existing high-speed electrical machine, and the calculation results for strand inductances, back-EMF of each strand, and strand current are compared with FEA. An experiment is also conducted to validate the method.

5) Chapter 5: Optimization design of the low AC copper loss winding

This chapter presents a novel winding structure designed to suppress AC copper loss through precise transposition, without compromising the slot fill factor. Based on the analytical methods presented in Chapters 3 and 4, the optimization process is discussed in detail, and the AC copper loss of various winding structures is calculated. The copper loss of the optimized winding is validated through both FEA and experiment.

6) Chapter 6: Conclusion

This chapter summarizes the key findings of the thesis and recommends potential future research directions.

Chapter 2 Literature Review

As discussed in the previous chapter, researching techniques to mitigate losses is crucial for enhancing the power density of electrical machines. Among these losses, copper loss is particularly significant because it constitutes a large portion of the total losses and directly affects the cooling system and insulation aging. Therefore, there is considerable potential for improving the power density of electrical machines by reducing copper losses.

To achieve the objective of reducing copper losses in electrical machines through novel winding designs, two major challenges must be addressed. The first challenge is the development of a swift and accurate calculation method. This is essential because the winding design process requires the estimation of AC copper losses for numerous different winding structures. Accurate estimation methods are vital to ensure that the design process is both efficient and reliable.

The second challenge is identifying the proper winding techniques to implement the designed winding into the electrical machine. Various winding technologies have been explored in the literature, including different winding structures and the use of advanced materials. The advantages and limitations of these techniques are evaluated comprehensively to identify the most suitable technique as the basis for winding optimization calculation.

Based on the discussion above, the literature review is organized as follows:

1) Introduction to the Losses in Electrical Machines. This section provides an overview of different types of losses in electrical machines, including the physics law and a brief introduction on the estimation method.

2) Calculation Methods for AC Copper Losses. This part investigates various rapid calculation methods for AC copper losses in electrical machines, evaluating the advantages and flaws of these methods.

3) Winding Technologies. This section reviews advanced winding technologies for AC copper loss reductions, in addition to the wires with the potential to be used as the foundation for optimized winding designs.

2.1 Losses in Electrical Machines

2.1.1 Copper Losses

The copper losses are composed of two components: DC copper loss and AC copper loss, and they are introduced separately in the following content.

1) DC copper loss

When an electric current flows through a conductor, heat will be generated consequently. The heat is known as Joule loss or copper loss. The power of heat is expressed in an integral form:

$$P_{\text{Joule}} = \iiint_V \rho |J|^2 \, \mathrm{d}V \tag{2.1}$$

where

Symbol	Unit	Explanation
V	m^3	Volume of the conductor
ρ	$\Omega \cdot \text{m}$	Resistivity of the material
J	A/m^2	Current density at each point in the conductor

By assuming that the current density in the conductor is constant and the cross-section area of the conductor is a certain shape, equation (2.1) can be

simplified into:

$$P_{DC}=\rho|J|^2 V=|J|^2 A^2*\rho l/A= I^2 R_{DC} \tag{2.2}$$

where

Symbol	Unit	Explanation
P_{DC}	W	Power of DC copper loss
I	A	DC current which flows through the conductor
R_{DC}	Ω	DC resistance of the conductor

And the DC resistance is expressed as:

$$R_{DC}=\rho l/A \tag{2.3}$$

where

Symbol	Unit	Explanation
l	m	Conductor length defined along the direction of current flow
A	m^2	Cross section area of the conductor

2) AC Copper Loss

AC copper loss is defined as the specific loss in the conductor which only occurs when the winding is exposed in an alternating external magnetic field or an alternating current is injected into the winding. Generally, AC copper loss consists of three components: the skin effect, the proximity effect and circulating current [23], and their principles as introduced in the following.

(1) Skin Effect

Equation (2.2) is widely utilized to calculate the Joule loss of the conductor in various application scenarios. However, it is under the assumption that the current is evenly distributed in the conductor. This assumption is only feasible

13

when the input current is DC current or under conditions of low alternating current in the conductor. For high-speed electrical machines and high-pole-pair electrical machines, the current density inside the conductor is not constant. Under those circumstances, the Equation (2.2) is not applicable. The detailed current density distribution is required to calculate the copper loss.

Several factors can influence the current density distribution in the slot, one of which is the skin effect, as shown in Figure 2.1. Skin effect is defined as the phenomenon that the current tends to flow more along the outer surface of the conductor rather than through its entire cross-section area when the frequency increases [24]. An example of the uneven current density distribution due to skin effect of a single conductor is simulated in FEA is shown in Figure 2.2. It can be observed clearly that as the frequency of the AC current increases, the current density distribution becomes more unevenly distributed.
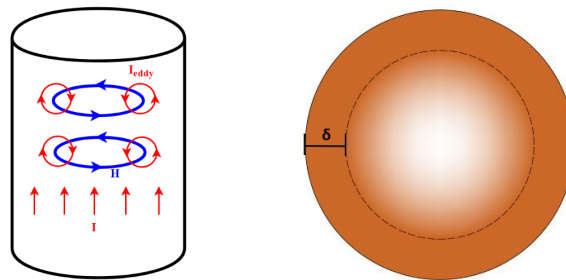
Figure 2.1 Law of skin effect [25]

(a)   (b)   (c)
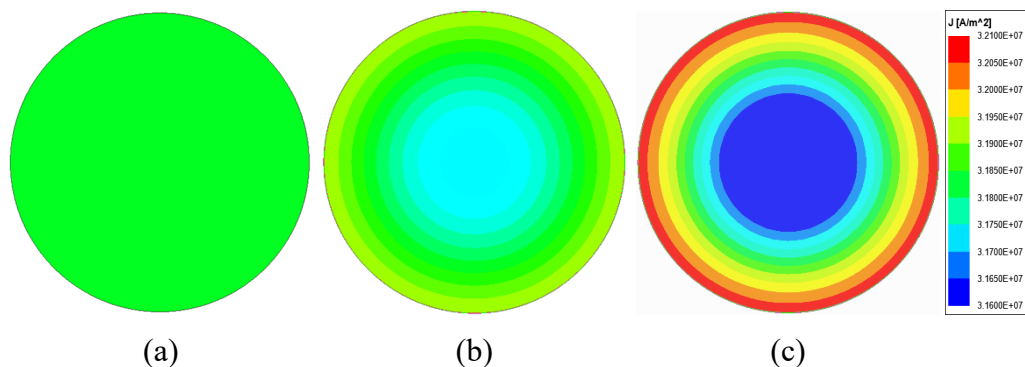
Figure 2.2 Uneven current density distribution in a conductor due to skin effect.
(a) 100Hz, 100 Arms; (b) 1000 Hz, 100 Arms; (c) 2000Hz, 100 Arms

Apparently, such phenomenon will cause a rise in effective resistance. One important index to measure the influence of the skin effect on resistance is skin depth, which is derived from [23]:

$$\delta = \sqrt{\frac{1}{\pi f \mu \sigma}} \qquad (2.4)$$

where

Symbol	Unit	Explanation
f	Hz	Frequency of sinusoidal current
μ	H/m	Permeability of the conductor
σ	S/m	Conductivity of the conductor

Skin depth is used to indicate the depth at which an electromagnetic wave's intensity inside a conductor decreases to $1/e$ (approximately 37%) of its value at the surface. As it is illustrated in equation (2.4), it is only relevant to the material type and the frequency of input current. Therefore, when the frequency is fixed, the ratio of effective resistance to DC resistance of round copper conductor can be written as a function of radius [26]:

$$\frac{R_{AC}}{R_{DC}} = 1 + \frac{1}{48}\left(\frac{a}{\delta}\right)^4 \qquad (2.5)$$

where a represents the radius of the conductor. Accordingly, the ratio of AC resistance to DC resistance of copper conductor of different radius at different frequencies is drawn in Figure 2.3.
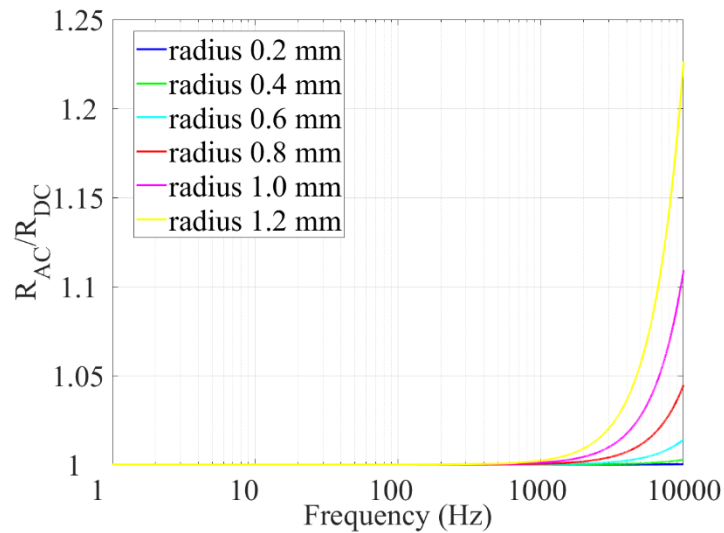
Figure 2.3 Ratio of AC resistance to DC resistance of different conductor radius

It is evident that under 1400 Hz, the AC resistance caused by skin effect is negligible, even for the conductor with large radius. Therefore, in most electrical machines, the skin effect loss is ignored, especially when the radius of the conductor is smaller than skin depth [27]. This is also the reason why corresponding rapid calculation method is not addressed in the thesis.

(2) Proximity

The physics phenomenon of proximity effect can also influence the current density distribution in the conductor in addition to skin effect. When there are conductors carrying current nearby or other magnetomotive force (MMF) source generating magnetic flux at a certain position, the current distribution of the conductor at this position will be influenced by the external magnetic flux. This phenomenon is described as proximity effect [28]. The physics law of proximity effect is illustrated in Figure 2.4, which depicts the influence of external magnetic flux on the current density within a conductor.
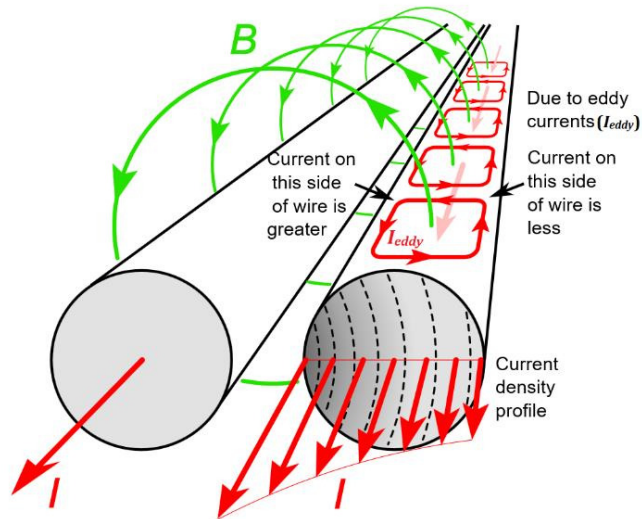
Figure 2.4 Physics law of proximity effect [24].

(a)

(b)
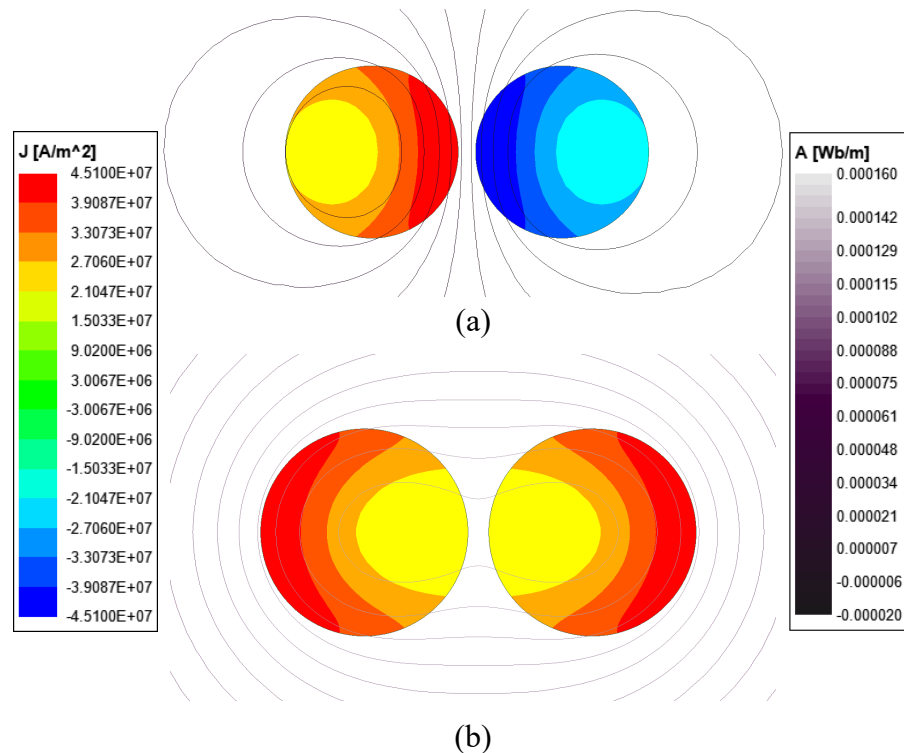
Figure 2.5 Current density distribution in the conductor due to proximity effect.
Current density in 2 conductors are in (a) opposite direction; (b) same direction

To further explain the influence of proximity effect, two adjacent conductors with flowing current is simulated in FEA, and the resultant magnetic flux and current density distribution is shown in Figure 2.5. It can be clearly observed that the current density is influenced by the external magnetic flux, and

the boundary of the map between different current density coincides with the magnetic flux to some extent.

Currently, the most commonly used equation to calculate proximity loss is presented in [29]. By assuming that the magnetic flux density is uniform in the conductor area, the proximity loss of a round conductor can be expressed as:

$$P_{\mathrm{p}}=\frac{\pi l\sigma d_0^{\,4}}{64}\left(\frac{dB_{\mathrm{ext}}}{dt}\right)^2 \tag{2.6}$$

where

Symbol	Unit	Explanation
d_0	m	Diameter of the conductor
B_{ext}	T	External magnetic flux density

(3) Circulating current

Circulating current is defined as the imbalanced current in the parallel-connected strands caused by imbalanced strand parameter such as inductance and resistance. Since the circulating current can be regarded as the imbalanced current distribution between the strands, which is similar to the definition of aforementioned proximity (uneven current distribution in the conductor), the circulating current is also regarded as a component of AC copper loss. In high power density electrical machines, the circulating current phenomenon is common because of their low number of turns and large strand number. The reason for the large strand number can be explained in the following equation [30]:

$$E=4.44fNk_pk_d\Phi \tag{2.7}$$

where

18

Symbol	Unit	Explanation
N		Number of turns of coil
k_p		Pitch factor of the coil
k_d		Distribution factor of the coil
Φ	Wb	Average magnetic flux per pole

In most power supply systems, the DC bus voltage is limited, which in turn limits back EMF E as described in equation (2.7). As the frequency increases, the number of turns in the coil decreases. If the coil is not divided into parallel strands, the conductor's cross-sectional area will be large, resulting in significant skin effect and proximity losses, as noted in [31]. Therefore, to mitigate these losses, a larger number of parallel strands is used. This approach can be interpreted as dividing one large solid conductor into several smaller conductors that are connected in parallel.
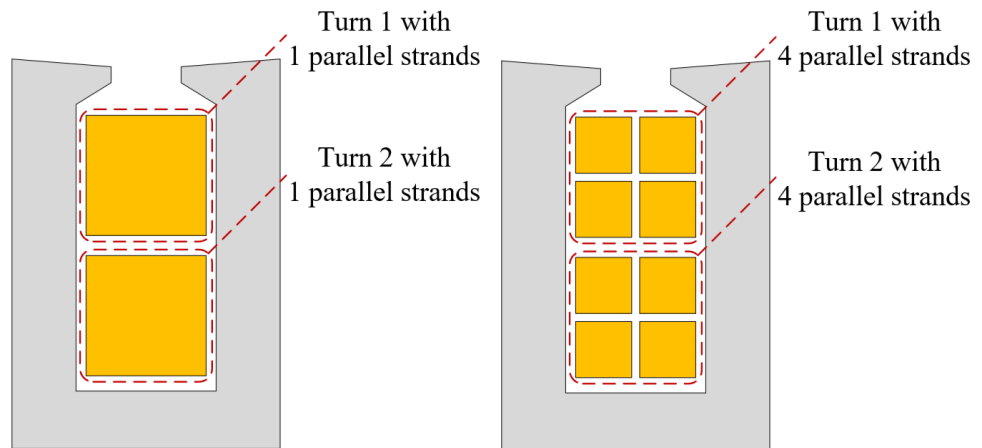
Figure 2.6 An example of separation on large conductor into 4 smaller conductors

To further illustrate the principle of circulating current, A FEA simulation on a slot is conducted to illustrate the phenomenon as it is shown in Figure 2.7. In the simulation, 2 conductors are placed in different positions in an iron core as shown in Figure 2.7 (a), and they are connected in parallel as indicated in

Figure 2.7 (b). The input current is 100 A at peak at 10000Hz. It can be clearly observed that the current in two conductors is very different, and additional Joule loss is generated compared with DC situations.

(a)   (b)

(c)
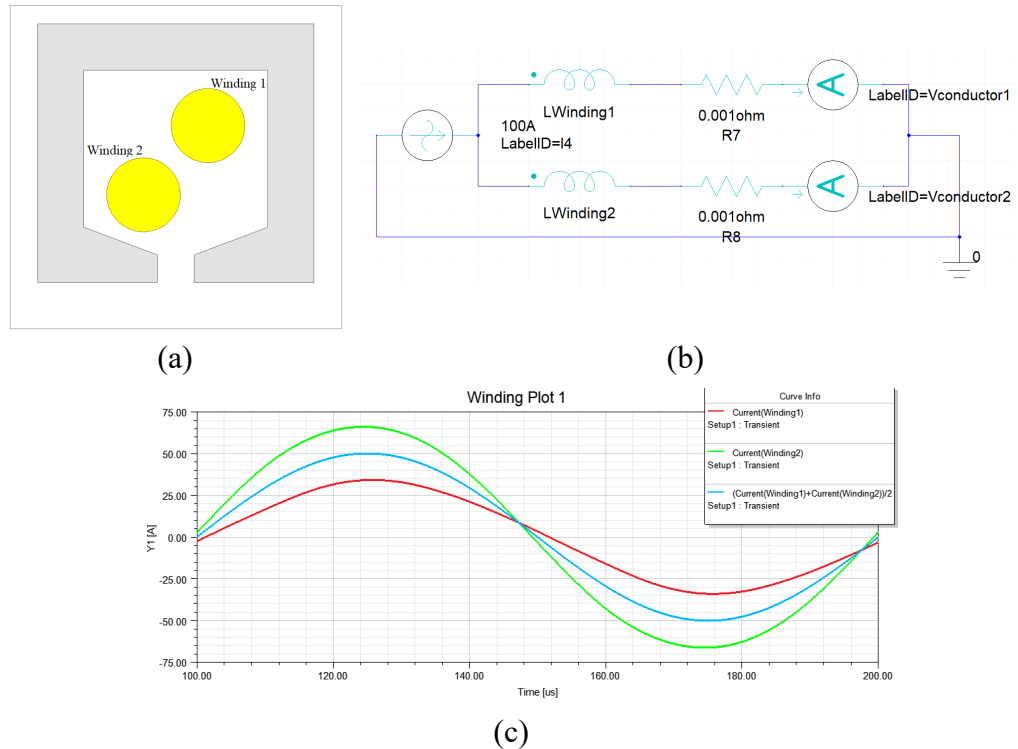
Figure 2.7 FEA simulation for circulating current illustration. (a) FEA configuration; (b) Connection of external circuit; (c) Current distribution in two conductors.

2.1.2 Core Losses

Core loss, also known as iron loss, is another critical component of the losses in electrical machines alongside the copper losses. Core loss refers to the energy dissipated due to the alternating magnetic field in the magnetic core of electrical devices, such as transformers and motors. Core loss constitutes a significant portion of the total losses, second only to copper losses, and has a considerable impact on efficiency, temperature control, material selection, design choices, and overall performance. Consequently, accurately predicting core loss and selecting the appropriate iron core material is essential.

The core losses consist of two main components: hysteresis loss and eddy current loss. Hysteresis loss in electrical machines refers to the energy dissipated as heat due to the lagging behavior of magnetic domains within a ferromagnetic material when it is subjected to a varying magnetic field. This loss occurs because the magnetic domains do not align instantaneously with the applied magnetic field, causing internal friction and energy dissipation during the cycles of magnetization and demagnetization [32]. An example of the BH loop is given in Figure 2.8, illustrating the magnetization process of the iron core.
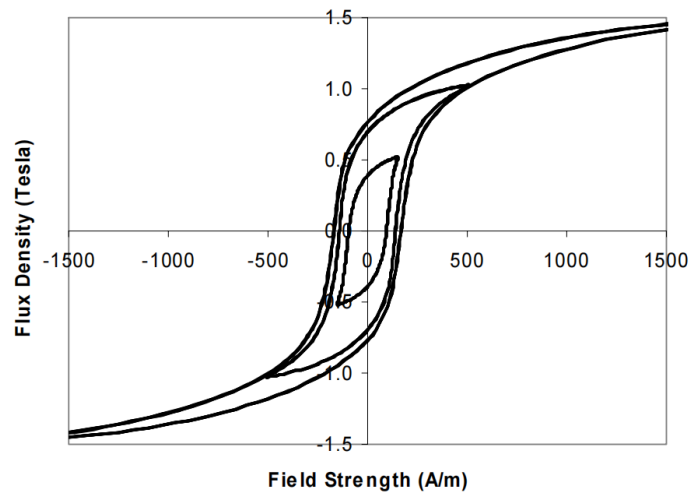
Figure 2.8 Example of BH loops for different values of peak flux density [33].

The energy dissipated in this process, i.e. the hysteresis loss, can be expressed as a close loop integral over one complete hysteresis loop:

$$P_\text{h}=f\oint HdB \tag{2.8}$$

where

Symbol	Unit	Explanation
P_h	W/m^3	The hysteresis loss per unit volume.
H	A/m	The magnetic field intensity.
B	T	The magnetic flux density

21

For different frequencies, the corresponding loop is selected for hysteresis loss calculation.

Although equation (2.8) provides a precise estimation on hysteresis loss, it is difficult to apply such equation in practice. Therefore, an approximation equation is proposed to provide a fast estimation on core loss when the magnetic flux density is sinusoidal [34]:

$$P_{h} = C_{h} B_{m}^{n} f \tag{2.9}$$

where

Symbol	Unit	Explanation
B_{m}	T	The peak value of sinusoidal magnetic field intensity.
C_{h}	W/(Hz*m^3*T^n)	Steinmetz coefficient (material-specific constant)
n		Steinmetz exponent (typically between 1.6 and 2.5)

Another important component of core loss is the eddy current loss, which is defined as the loss that occurs in the conductive materials of electrical machine cores due to the induction of eddy currents by a changing magnetic field [35]. The expression for eddy current loss P_e in a laminated core when the magnetic flux density is sinusoidal is given by [36]:

$$P_{e} = \frac{\pi^2 B_{m}^2 h^2 f^2}{6\rho} \tag{2.10}$$

where

Symbol	Unit	Explanation
P_{e}	W/m^3	The eddy current loss per unit volume.
h	m	Thickness of the core lamination.

As it is illustrated in (2.10), the eddy current loss in core is related to the

lamination thickness, material resistivity, magnetic flux density and frequency. Therefore, when choosing the core material for eddy current loss reduction, the working condition and the material properties should be considered comprehensively.

Except for hysteresis loss and eddy current loss, the concept of excess loss P_{exc} is also introduced because of the huge differences between the calculated results by classical eddy current loss equation and the measured results [37]. The excess loss P_{exc} caused by domain wall motion is generally obtained by curve fitting of the test results.

The total core loss can be expressed as the sum of hysteresis loss, eddy current loss and excess loss:

$$P_{Fe}=P_h+P_e+P_{exc} \tag{2.11}$$

2.1.3 Mechanical Losses

Mechanical losses in electrical machines are typically defined as the power losses that occur due to mechanical friction and aerodynamic drag within the machine. These losses are associated with the physical interactions and movement of the components of the machines and can significantly impact the efficiency and performance [38].

One component of the mechanical losses in electrical machines is bearing friction loss. This loss is defined as friction loss in the bearings that support the rotor. Although these friction effects are well-know, it is extremely difficult to quantify the value of these losses. Currently, empirical equations are widely employed for estimation of bearing friction loss based on the guidelines given

by bearing manufacturers [39]. For example, the bearing friction loss in the bearing manufactured by Swedish Ball Bearing Factory (SKF) can be calculated from [30]:

$$P_{\text{fri}} = 0.5\omega_{\text{mec}}\mu_{\text{fri}}F_{\text{load}}d_{\text{bearing}} \qquad (2.12)$$

where

Symbol	Unit	Explanation
P_{fri}	W	The total bearing friction loss.
ω_{mec}	rad/s	Angular frequency of the shaft supported by the bearing.
μ_{fri}		Friction coefficient (typically 0.08–0.20).
F_{load}	N*m	Bearing Load.

The other component of mechanical loss in electrical machines is the windage loss, which is defined as the loss generated by friction resulting from relative fluid/air movement in reference to the rotating parts of the machines [40]. Accurately quantifying windage losses is challenging, and current estimates are often based on experience and empirical equations, which are limited to specific scenarios [41]. The most precise method for predicting windage loss is through Computational Fluid Dynamics (CFD) techniques, though this comes at the expense of long computational times [42].

2.1.4 Additional Losses

In electrical machines, additional loss refers to the energy losses that occur beyond the primary predictable losses such as copper losses, core losses, and mechanical losses [43]. The additional loss can be caused by non-uniform current distribution, leakage flux and other irregularities under load conditions.

These losses are often attributed to various factors and are generally more difficult to quantify precisely.

Typical additional loss values in different machine types are given in Table 2.1. It can be observed that the additional loss is negligible in most of the machine types except for squirrel cage motors. Besides, the additional loss P_{add} can be roughly estimated with [30]:

$$P_{add} \sim (I_s^2 - I_0^2)\, f^{1.5} \tag{2.13}$$

where

Symbol	Unit	Explanation
I_s	A	The stator current.
I_0	A	No load current.

If extra losses are measured or known for a specific combination of current and frequency, then the additional loss of the machine at other working conditions, i.e. different combination of current and frequency, can be estimated using (2.13).

Table 2.1 Additional losses as a percentage of input power in electrical machines [30].

Machine type	Additional losses of input power
Squirrel cage motor	0.3%-2% (sometimes up to 5%)
Slip-ring asynchronous machine	0.5 %
Salient-pole synchronous machine	0.1–0.2 %
Non-salient-pole synchronous machine	0.05–0.15 %
DC machine without compensating winding	1 %
DC machine with compensating winding	0.5 %

2.2 AC Copper Loss Calculation Methods

2.2.1 Skin Effect

Given that the skin effect is caused by the alternating current inside the conductor, its modelling is not very complicated. For the round conductors, the skin effect loss at various frequencies with different diameters can be directly calculated using equation (2.5). As for the rectangular wire, its analytical equations have been deduced in [44], involving the influence of temperature and material. Moreover, a calculation method of skin effect in conductors of complicated shape is presented in [45]. The detailed current density distribution can be obtained by dividing the solid conductor into small segments and solving the electric circuit.

In summary, existing analytical approaches for skin effect have been extensively studied, demonstrating rapid and accurate computation capabilities.

2.2.2 Proximity

Currently, the most widely used method for calculating proximity loss is Finite Element Analysis (FEA), which has facilitated substantial advancements in mitigating these losses. The primary advantage of FEA is its exceptional accuracy, particularly with three-dimensional (3-D) FEA. In [46], 3D-FEA has been employed to evaluate the proximity loss and its impact on temperature rise in end-windings of a power inductor. Also, the obtained results were compared with the 2D-FEA model. The results were compared with those obtained from a two-dimensional (2D) FEA model, revealing that the 2D-FEA overestimated the

R_{ac} / R_{dc} ratio. In contrast, the 3D-FEA predictions were in good agreement with experimental data.

In addition, a multiphysics FEA model, incorporating both electromagnetic and thermal aspects, has been used to study the dynamic interaction between proximity losses and temperature rise [47]. This model successfully predicted the temperature rise in the windings of electrical machines. Similarly, the cooling technique for a high-speed machine was designed based on AC copper loss and temperature distribution in the windings as predicted by a coupled electromagnetic-thermal model in 3D-FEA. The measured temperatures at different parts of the machine confirmed the model's precision [48].

Furthermore, both 2D and 3D FEA have been employed to design winding shapes aiming at reducing proximity loss, leading to the production of shaped coils using additive manufacturing technology. Despite the complexity of the winding structure, significant reductions in losses were achieved [49].

Despite its high precision, a significant drawback of FEA is the long computational time. Efforts have been made to simplify models and reduce computational time for FEA simulations. For example, a 2D-FEA model compensating for end-winding effects was proposed to provide a fast estimation of AC copper loss in an axial flux machine. This approach saves significant computational time compared to 3D-FEA, with only a minor sacrifice in accuracy [50]. Another study on reducing the calculation time for AC copper loss in FEA involved modeling an equivalent current source in a harmonic solution

to simulate the effect of a rotating surface-mounted permanent magnet rotor [51]. Comparison between this equivalent model and the complete model showed that the substitution effectively reduced simulation time.

Despite progress in reducing the simulation time of AC copper loss models in FEA, this method remains inefficient, particularly for optimization purposes. As a result, faster calculation methods, including analytical approaches, have been considered for predicting skin effect and proximity losses.

One of the fast calculation approaches is semi-FEA method. In this method, the analytical equation is combined with FEA to provide a fast estimation on AC copper loss. In [52], the magnetic flux leakage in the slot is calculated using FEA and calculated by dividing the conductor area into several layers, and subsequently calculating the proximity loss using Equation (2.6). Similarly, the conductor area is divided into small rectangular areas in a fractional-slot permanent magnet synchronous machine to calculate the proximity loss [53]. With the increasing number of rectangles, the external magnetic flux density in the entire slot is obtained. The skin effect and proximity losses are also calculated using semi-analytical method, and the losses induced by high order harmonics are calculated and validated [54]. This method is further developed so that the stator saturation is considered and the harmonics caused by PWM is calculated precisely [55]. It turned out that the computational time is reduced significantly with high accuracy compared with detailed FEA.

Except for semi-FEA method, analytical approaches are also widely researched for proximity loss calculation. An analytical method, using 1-D

winding model in Cartesian coordinates and known as Dowell Equation, has been developed for evaluating the effects of eddy currents on transformer windings [56]. Dowell Equation was employed to calculate the AC winding losses of a close-formed rectangular transformer with round conductors [57]. Additionally, the Dowell equation can also be applied in transformers in the cylindrical coordinate with appropriate correction [58]. However, it should be noted that these equations are applicable for the close-formed rectangular transformers but may not be suitable for electrical machines [59]. In [60], the Squared Field Derivation (SFD) method was used to calculate the proximity losses considering complex 2D and 3D field effects along with arbitrary waveforms. This approach can simplify the magnetostatic filed calculation, resulting in saving computational resources. In addition, proximity losses were computed for various coil conductor shapes, including rod core [61], magnetoplated conductor [62], rectangular conductor [63], and round conductor [64]. In these studies, the geometric structure of the cores was not complex, allowing for the direct expression of magnetic field in a Cartesian coordinate. However, in the case of most rotating electrical machines, the presence of slot openings introduces substantial differences in flux leakage in the slot region compared to transformers.

Generally, 1-D analytical method [65] and 2D analytical method [66] are widely used to calculate flux leakage in the stator slot area. A 1-D analytical model can provide an appropriate approximation of the flux leakage distribution within the slot. However, its accuracy is reduced considerably near the slot

opening area due to its underlying assumptions. In contrast, 2D analytical model can precisely calculate the flux leakage in the vicinity of slot opening area.

Although the analytical methods offer can provide a swift estimation of proximity losses, their applications are constrained to the simple core structures, like rods or close-formed transformers. Even the most sophisticated analytical methods employing Laplace Equation cannot accurately predict the proximity losses of electrical machines with parallel teeth, mainly due to the challenge in presenting the slot shape within the coordinate system [67].

2.2.3 Circulating Current

Similar to skin effect and proximity losses, the most accurate method to calculate circulating current loss is FEA. The main drawback of circulating current calculation by FEA is also long computation time and large amount of computational resource. The situation is even worse than calculating the skin effect and proximity losses, because the electromagnetic field is coupled to the electrical circuit, and it will cause iteration in both current distribution between the strands and in current density distribution within the conductor.

Efforts have been made to reduce the computational time for calculation of circulating current loss using FEA. In [68], different FE models for AC copper losses were simulated to discuss the influence of modeling depth and compare the computational time and precision of resultant losses. It was found that a single slot model is sufficient in cases of distributed windings. In [69], the mesh settings on the slot area of an AC copper loss simulation model in FEA were examined, and two coarse mesh application methods were proposed. These

methods significantly reduced computational time while maintaining high consistency with the initial mesh division FEA model in terms of resultant circulating current.

Despite these efforts, calculating circulating current loss using FEA remains time-consuming and, consequently, difficult to apply for optimization purposes. To further reduce computational time, semi-analytical methods have been proposed. In [70] a semi-analytical method was developed to calculate the circulating current loss in a high-speed permanent magnet machine. The proposed method's simulation time was only 1/400 of that required for FEA, with an error margin within 2%. The accuracy of this method was also validated experimentally. In [71], a flexible semi-analytical method for calculating circulating current was proposed, solving the electrical equation with parameters derived from FEA. This method can calculate the Joule loss of litz wire twisted at different angles. Similarly, in [72], detailed electrical equations for each strand were established, and the parameters were obtained using FEA, considering the effects of end-winding and temperature. This method was also used to calculate circulating current in stranded windings [73] and form-wound windings [74] in electrical machine, in electrical machines, with results showing good agreement with FEA.

While semi-analytical methods provide rapid calculations for circulating current losses, understanding the coupling relationship between FEA and analytical equations remains challenging, in addition to the programming for the interaction between different software.

Except for semi-FEA methods, analytical methods are also proposed to provide an estimation of circulating current loss even faster than the semi-analytical methods. One of the analytical calculation methods is the subdomain approach [75]. This method offers a computationally efficient and accurate prediction in contrast with FEA once the sophisticated computational equation is completed. However, it is limited to calculating the flux leakage inductance for the strand in slots of sector-shape and rectangular-shape. Further development of this method is presented in [76] to estimate the current density distribution and the proximity loss in each conductor.

Furthermore, magnetic circuit method is also utilized in estimation of flux leakage inductance. This approach has been employed to predict the circulating current of various winding transposition in large turbogenerators [77]. The method is also utilized in [78] to calculate the circulating current loss in a high-speed permanent magnet synchronous machine, where the slot with parallel teeth is transferred into rectangular slot and parallel magnetic flux leakage in the slot is assumed. However, when this method is applied on smaller electrical machine [79], the result turned out to be unsatisfactory. This is because it assumed that all the wires are on the center line of the slot, and the magnetic flux line in the slot is parallel. It is difficult to calculate the complicated magnetic flux in the slot precisely.

2.3 Winding Technologies

Extensive research has been conducted to develop various techniques for reducing copper losses in electrical machines based on different calculation

methods. This chapter provides a detailed review of these wire techniques, in addition to those with potential to serve as the foundation for optimized winding designs.

2.3.1 Litz Wire

One of the most effective techniques for mitigating AC copper loss is the use of litz wire, which has been widely adopted in applications such as inductors and transformers, operating at frequencies up to hundreds of kilohertz [80]. As previously mentioned, using conductors with a very small radius can significantly reduce skin effect loss. Typically, the radius of the conductors in litz wire is very small (less than 0.4 mm), which effectively reduces skin effect and proximity losses in most electrical machines operating at fundamental frequencies lower than 2000 Hz. Furthermore, the strands within the litz wire are twisted to alter their positions within the slot, thereby equalizing the inductance values in each strand and suppressing circulating current losses.

Consequently, all components of AC copper loss, including skin effect, proximity effect, and circulating current losses, are significantly minimized. The reduction is significantly substantial that in most of the calculations, the AC copper loss is often assumed to be completely eliminated [81]. The structure of litz wire is shown in Figure 2.9.
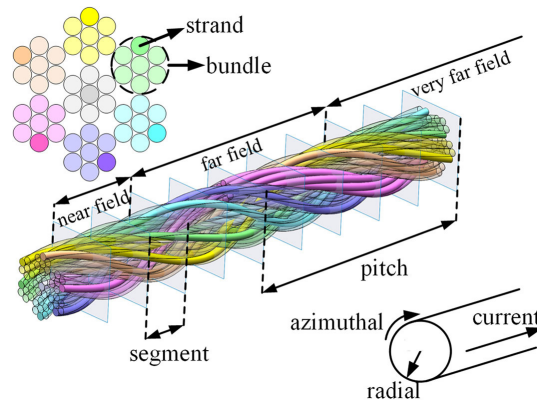
Figure 2.9 Structure of litz wire [82]

To design litz wire for different application scenarios, various factors must be considered, including the strand number [83] and twist angle [84]. For the strand number, the optimal design balances the tradeoff between skin effect loss, proximity loss, and DC copper loss to achieve minimal Joule loss in the conductor. Regarding the twist angle, it has been demonstrated that full transposition, meaning a 360° twist angle, results in the minimum AC copper loss.

While the use of litz wire can significantly reduce AC copper loss, it comes with drawbacks such as high manufacturing costs, low slot fill factor, and potential thermal performance issues. The tradeoff between the cost and losses is evaluated in [85], which illustrates that the cost of litz wire increases rapidly as the strand diameter decreases. Additionally, it has been reported that using ideal litz wire results in a slot fill factor of around 30% in electrical machines [86]. The impact of litz wire on the thermal performance of electrical machines is discussed in [87], indicating that the impregnation process can introduce significant errors in temperature spot predictions. These inherent drawbacks of litz wire restrict its application in electrical machines.

In addition to conventional litz wire, a novel manufacturing technology has enabled the production of formed litz wire, as shown in Figure 2.10. Similar to conventional litz wire, this novel type also consists of small-diameter strands connected in parallel. However, the precise position of each strand is fixed using advanced manufacturing techniques, resulting in a substantial improvement in the slot fill factor. The thermal performance of formed litz wire is shown to be superior to that of conventional litz wire [88]. Additionally, its electromagnetic performance benefits for electrical machines have been illustrated through comparisons with random-wound round wire and hairpin winding [89].

Despite all the benefits of formed litz wire, it is worth noticing that the difficulties in manufacturing process and machine are still challenging [90].

(a)   (b)
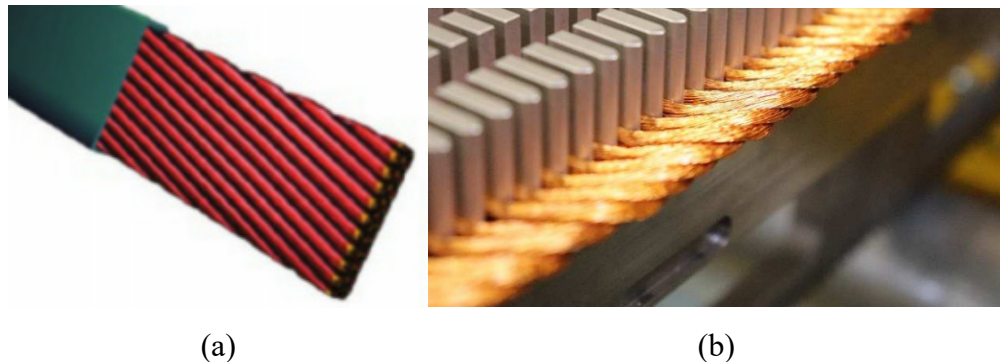
Figure 2.10 (a) Structure of formed litz wire. (b) Real formed litz wire product [91].

2.3.2 Aluminum Wire

Although copper wire is the most commonly used in electrical machines, aluminum wire is also employed in high power density machines. The primary benefit of using aluminum wire is the reduction in AC copper losses. According to equation (2.2) and (2.6), the DC Joule loss of aluminum wire increases due to its lower conductivity, while AC copper loss decreases. To compensate for the

35

high DC Joule loss, electrical machines using aluminum wire generally have a higher slot fill factor. Various studies report that the slot fill factor in electrical machines with aluminum wire can reach up to 83.8% [92].

Beyond the advantage of lower AC copper losses, aluminum winding also has the potential to enhance power density in specific application scenarios, as the mass density of aluminum is only 30% that of copper. In a high power density machine designed for aerospace applications, pre-compressed aluminum wire was used, maintaining the required loss levels while reducing the machine's overall weight by 10% [93], demonstrating the potential for substantial weight reduction in electrical machines by using aluminum wire.

Another notable advantage of aluminum wire is its low cost. Aluminum wire costs approximately 10% per unit volume and 30% per unit mass compared to copper [94].   In the context of electric vehicles, using aluminum wire in traction motors has been shown to reduce the weight of the windings by 66% and the cost of the wire by 90%, making it a viable option given the battery and cost limitations [95].

The decision to use aluminum wire depends heavily on the application scenario and operating conditions of the machine. A comprehensive tradeoff between DC Joule loss, AC copper losses, weight, and cost must be considered. Such tradeoffs are detailed and compared in [96].

Despite these advantages, a significant drawback of aluminum wire is the increased DC Joule loss, which imposes a heavy burden on the thermal management of electrical machines. Consequently, aluminum wire can only be

used in specific scenarios where its benefits outweigh the challenges associated with thermal management.

2.3.3 Additive Manufacturing Wire

To build windings with low AC copper loss, advancements in wire construction technology are crucial. The optimization of windings for AC copper loss mitigation is often constrained by manufacturing processes. Even when an optimized winding design proves effective in reducing AC copper loss, it may not be feasible to implement due to manufacturing limitations. Additive manufacturing (AM) offers a viable solution to this problem. AM, known for its ability to create virtually unconstrained, three-dimensional, no-waste, rapid prototypes of parts and components, has become a popular research topic in recent years [97]. Once the winding design is complete, AM can produce the winding regardless of its complexity. In addition to high flexibility, AM offers benefits such as short end-windings, higher operational temperatures, and controllable conductor conductivity [98].

When adopting AM wire in electrical machines, the first consideration should be the wire's conductivity. As indicated in [99], the conductivity of AM-formed wire varies significantly depending on the laser technology and metal powder used. Figure 2.11 shows that most AM wires have much lower conductivity than pure copper, with only the most advanced wires approaching pure copper conductivity. The progress in conductivity of AM wires is facilitating its use in practical electrical machines.

Using AM's high flexibility, hollow conductor coils have been proposed for

37

high-power-density machines rated at 250 kW [100]. The hollow center of the conductor serves as a cooling channel for direct heat exchange, resulting in a high electrical loading of 94,266 Arms/m, an average current density of over 20.09 Arms/mm^2 and a high-power-density of over 20 kW/kg. A comparison of mechanical performance, electrical properties, and thermal performance between aluminum alloy and copper alloy illustrates that, despite the conductor's low conductivity, such windings are feasible for high power density machines in aerospace applications due to power density enhancements [101].
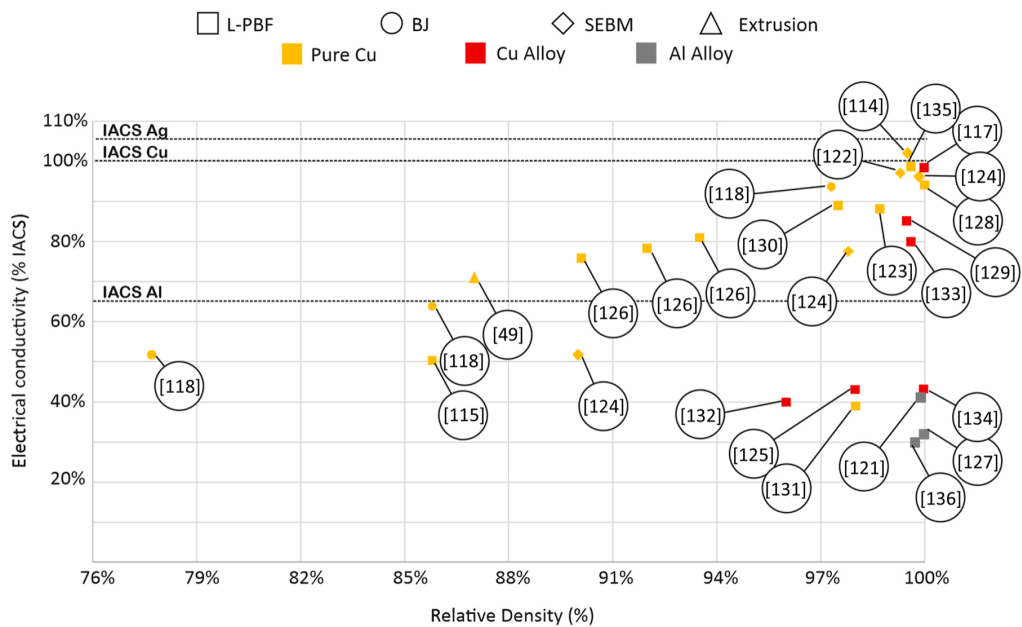
Figure 2.11 Comparison of printed conductive materials in terms of relative DC conductivity (%IACS) and relative density [99].
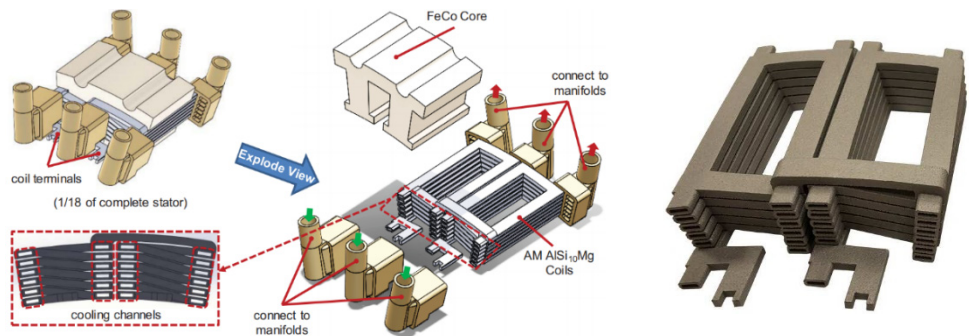
Figure 2.12 Modular stator and additively manufactured hollow conductor integrated with direct cooling [100].

38

Similarly, another additively manufactured coil with a cooling channel is reported in [102]. In this study, powerful cooling techniques are adopted to enhance the current density of the coil. The shape of the conductor is designed to balance the cooling channel and AC copper loss reduction, resulting in 11.7% of AC copper loss among overall losses at 500 Hz. Despite the low conductivity of aluminum alloy, the designed DC current density of the conductor reached 100 A/mm^2.

<div align="center">(a)   (b)</div>
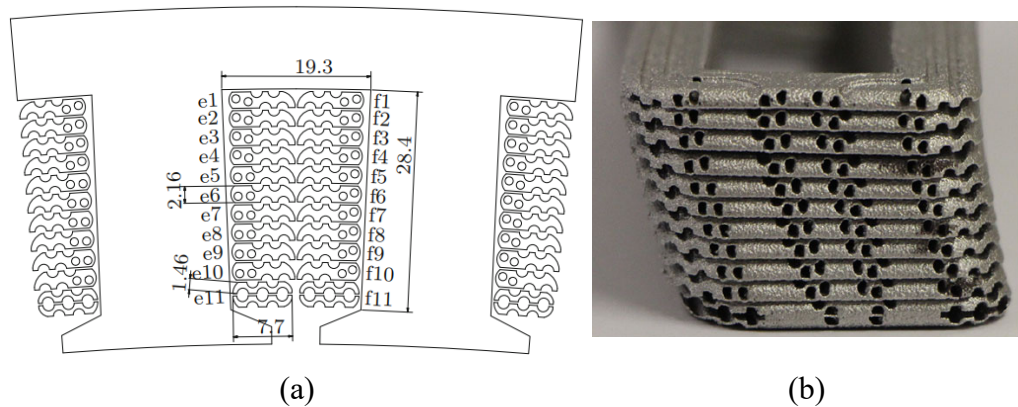
Figure 2.13 (a) Schematic of the 3D-printed coil (b) 3D-printed coil prototype.

Another case of an additively manufactured coil is illustrated in [103], demonstrating AM's capability to form complex coil shapes. In this research, the coil is designed parallel to the magnetic flux leakage direction in the slot to reduce proximity loss and skin effect loss. Although the shaped conductor's conductivity is only 75% of pure copper, its overall copper loss from 600 Hz to 1000 Hz is much lower than that of regular flat copper wire. This reduction in AC copper loss enhances the overall performance of the electrical machine and highlights the potential of AM wires [104].
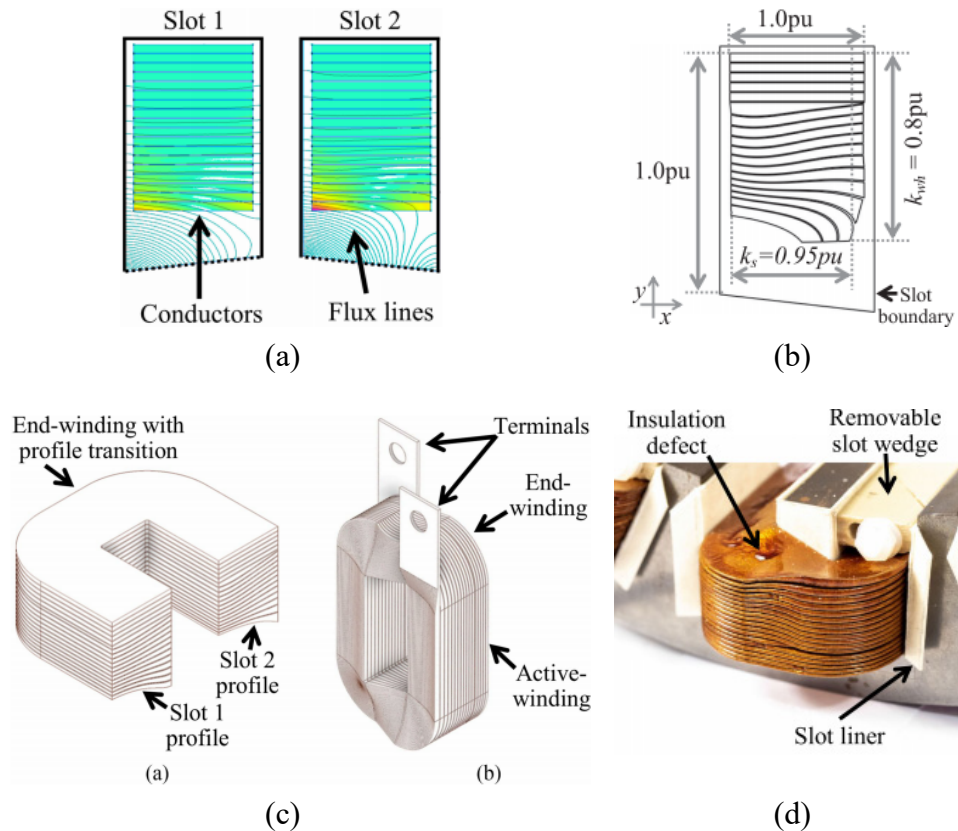
Figure 2.14 (a) Magnetic flux leakage in the slot. (b) Designed conductor shape parallel to magnetic flux. (c) CAD illustration of the shaped profile winding. (d) Additively manufactured shaped profile winding in stator [103].

Despite the benefits of design freedom and potential performance improvements, AM is still restricted by the challenge of precisely controlling material properties during manufacturing, which influences the thermal and electrical conductivity of the winding [105].

2.3.4 Winding Transposition

As illustrated in equation (2.5) and (2.6), the skin effect and proximity loss of a round conductor are primarily determined by the size of the conductor. This principle also applies to conductors of other shapes. Therefore, a common technique to reduce skin effect and proximity loss is using conductors with a very small diameter. However, simply increasing the number of strands does not

reduce copper loss, as the circulating current loss increases with the number of strands [106]. Figure 2.7 demonstrates that the circulating current is heavily influenced by the conductor's position in the slot. Consequently, extensive research has been conducted to explore circulating current loss in various conductor placements, such as winding transposition, to propose solutions that suppress circulating current loss while utilizing a large number of strands.

The first type of winding transposition can be categorized as transposition with round conductors. Although achieving transposition with round conductors in experiments and manufacturing is challenging, it is still valuable to conduct such research to explore the relationship between conductor placement and circulating current loss. A preliminary investigation into winding transposition is presented in [107], which experimentally compares the copper loss of several different winding transpositions in an electrical machine. It is shown that bad winding transposition can significantly increase overall losses, whereas good transposition can minimize circulating current loss. In [108], the influence of conductor placement and strand number on overall copper loss in a motorette is discussed, providing guidance on conductor placement during the design of electrical machines. Notably, a 3D-printed plastic mold was used in the experiment to precisely fix the conductor positions. Similarly, in [109], the discussion focuses on the effect of winding transposition on the copper loss of the entire electrical machine, concluding that AC copper loss suppression techniques can be applied to machines with different pole-pair numbers. Another practical winding suppression method, proposed in [110], considers the

difficulties of realistic winding installation and suggests using a clamp to fix each conductor's precise position. In addition to winding transposition, the influence of temperature on circulating current loss is comprehensively discussed [111].

(a)   (b)
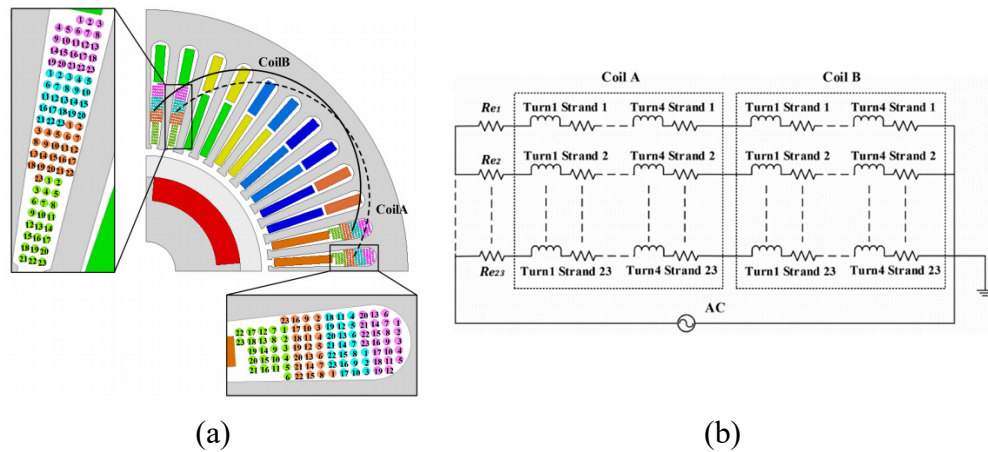
Figure 2.15 (a) Winding transposition scheme. (b) Electric circuit connection [110].

For rectangular conductors, winding transposition is also explored. Generally, there are three types of rectangular conductors: form-wound winding, Roebel bar coil, and hairpin winding. A comprehensive discussion of magnetic flux leakage, slot shape, and temperature for form-wound winding is presented in [112]. It is concluded that a semi-closed slot opening induces much higher AC copper loss than an open slot, and AC copper loss increases rapidly with temperature. A The winding transposition of form-wound winding, particularly concerning strand number and conductor size, is discussed in [19], illustrating that increasing the number of strands does not simply decrease copper loss.
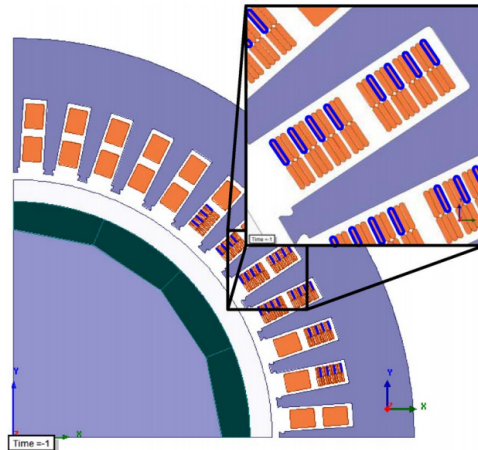
Figure 2.16 FE model of the electrical machine with form-wound winding [112].

Another type of rectangular wire used in electrical machines is the Roebel bar, which is widely employed in large turbo generators. In these machines, transposition of parallel strands reduces circulating current loss, effectively suppressing circulating current with proper transposition [113]. Detailed transposition schemes, including strand number and end-winding parts, are illustrated in [114]. Different winding transpositions of Roebel bar windings are discussed and compared, showing that more complex transposition schemes can further suppress circulating current. Additionally, the mechanism of circulating current caused by the end-winding part in a large turbo-generator with a stator coil is presented in [115], demonstrating that slight changes in transposition angle can effectively reduce circulating current caused by the end-winding effect.
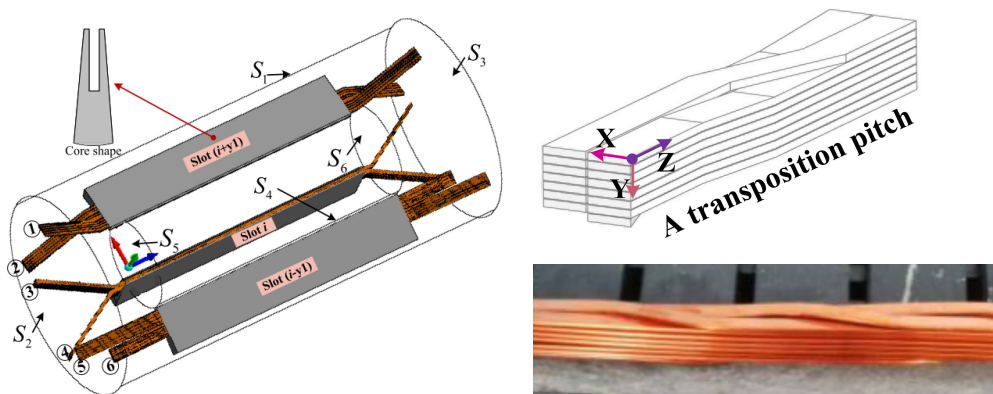
Figure 2.17 Structure of rectangular Roebel bar [112].

The third type of rectangular wire is hairpin winding, known for its high slot fill factor and quick manufacturing process. Due to the limited number of strands in hairpin winding, it is possible to eliminate circulating current loss using symmetrical transposition [116]. The transposition of hairpin winding is adopted in a 24-slot, 4-pole, and 4-layer configuration, completely eliminating circulating current in the case [117]. However, the skin effect and proximity losses can be substantial due to the large conductor cross-sectional area. Therefore, research on partial transposition of conductors near the slot is conducted [118]. This study uses segmented conductors transposed near the slot opening area, significantly reducing copper loss and suppressing AC copper loss to very low levels. In addition to the segmented area near the slot opening, conductors of different thicknesses are explored [119]. Comparing regular hairpin winding with hairpin winding of varying thicknesses shows that using thinner conductors near the slot opening effectively reduces AC copper loss.
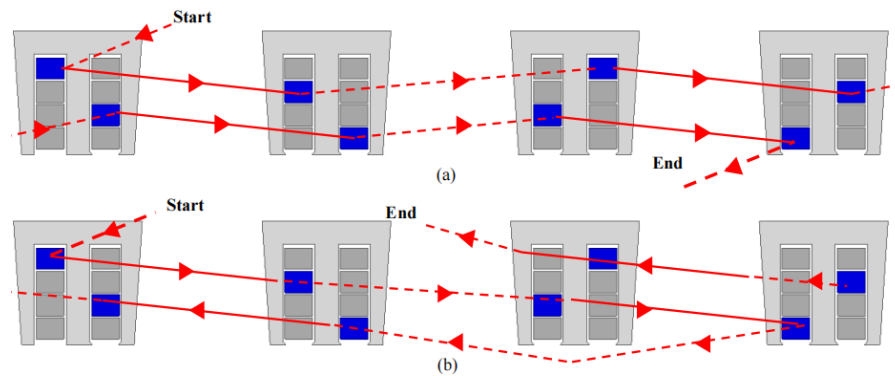
Figure 2.18 Winding transposition scheme of hairpin winding [116].

2.4 Summary

This chapter provides a comprehensive review of advanced techniques for addressing AC copper loss, including calculation methods, winding

manufacturing technologies, and academic research.

Research on complex magnetic flux leakage is currently limited. Since magnetic flux leakage directly influences proximity loss and circulating current loss, this lack of understanding hinders the development of windings designed to minimize AC copper loss. Although FEA provides precise estimations and is widely used in AC copper loss research, its computational time is too long for effective optimization purposes.

Moreover, the research on winding transposition is fragmented. Different winding transposition methods are not well-featured or categorized, making it challenging to determine which winding structures effectively reduce AC copper losses. Systematic research on winding structures is necessary to address this gap.

Chapter 3 Proximity Loss Calculation Using MEC

As previously reviewed, the research on calculation methods for magnetic flux leakage remains limited, restricting the further development of low AC copper loss winding designs. To provide a new perspective on magnetic flux leakage calculation, this chapter proposes a novel method based on mesh-based magnetic equivalent circuit (MEC). The proposed method is highly flexible, accommodating various slot shapes, and can offer a fast and precise estimation.

The modeling and calculation process of the proposed method is demonstrated by calculating the magnetic flux leakage and proximity loss in a baseline electrical machine. The results obtained using MEC closely match those from finite element analysis (FEA) and experimental data, validating its effectiveness and efficiency. This alignment confirms the proposed method's potential to advance low AC copper loss winding designs.

3.1 Problem Description

3.1.1 Baseline Machine Parameters

The geometry of an existing machine serves as the reference model, designated as the baseline machine as shown in Figure 3.1, and its corresponding parameters are detailed in Table 3.1. To study the proximity loss phenomena, round conductor is selected, and the diameter of the copper conductor is chosen large enough as shown in Figure 3.2. This conductor configuration satisfies the figures in Table 3.1. It is noteworthy that in order to focus on the proximity loss calculation and eliminate the effect of circulating current, it is assumed that

complete transposition techniques were employed to effectively minimize circulating currents within this machine.
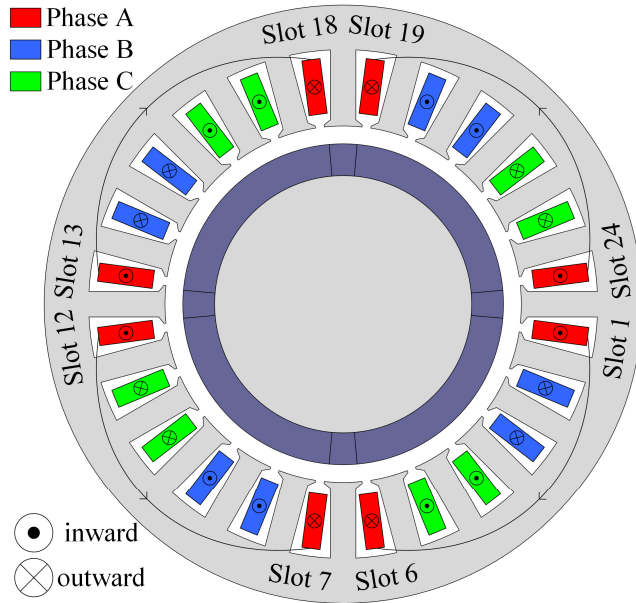
Figure 3.1 Schematic of the baseline machine model.

Table 3.1 Machine Parameters

Description	Specification	Description	Specification
Machine type	3-phase PMSM	Stator outer diameter	235 mm
Magnet material	SmCo33E	Inner radius of stator R_s	70 mm
Core material	10JNEX900	Rotor radius R_m	63 mm
Wire conductivity σ	5.8×10^7 S/m	Tooth tip height	0.8 mm
Rated power	300 kW	Slot opening	3.5 mm
Rated speed	30000 rpm	Yoke thickness	17.5 mm
Fundamental frequency f	1000 Hz	Slot height	27.4 mm
Number of pole pair N_p	4	Tooth width	10 mm
Number of slots Q	24	Stack length l	130 mm
Number of turns n	2	PM thickness h_{PM}	12.5 mm
Airgap g	7 mm		
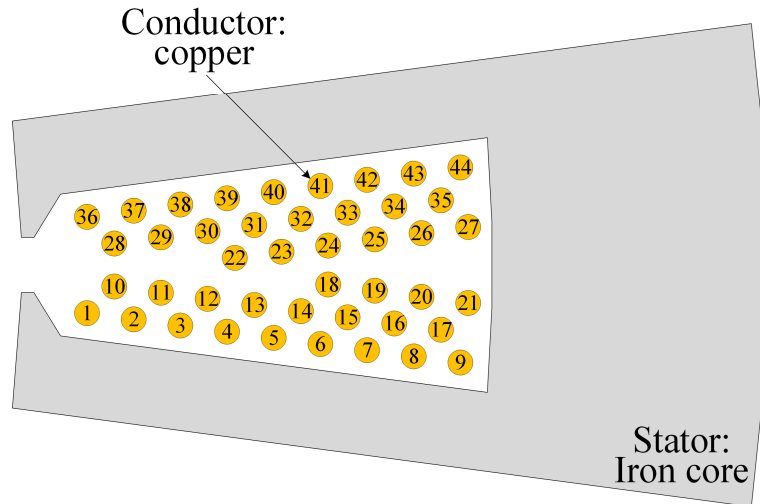
Figure 3.2 Conductor shape and position

3.1.2 Modelling Objective Description

When calculating the copper loss of an electrical machine, it is a good approximation to model one slot of the machine rather than all slots in order to simplify the model. To verify the validity of such simplification, the whole-machine model, stator-only model and one slot model are simulated in FEA, and the resultant copper loss is compared and shown in Figure 3.3.
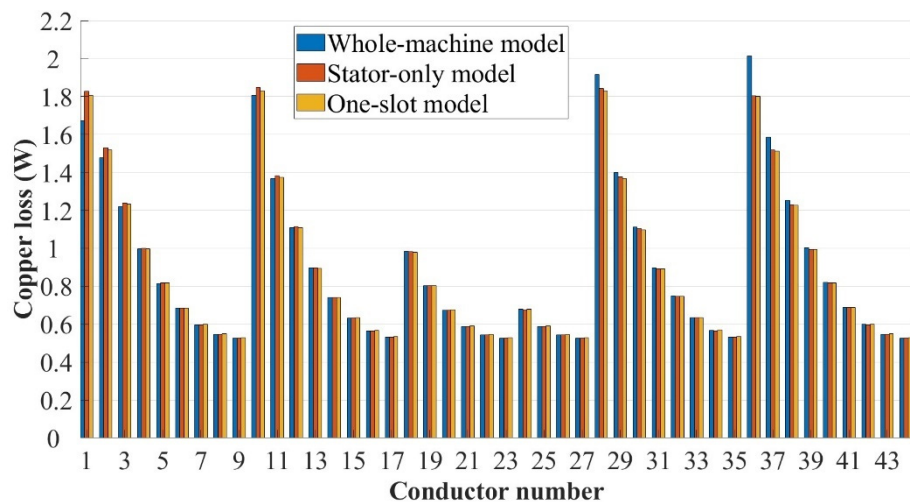
Figure 3.3 Copper loss of each conductor in whole-machine model, stator-only model and one-slot model

It turned out that the average copper loss error in each individual conductor in stator-only model is 2.8% while the error in one-slot model is 2.3%. It can

48

also be concluded that modelling permanent magnet or not has a minimal impact in copper loss. The reason for the minimal difference is that the magnetic flux generated by permanent magnet and conductors in other slots is negligible in the slot, resulting in minimal difference in external magnetic flux of the conductors with or without the permanent magnet. By comparing the stator-only model and one-slot model, it can be observed that the copper loss difference between the whole machine model and stator only model is mainly caused by saturation. Due to the minor copper loss difference in whole-machine model and one-slot model, in the following discussion, only one slot is modeled in MEC.

3.1.3 Assumptions and Simplifications

Some assumptions were made to build the MEC model in this study as follows:

   i.   The permeability of the stator is infinite.

   ii.   The temperature and the conductivity of the conductor are constant.

   iii. The eddy current inside conductors has no impact on the flux leakage.

Based on these assumptions, the limitations of the proposed method are established accordingly. Assumption i renders the proposed method inapplicable to saturated iron core, while assumption iii excludes its use in cases involving large-section conductors. Proximity effect will change the current distribution inside the conductor, subsequently impacting the flux leakage distribution. Such effect can be neglected for small-section conductors, but for large-section conductors the error will become considerable.

Considering these assumptions, further simplification can be made. Since

the permeability is assumed to be infinite, the flux leakage distribution in the slot could be regarded as the linear superposition of flux leakage generated by each individual conductor. Therefore, the calculation process of flux leakage generated by one single conductor is explained as follow section.

The initial step involves in discretising the slot domain and building the MEC. Subsequently, by solving the MEC with one single conductor, the magnetic field in the slot domain generated by one conductor is calculated. This process is repeated for all conductors and by applying the linear superposition law, the proximity loss and leakage flux can be computed.

3.2 Magnetic Equivalent Circuit (MEC) Modelling

3.2.1 Principle of MEC

Table 3.2 MEC physics parameters and its analog in electric circuit [120]

Magnetic Circuit	Electric Circuit
Permeability μ (H/m)	Conductivity σ (S/m)
Magnetomotive Force F (A*N)	Voltage U (V)
Magnetic flux Φ (Wb)	Current I (A)
Magnetic reluctance R_m (H^{-1})	Electrical Resistance R (Ω)
Magnetic permeance Λ (H)	Electrical Conductance G (S)
Magnetic voltage $F = HI = \Phi R_m$	Voltage $U = IR$
Magnetic Ohm Law $\Phi = F/R_m$	Ohm Law $I = U/R$

The magnetic equivalent circuit (MEC) is a simple, fast, and effective approach to accurately calculate the magnetic flux density in the electromagnetic systems. This method is universally utilized for preliminary assessment of the

electromagnetic characteristics of electrical machines. The principle of MEC could be interpreted as the analog to the principle to electric circuit, as it is illustrated in Table 3.2.

Similar to Kirchhoff Current Law and Kirchhoff Voltage Law, in the MEC, the sum of magnetic flux entering a node is always equal to the sum of magnetic flux leaving the node, while the directed sum of magnetic potential differences around any loop in a circuit is zero. The principle is described in equation as:

$$\sum \Phi = 0 \tag{3.1}$$

$$\sum F = \sum HI = \sum \Phi R_{\mathrm{m}} \tag{3.2}$$

Magnetic permeance of different shapes and different magnetic flux direction and their value can be calculated from Table 3.3.

Table 3.3 Magnetic permeance calculation

cube	Trapezoid (tangential direction)	Trapezoid (normal direction)
$G=\dfrac{\mu h l}{w}$	$G=\dfrac{\mu l h}{w_2\text{-}w_1}\ln\left(\dfrac{w_2}{w_1}\right)$	$G_{r1}=\dfrac{\mu l}{h}\dfrac{w_2\text{-}w_1}{\ln\left(\dfrac{w_2}{w_1}\right)}$
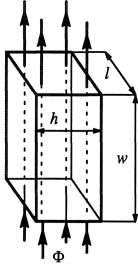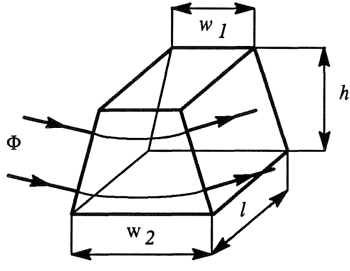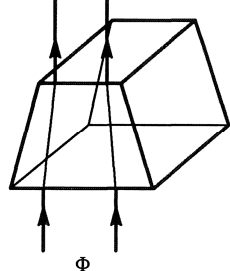
Mesh-based MEC is an advanced MEC model which discretize the study domain by multiple magnetic networks comprising reluctances / permeances in both radial and tangential directions. According to the mesh division, the value of magnetic reluctances is calculated, and the excitation is added accordingly. By solving the circuit, the magnetic flux density distribution is obtained. This

technique allows to estimate the magnetic flux density as accurate as FEA.

3.2.2 Mesh Process and Calculation of Magnetic Permeance

The geometry of the slot could be divided by small mesh elements. These mesh elements are achieved through radial discretisation of the stator slot from the inner diameter of stator to the bottom of stator slots. Consequently, each mesh element has a circular sector shape. Inside each mesh element, there are always two magnetic permeances in the tangential direction and two in the radial direction as shown in Figure 3.4. The boundaries of mesh elements are represented in dotted lines. It is worth noting that the intersection points of the slot which are highlighted in red (See Figure 3.5), always coincide with the corner of the element. This makes it possible to model different materials inside one mesh element. In addition, the density of the mesh in the slot area can be adjusted to obtain higher accuracy considering the size of conductors.

Radial and tangential magnetic permeances in each mesh element can be calculated by [121]:

$$G_{r1} = \frac{\mu l}{h} \frac{w_2 - w_1}{2 \ln \left(\frac{w_2 + w_1}{2w_1} \right)} \tag{3.3}$$

$$G_{r2} = \frac{\mu l}{h} \frac{w_2 - w_1}{2 \ln \left(\frac{2w_2}{w_2 + w_1} \right)} \tag{3.4}$$

$$G_{\theta} = \frac{\mu l h}{\frac{(w_2 - w_1)}{2}} \ln \left(\frac{w_2}{w_1} \right) \tag{3.5}$$

where μ represents the permeability of the material, l is the axial length of the machine, h denotes the height of the mesh element, w_1 and w_2 are the length of inner and outer section of the arc in the mesh element.
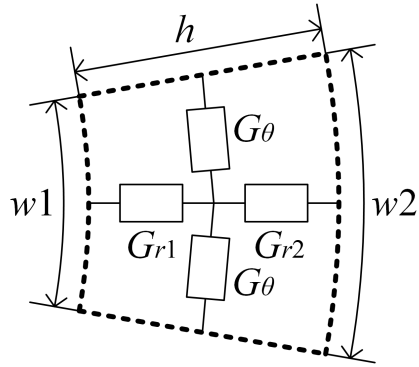
Figure 3.4 Magnetic permeance of a mesh element.

air permeability   ——▭——

iron core permeability   ——▭——
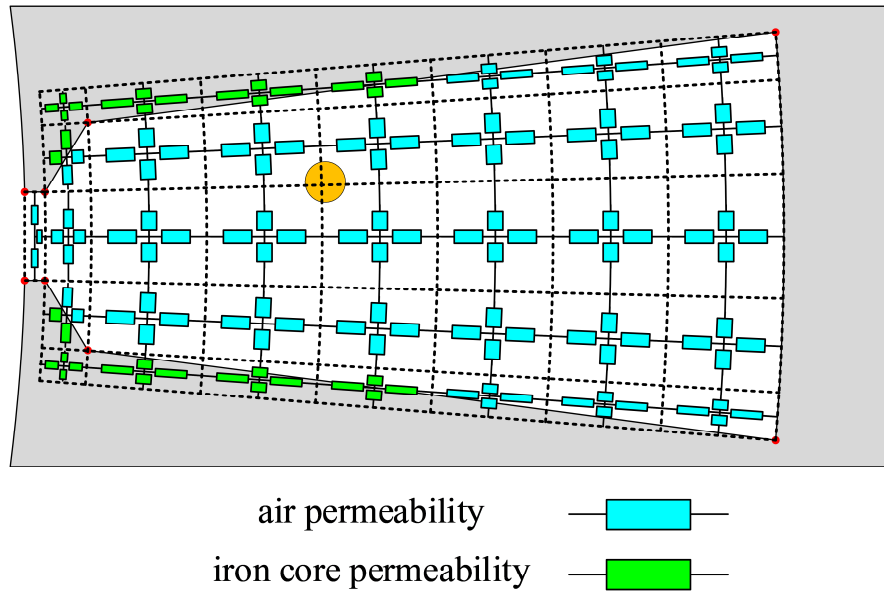
Figure 3.5 An example of mesh and formed magnetic circuit.

As can be seen in Figure 3.5, when the centre of the mesh element is within

the air area, the air permeability is assigned to the permeances. On the other hand,

if the centre of the mesh element is within the iron area, the iron permeability is

considered. In addition, when the element centre lies on the boundary between

two different materials, which represents roughly 50 % of the area covers iron

core and the remaining part covers air, a tuning is made. In this circumstance,

two of the magnetic permeances in the mesh element is substituted with iron core

permeability and the other ones with air permeability.

It is worth mentioning that this approach might introduce some calculation

errors at the slot edge. However, these errors can be mitigated by increasing the number of mesh elements on the edge area. By increasing the number of mesh elements, the slots with various shapes can be approximated, as it is illustrated in Figure 3.6.
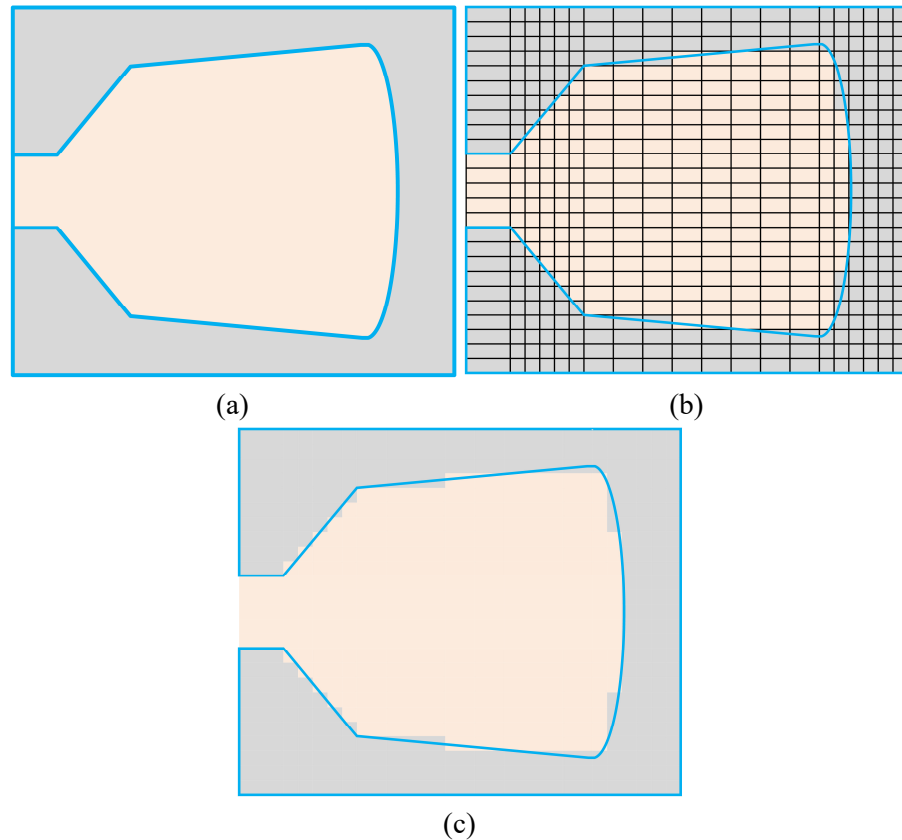
Figure 3.6 Approximation using mesh elements with regular shape. (a) Original slot. (b) Approximated slot with solid line mesh element boundary. (c) Approximated slot without mesh element boundary line.

3.2.3 Magnetic Source Modelling

To obtain a complete magnetic circuit, it is necessary to define the magnetomotive force (MMF) to the magnetic circuit according to the position of the conductors.

To demonstrate the principle of incorporating the MMF sources into the magnetic circuit, a C-shape iron core with a conductor placed inside is

considered as an example as shown in Figure 3.7(a). Regardless of the position of the conductors and the shape of the slot, the magnetic flux consistently forms a closed loop around the conductor. The magnetic circuit can be defined by assuming the conductor placed in the center as shown in Figure 3.7(b), and the value of the MMF source corresponds to the value of current flowing in the conductor. By further discretizing the domain into smaller sections, an equivalent circuit model with more permeance with the aim of enhancing the calculation can be obtained – see Figure 3.7(c). Moreover, this MMF source can also be split into multiple parallel-connected branches as shown in Figure 3.7(d) to model filed more precisely. The sum of G_1, G_2, G_3 and G_4 is equal to G_0, and the value of MMF sources in each parallel branch are identical with F.

Despite the iron core shape and the conductor position, there is always very few magnetic flux lines in radial direction between the conductor and yoke. This is because the magnetic flux line rotates around the conductor. So, the magnetic flux generated by this conductor is mainly in tangential direction. Since there are very few magnetic flux lines in radial direction branches, the branches in radial direction can be equivalent to can be removed. Then the magnetic circuit in Figure 3.7(d) could transferred into Figure 3.7(e). For the same reason, the magnetic permeance is added in the radial direction in the mesh element with MMF sources, the mesh of the whole area is completed as presented in Figure 3.7(f).
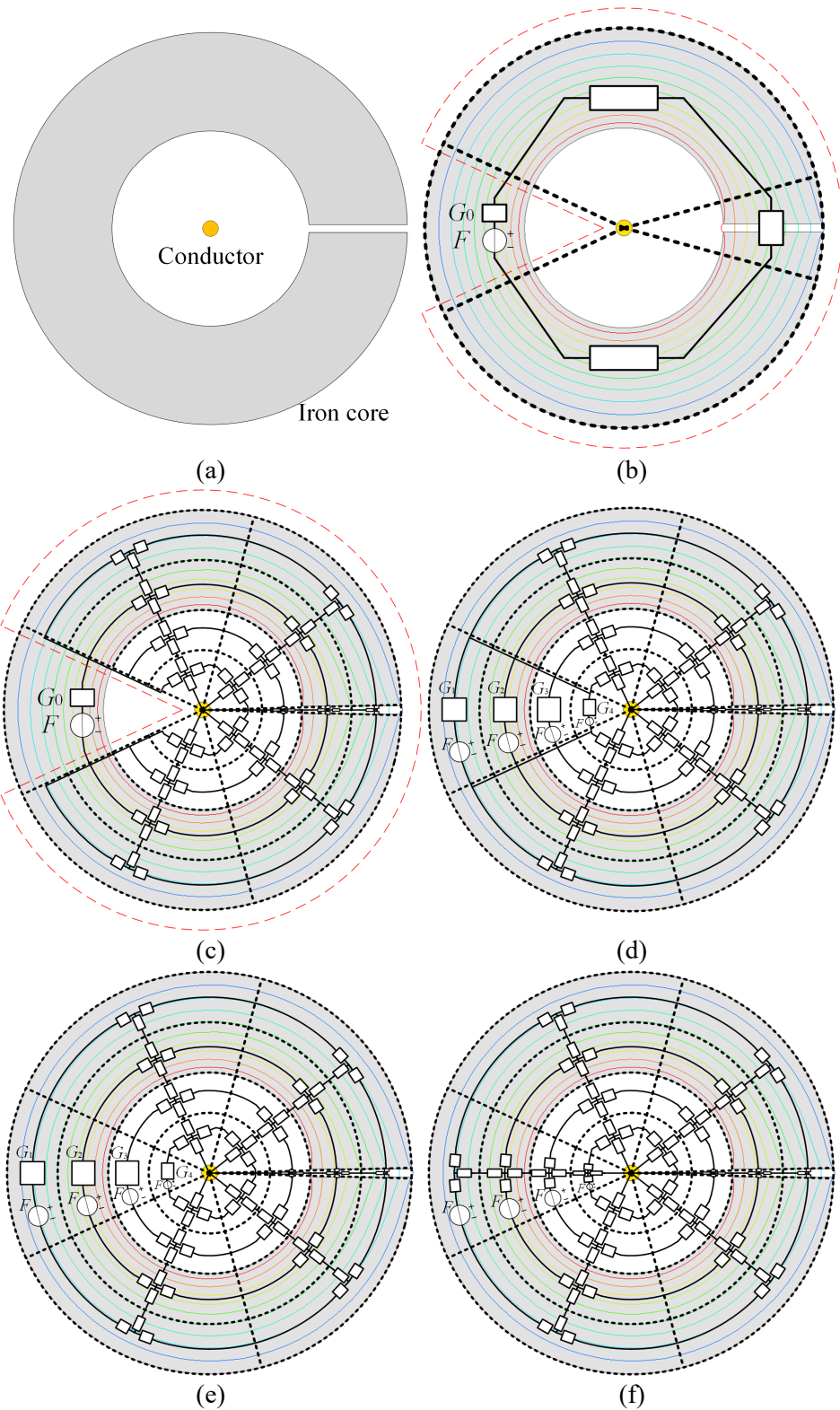
Figure 3.7 MMF source theory demonstration. (a) Structure of example iron core. (b) Rough Magnetic Circuit. (c) Meshing the part without MMF source. (d) Meshing the part with MMF source. (e) Removing spare connections in MEC. (f) Final mesh-based MEC.

In summary, the process of MMF source modelling can be described as:

1) Take the conductor center as the starting point, draw the shortest straight line to outer stator yoke.

2) Add MMF source in tangential direction branches which intersect with this straight line.

Applying this methodology, the magnetic circuit of the stator slot represented in Figure 3.5 can be completed as shown in Figure 3.8 by adding the MMF sources due to the single conductor inside the slot domain. When the conductor is at different positions, the magnetic permeance and the branches remain the same while the MMF sources are added differently according to the position of conductor.
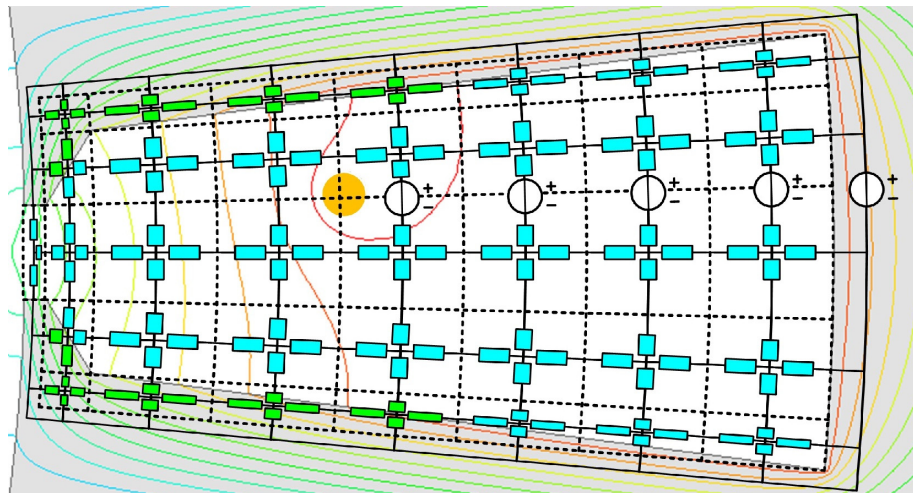
Figure 3.8 Complete magnetic circuit of one conductor in slot.

3.2.4 Solving the MEC

After the MEC is created according to the shape of slot and conductor positions, the next step is to create and solve the corresponding matrices. First, number each branch and node and define the direction of each branch. Taking the magnetic circuit in Figure 3.8 as an example, the node number, branch number and branch direction are shown in Figure 3.9. The slot area is divided

into m rows in radial direction and n columns in tangential direction. Accordingly, the value of total node number N_n is $(m+1)\times(n+2)$, while the total branch number N_b is $[(m+1)-1]\times[2(n+2)-1]+n+2-1$. The number of branches is numbered according to the number of nodes which is connected to it. For each row of nodes except for the last row, there are $[2(n+2)-1]$ branches connected to it. The number of branches is programmed in MATLAB according to the node flowing out of it.
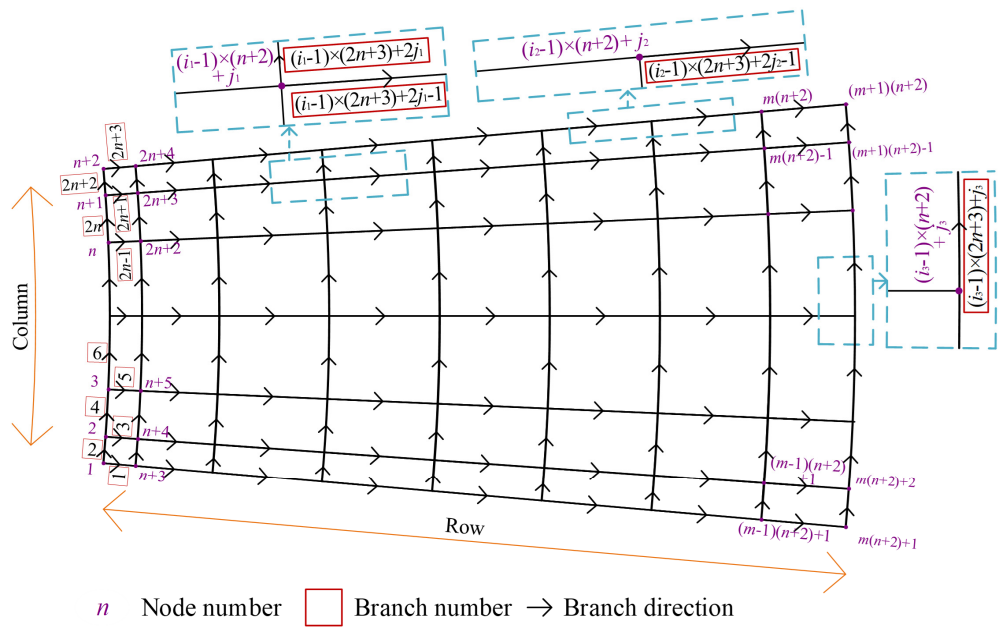
Figure 3.9 Node number, branch number and branch direction of MEC

Then, the incidence matrix should be created. The incidence matrix A can be constructed as a $N_n \times N_b$ matrix. In this matrix, each column number represents the branch with same number, while the row number represents the corresponding node [122]. The incidence matrix A is shown in equation (3.6) and the value of the elements is shown in equation (3.7). In one column, the element value 1 represents that in the corresponding branch, the flux flow from this node, while the element value -1 represents the flux flow into this node, and

the other elements in the column are 0.

The nodes and branches are numbered based on the nodes. The node at row i column j is numbered as $(i-1)\times(n+2)+j$. For each node, the branches that flows out of this node is numbered accordingly. The nodes can be categorized into 4 types: 1) With 2 branches flowing out of it [Node $(i_1-1)\times(n+2)+j_1$], 2) with only one branch flowing out in radial direction [Node $(i_2-1)\times n+j_2$], 3) with only one branch flowing out of it in tangential direction [Node$(i_3-1)\times n+j_3$] and 4) with no branch flowing out of it. The branches that flow out of the node are numbered as demonstrated in Figure 3.9. After the nodes and branches are numbered, fill the values in the incidence matrix A. For example, in branch 3, the branch direction is flowing from node 2 into node $n+4$. Therefore, in column 3, the value of row 2 is 1 and the value of row $n+4$ is -1, while the other elements in column 3 is 0. In this way, the incidence matrix A is built.

$$
A=
\begin{array}{c}
\\
1 \\
2 \\
3 \\
\cdots \\
n+3 \\
n+4 \\
\cdots \\
(m+1)\times(n+2)
\end{array}
\begin{array}{cccccc}
1 & 2 & 3 & 4 & \cdots & m\times(2n+3)+n+1 \\
\left[\begin{array}{cccccc}
1 & 1 & 0 & 0 & \cdots & 0 \\
0 & -1 & 1 & 1 & \cdots & 0 \\
0 & 0 & 0 & -1 & \cdots & 0 \\
\cdots & \cdots & \cdots & \cdots & \cdots & \cdots \\
-1 & 0 & 0 & 0 & \cdots & 0 \\
0 & 0 & -1 & 0 & \cdots & 0 \\
\cdots & \cdots & \cdots & \cdots & \cdots & 0 \\
0 & 0 & 0 & 0 & \cdots & -1
\end{array}\right]
\end{array}
\tag{3.6}
$$

$$
a_{ij}=\begin{cases}1, & \text{when branch } j \text{ flow out of node } i \\ -1, & \text{when branch } j \text{ flow into node } i \\ 0, & \text{otherwise}\end{cases}
\tag{3.7}
$$

Next, the magnetic permeance matrix $\varLambda$ should be built. The magnetic permeance matrix is a $N_b\times N_b$ diagonal matrix, which means all the elements that are not on the diagonal are 0. The value of each element represents the magnetic permeance of the corresponding branch. The value of the magnetic permeances

in each branch is calculated by means of equation (3.3)-(3.5). Substitute the value of magnetic permeances into the branches accordingly, the magnetic permeance matrix Λ can be obtained.

$$\Lambda = \text{diag} \begin{bmatrix} \Lambda_1 & \Lambda_2 & \cdots & \Lambda_{N_b} \end{bmatrix} \tag{3.8}$$

After that, the MMF source branch matrix F_s (an $N_b \times 1$ matrix) should be created. When solving the matrix, the input current is assumed to be 1 A to calculate the flux leakage generated per ampere. The flux leakage generated by input current at any magnitude can be obtained by amplifying the flux leakage per ampere because of the linear permeability of the MEC.

$$F_s = \begin{bmatrix} \cdots & 1 & \cdots & 1 & \cdots & 1 & \cdots & 1 & \cdots \end{bmatrix}^T \tag{3.9}$$

When the number of branches in which the MMF source are specified, the element value at rows with corresponding number in F_s is assigned with 1 while the other elements in the matrix are assigned with 0. In this matrix, the number of elements with value of 1 is determined by the conductor position and mesh division.

Finally, knowing the incidence matrix A, magnetic permeance matrix Λ and MMF source branch matrix F_s, the distribution of magnetic flux can be determined by solving the following equation in order of (3.10)-(3.11)-(3.12):

$$F_n = (A\Lambda A^T)^{-1} A\Lambda F_s \tag{3.10}$$

$$F = A^T F_n \tag{3.11}$$

$$\Phi = \Lambda(F - F_s) \tag{3.12}$$

where F_n is the magnetic potential of each node, F is the magnetic potential drop of each branch, and Φ is the magnetic flux matrix. In the obtained $N_b \times 1$ magnetic

flux matrix $\boldsymbol{\Phi}$, the value at different rows represents the value of magnetic flux in corresponding branches. The equation (3.13) could also be written in expanded form:

$$\begin{bmatrix} \Phi(1) \\ \Phi(2) \\ \vdots \\ \Phi(N_b) \end{bmatrix} = \begin{bmatrix} \Lambda(1) & & & \\ & \Lambda(2) & & \\ & & \ddots & \\ & & & \Lambda(N_b) \end{bmatrix} \left\{ \begin{bmatrix} F(1) \\ F(2) \\ \vdots \\ F(N_b) \end{bmatrix} - \begin{bmatrix} F_s(1) \\ F_s(2) \\ \vdots \\ F_s(N_b) \end{bmatrix} \right\} \tag{3.13}$$

In this way, the flux leakage generated by one conductor is calculated. By repeating this process and applying linear superposition law, the external magnetic flux density at all conductor positions can be calculated. Suppose the number of conductors in the slot is N_{total}. The external magnetic flux density of a conductor is the sum of magnetic flux density generated by the rest of N_{total}-1 conductors at this position. To achieve this goal, firstly, transfer the obtained magnetic flux B at each position into magnetic flux density flux density by:

$$B = \Phi / S \tag{3.14}$$

Φ represents the magnetic flux calculated from (3.13), S denotes the cross-section area of the magnetic permeance.

Suppose the current in conductor number s is expressed in phasor form as $I_s \cdot e^{j\lambda_s}$, where I_s denotes the magnitude of the sinusoidal current waveform in conductor number s, and λ_s denotes the phase of the sinusoidal current waveform in conductor number s. Suppose the tangential component and radial component of external magnetic flux leakage generated by conductor s per Ampere at the position of conductor number z ($s \neq z$) are $B_{\theta A\text{-}s,z}$ and $B_{rA\text{-}s,z}$. Then the magnetic flux density generated by conductor number s at conductor number z is expressed

61

as:

$$B_{\theta\text{-}s,z} = I_s \cdot e^{j\lambda_s} \cdot B_{\theta A\text{-}s,z} \tag{3.15}$$

$$B_{r\text{-}s,z} = I_s \cdot e^{j\lambda_s} \cdot B_{rA\text{-}s,z} \tag{3.16}$$

Therefore, the external magnetic flux density of probe conductor number z can be expressed as the sum of magnetic flux density generated by the rest of the conductors:

$$B_{\theta\text{-}z} = \sum_{s=1}^{z-1} B_{\theta\text{-}s,z} + \sum_{s=z+1}^{N_{total}} B_{\theta\text{-}s,z} = \sum_{s=1}^{z-1} I_s \cdot e^{j\lambda_s} \cdot B_{\theta A\text{-}s,z} + \sum_{s=z+1}^{N_{total}} I_s \cdot e^{j\lambda_s} \cdot B_{\theta A\text{-}s,z} \tag{3.17}$$

$$B_{r\text{-}z} = \sum_{s=1}^{z-1} B_{r\text{-}s,z} + \sum_{s=z+1}^{N_{total}} B_{r\text{-}s,z} = \sum_{s=1}^{z-1} I_s \cdot e^{j\lambda_s} \cdot B_{rA\text{-}s,z} + \sum_{s=z+1}^{N_{total}} I_s \cdot e^{j\lambda_s} \cdot B_{rA\text{-}s,z} \tag{3.18}$$

Consequently, the magnitude of the external magnetic flux density at the position of conductor number z can be expressed as:

$$B_{\text{-}z} = \sqrt{B_{\theta\text{-}z}{}^2 + B_{r\text{-}z}{}^2} \tag{3.19}$$

In this case, the magnitude of the sinusoidal current I_s and the phase of the sinusoidal current waveform λ_s in all the conductors are identical. Therefore, it is not necessary to calculate the phase shift in each conductor. However, it should be noted that the method can be utilized to calculate the magnetic flux density when the magnitude and phase shift in each conductor are different.

Taking conductor No.1 in the slot in as an example, the calculation of the external magnetic flux density at position of conductor No.1 is illustrated in Figure 3.10. The first step is to calculate the magnetic flux density generated by conductor No.2 at the position of conductor No.1 using equation (3.15) and (3.16), then the magnetic flux density generated by conductor No.3, No.4, etc.

After all the conductors are calculated, the external magnetic flux density at the

position of conductor No.1 can be calculated by equation (3.17) and (3.18).

(a)　　　　　　　　　　　　(b)

(c)
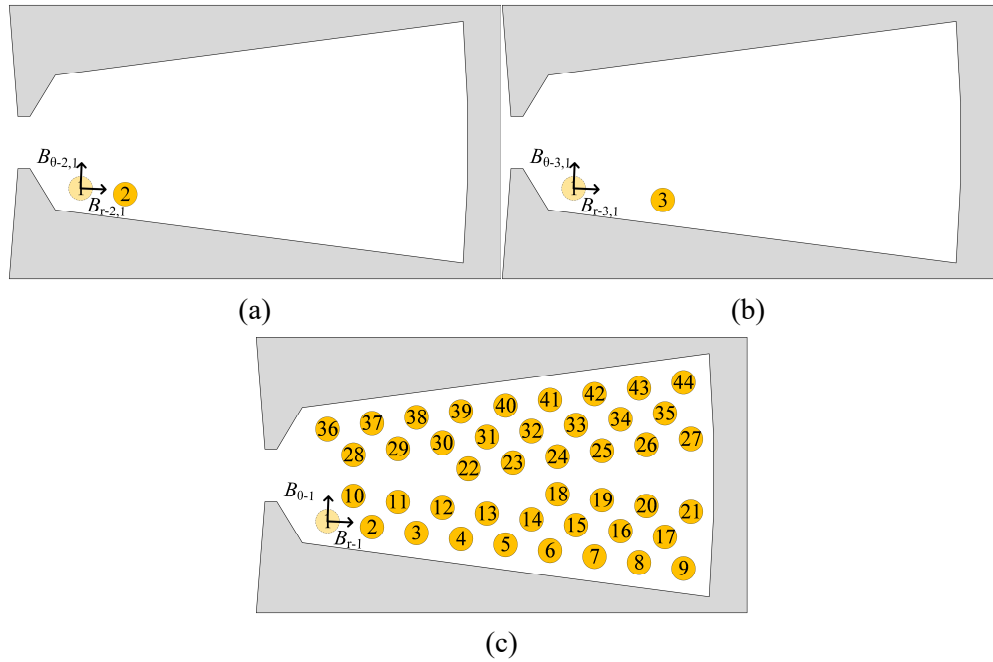
Figure 3.10 External magnetic flux density calculation at the position of conductor No.1. (a) Generated by conductor No. 2. (b) Generated by conductor No. 3. (c) Overall

When the magnitude of external magnetic flux density is sinusoidal, the

proximity loss of a conductor can be calculated as:

$$P_{\mathrm{p}} = \frac{\pi l \sigma d_0{}^4 (2\pi f B_{\mathrm{m}})^2}{128} \tag{3.20}$$

where f represents the frequency of the sinusoidal magnetic flux density

waveform, B_{m} represents the magnitude of the external magnetic flux density of

each conductor.

Therefore, by calculating the external magnetic flux density and

substituting the value into equation (3.20), the proximity loss could be calculated.

The proximity loss calculation process is summarized in Figure 3.11.
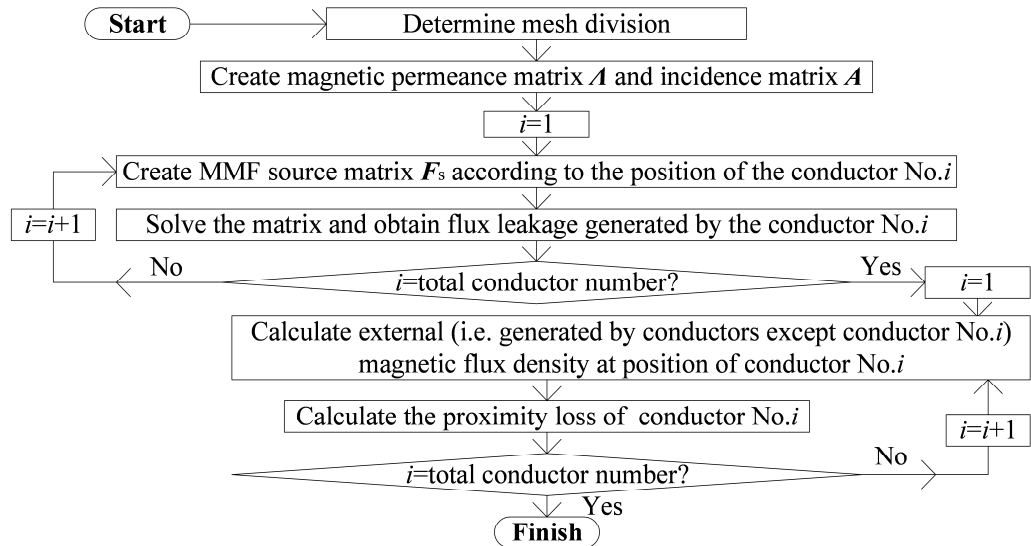
Figure 3.11 Proximity loss calculation process.

3.3 Finite Element Comparison

Numerical FEA simulations are carried out to validate the proposed methodology using the structure of the baseline machine, and flux leakage and proximity losses of the slot are calculated by means of MEC and FEA.

3.3.1 Computational Time and Accuracy

In the MEC model considered for the baseline machine, the slot area is divided into 49 columns and 90 rows to illustrate the capability of obtaining precise flux leakage distribution and proximity loss using the proposed method. The MEC model was developed in MATLAB environment while ANSYS Electronics was used for FEA. The mesh density in MEC model and in FEA model are set to be basically the same. Using MEC, it took approximately 16 seconds in total to compute the losses for various input currents. When additional input current cases need to be calculated, no extra time is required beyond the initial 16 seconds. In contrast, in FEA, over 16 minutes is required to calculate

64

the losses in one case alone, and it took about 40 minutes in total to simulate 4 cases simultaneously.

Different mesh division is also simulated, and the results are compared with the one-slot FEA model as shown in Figure 3.12. It can be observed that the average copper loss error in each conductor slightly decreases when the number of mesh element increases. The maximum average error among all is approximately 2% with a calculation time of about 0.4 seconds, while the minimum average error is about 0.9% which required 9.2 seconds for calculation.

(a)   (b)
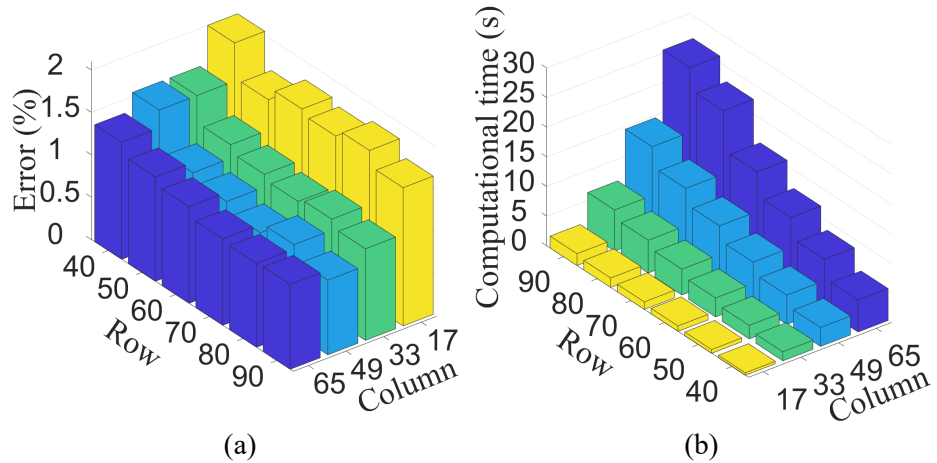
Figure 3.12 Comparison of MEC model with different mesh element number. (a) Average error in copper loss of each individual conductor. (b) Computational time.

3.3.2 Magnetic Flux Leakage

As mentioned previously, the magnetic flux in the slot domain is calculated by superposition of magnetic flux due to each individual conductor. In order to evaluate the accuracy of the proposed MEC model, the magnetic flux due to different conductors in the slot domain are calculated and compared with the FEA model accordingly. In Figure 3.13, the colour-shaded map of magnetic flux density calculated by means of MEC and FEA for the conductors No. 1, No. 23 and No. 44 are compared. In addition, distribution of magnetic flux density

resulted by all conductors calculated by MEC and FEA are also compared in Figure 3.14. It can be observed that the overall estimated flux leakage has an excellent agreement with the FEA results.

The input current in the conductors is a sinusoidal waveform, and its RMS value and frequency are 21.7 A and 1000 Hz, respectively.
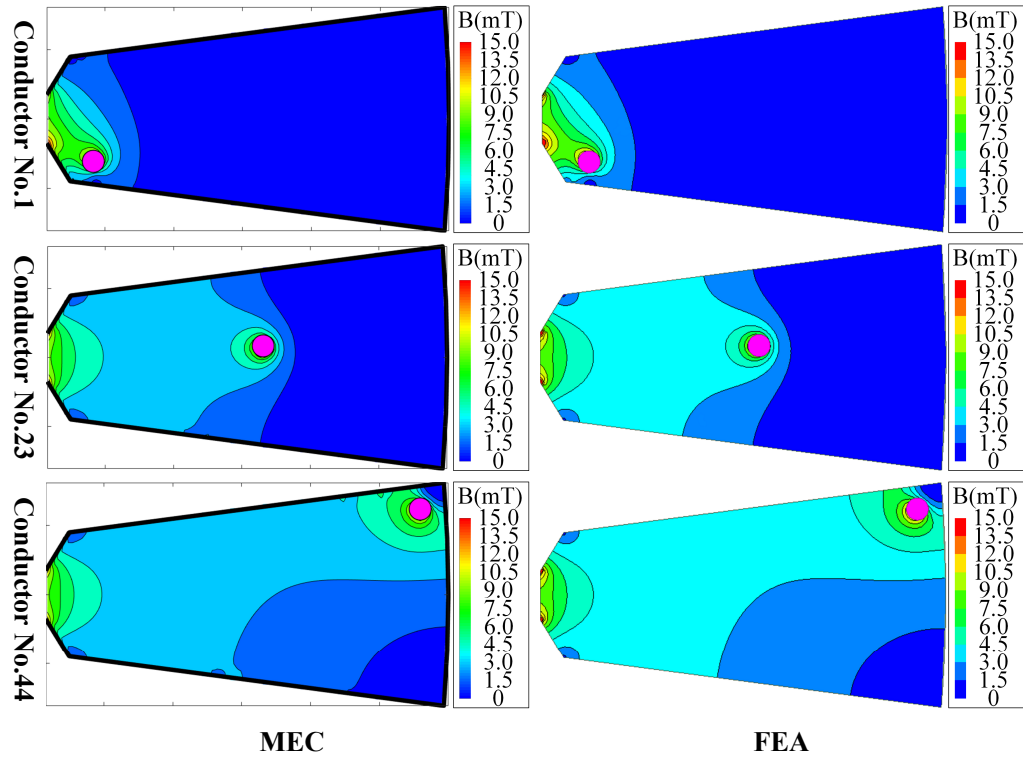
Figure 3.13 Distribution of magnetic flux density generated by a single conductor computed by MEC and FEA.
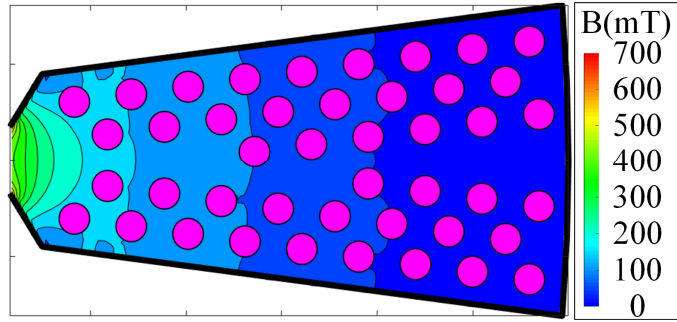
(a)
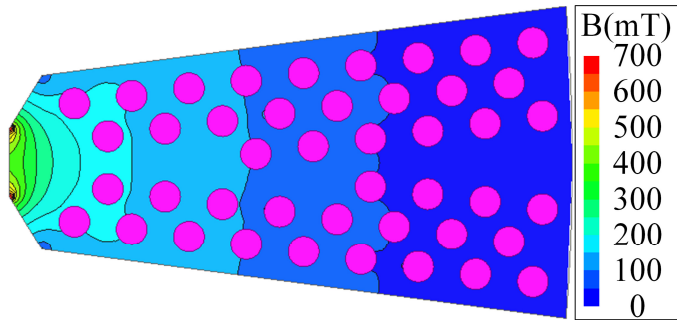
(b)

Figure 3.14 Magnetic flux leakage distribution in MEC (a), and in FEA (b).

3.3.3 Copper Loss

Table 3.4 Comparison of copper loss in conductors near the slot at 1000 Hz.

Conductor number	1	2	3	4	10
Copper loss in FEA (W)	1.812	1.519	1.229	0.993	1.839
Copper loss in MEC (W)	1.801	1.521	1.221	0.985	1.817
Deviation (%)	0.607	-0.132	0.651	0.806	1.196
Conductor number	11	12	13	22	
Copper loss in FEA (W)	1.374	1.100	0.890	0.981	
Copper loss in MEC (W)	1.372	1.097	0.882	0.975	
Deviation (%)	0.146	0.273	0.899	0.612	

The copper losses consist of different components, including DC loss, circulating current loss, proximity loss, and skin effect loss. In the baseline machine, the circulating loss component is mitigated by applying full transposition as stated earlier in Section 3.1.1 Baseline Machine Parameters. In

addition, the skin effect loss of the baseline machine is calculated according to [24]. The calculated value of the skin effect loss is very small and negligible. As result, the applicable loss components are primarily DC copper loss and proximity loss. The sum of DC copper loss, computed from $P_{DC} = I^2 R,$ and proximity loss determined through MEC is compared with copper loss in FEA.

The copper loss of the conductors near the slot opening are computed and compared in Table 3.4. The DC copper loss of each conductor is 0.524 W, which means the proximity loss accounts for a significant portion of total copper losses.

The deviation in proximity loss will be reflected in the deviation of total copper loss. It is observed that the deviation percentage of the copper loss for each individual conductor computed through the proposed approach is found negligible when compared with FEA.

Table 3.5 Copper loss values in one slot for different frequencies.

Frequency	400	800	1200
Copper loss in FEA (W)	25.6	33.3	46.1
Copper loss in MEC (W)	25.7	33.4	46.0
Deviation (%)	-0.45	-0.27	0.05

In addition, compares the values of total copper losses in one slot at different frequencies computed by MEC and FEA. As ca be seen, the estimated copper losses computed by proposed method closely align with FEA results.

It is worth mentioning that the input current in the conductors is a sinusoidal waveform, and its RMS value is 21.7 A, and the frequency varies from 400 Hz to 1200 Hz. It can be observed the deviation between the copper loss calculated by MEC and by FEA is less than 0.5 %, which is completely negligible.

3.4 Experimental Test

3.4.1 Experimental Setup

For experimental validation, a segment of the machine stator comprising two slots, referred as 'motorette', was constructed to assess the viability of proposed method. The shape and dimensions of the slots of the motorette is the same as the baseline machine. The motorette, named as Motorette #1, is made of B35A250 silicon iron (SiFe) steel with the thickness of 0.35 mm aimed to reduce the eddy current loss.

In addition, to duplicate the identical positions of individual conductors as considered in the MEC and FEA models, two molds were built by means of a 3D printer [70] – See Figure 3.15 (a). These molds were composed of Nylon Fiberglass and can withstand temperature up to 180°C. These molds then were employed to wind Motorette #1 as shown in Figure 3.15 (b). The motorette is essential to induce flux leakage and subsequently generate the proximity loss component within the test experimental setup.

(a)   (b)
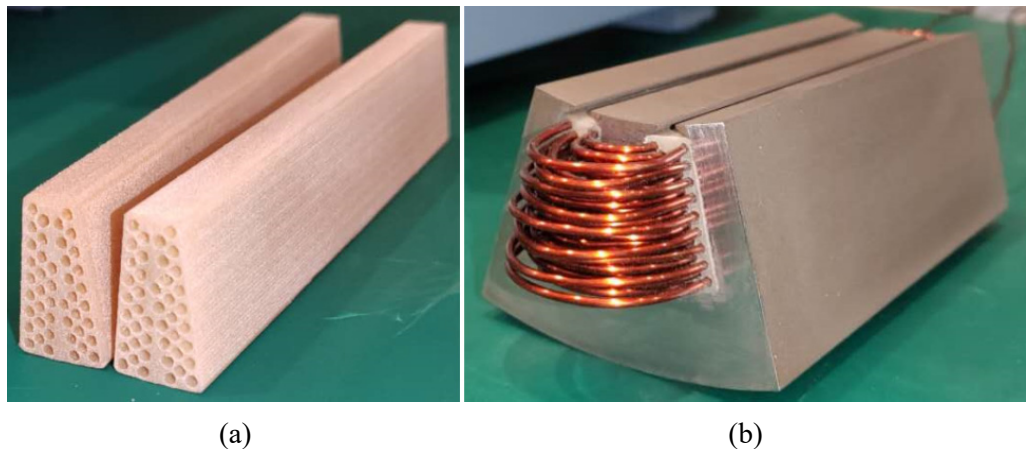
Figure 3.15 3D-printed molds (a), wounded Motorette #1 in experiment (b).
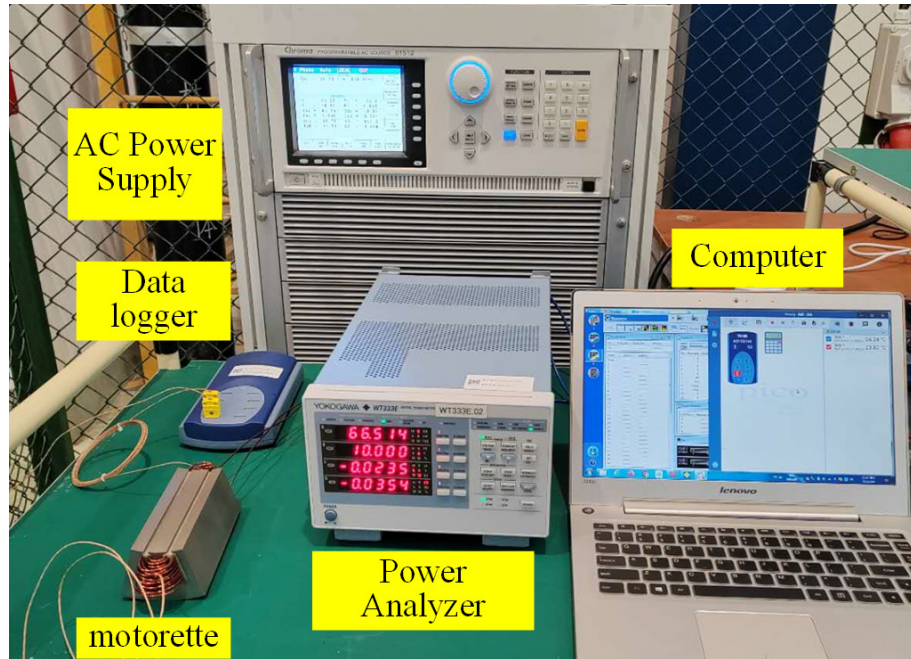
(a)
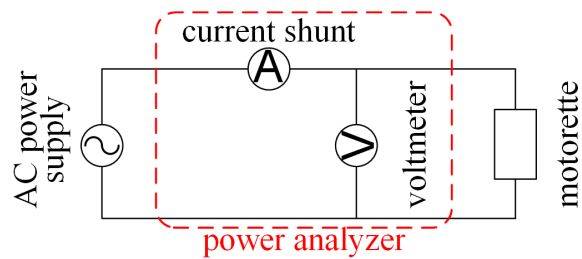
(b)

Figure 3.16 Actual experiment setup (a), schematic diagram of the experimental setup (b).

Table 3.6 Instruments employed during experiment test.

Instrument	Model	Function description
AC power supply	Chroma 61512	Supply variable frequency voltage
Power analyzer	WT 333E	Measure power loss
K-type thermocouple	PICO	Monitor winding temperature
Data logger	PICO-TC08	Collect the temperature values
Oscilloscope	KEYSIGHT DSOX2024A	Collect the voltage and current values
Current probe	FLUKE i400s	Measure the current
Voltage probe	KEYSIGHT N2791A	Measure the voltage

The experiment setup and its corresponding electrical circuit schematic are shown in Figure 3.16. The instrument descriptions and their function in the experiment are reported in Table 3.6. It should be noted that the power losses measured by the power analyser encompass the total copper joule losses, both DC and AC components, and iron core losses. To derive the AC copper loss, which represents the proximity loss within the context of this study, it is not possible to segregate these loss components precisely within the experiment. For this reason, an additional test was conducted to measure the B-H curves and B-P curves of the laminated steel used for building the iron core ring at different frequencies [109], as depicted in Figure 3.17.
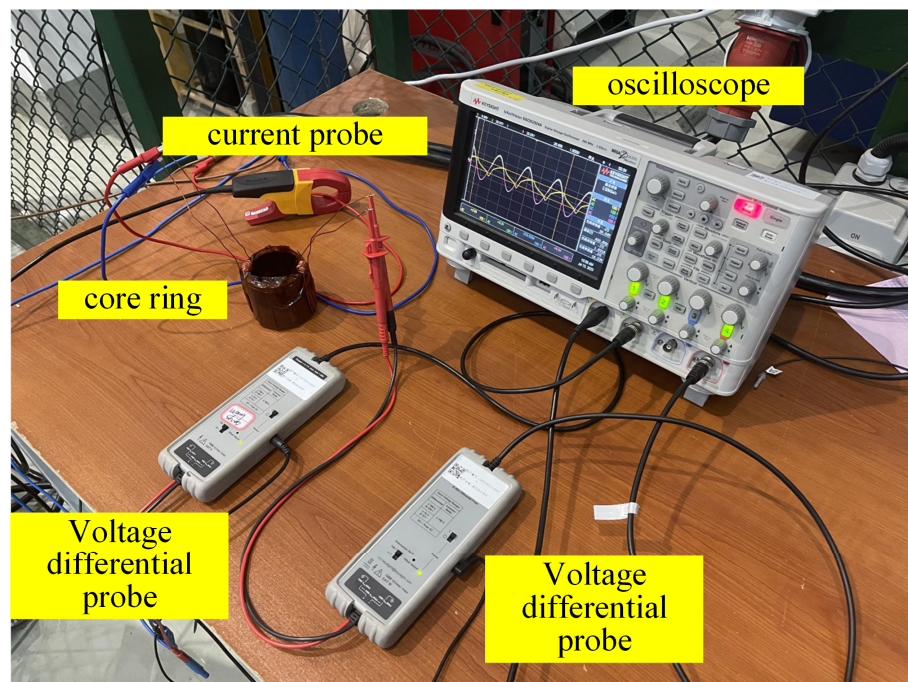
Figure 3.17 Experimental setup for magnetic and loss characterization of iron core.

3.4.2 Comparison Between Calculation and Experiment

The measured B-H curves and B-P curves are illustrated in Figure 3.18 (a). The instruments used in this experiment and their function are presented in

Figure 3.18 (b). These dataset serves as the input properties during the formula curve fitting process to determine the Bertotti's core loss coefficients for calculation of core loss P_{Fe} in 2D-FEA. In this way, a more precise core loss data is obtained.
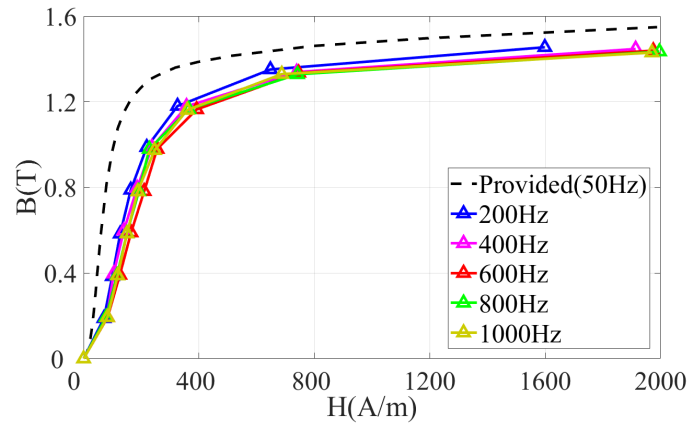
(a)
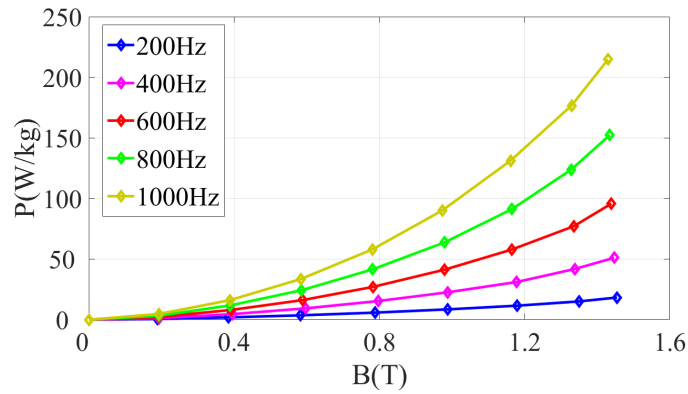
(b)

Figure 3.18 Measured (a) B-H curves and (b) B-P curves of B35A250.

Therefore, the measured copper loss can be obtained from subtracting the core loss from the experimentally measured loss. Subsequently, the measured AC to DC resistance ratio $K_{AC\text{-}tested}$ can be expressed as [55]:

$$K_{AC\text{-}tested}=P_{copper\text{-}tested}/P_{DC\text{-}tested}=\frac{P_{tested}-P_{Fe}}{P_{DC\text{-}tested}} \tag{3.21}$$

On the other hand, the calculated AC to DC resistance ratio K_{AC} is obtained as follow:

1) Calculate AC copper loss P_{AC}. As it is mentioned previously, the skin effect loss in this case is very small and therefore neglected. Therefore, the AC copper loss only involves proximity loss, which is calculated by proposed mesh-based MEC method. One-slot MEC model is utilized for AC copper loss calculation.

2) The DC copper loss is deduced from measuring the DC resistance of the winding R_{DC} and rms value of the current injected into the winding I_{rms} ($P_{DC}=R_{DC}I_{rms}^2$).

$$K_{AC}=P_{copper}/P_{DC}=\frac{P_{AC}+R_{DC}I_{rms}^2}{R_{DC}I_{rms}^2} \qquad (3.22)$$

The comparison of the calculated AC to DC resistance ratio K_{AC} and measured AC to DC resistance ratio $K_{AC\text{-tested}}$ is shown in Figure 3.19. The calculated total loss and the measured total loss are in good match. It could be observed that the error increases along with the increase of frequency, and the largest error is approximately 4.9%. The error may be caused by the instrument inaccuracy such as unexpected harmonics due to AC power source or the core loss calculation errors.

The experiment suggests that when the laminated iron core is beyond saturation, the permeability of the iron core can be regarded as linear and linear superposition law is applicable. Besides, the proposed method in this paper is proved to be feasible for proximity loss prediction, as well as flux leakage estimation. The proposed method will be used to quickly estimate the AC copper loss of different windings to maximize the efficiency of the electrical machine.
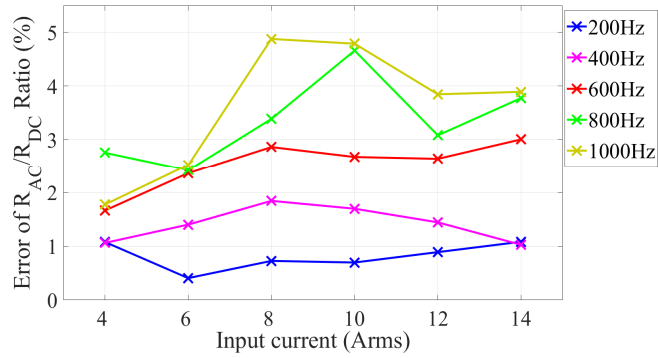
(a)
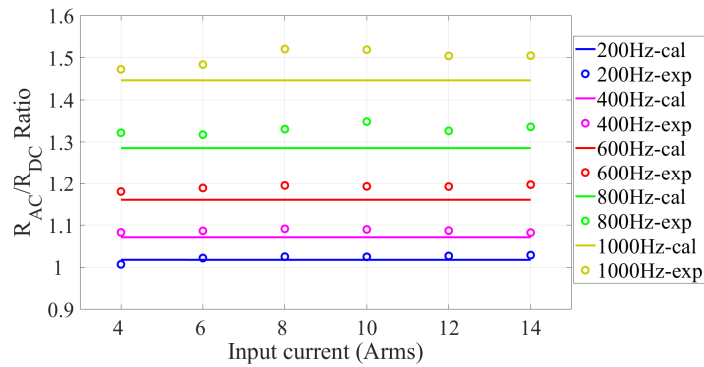
(b)

Figure 3.19 Comparison of calculated and measured AC/DC resistance ratio (a) and error percentage of AC/DC resistance ratio (b).

3.5 Summary

This study presents an innovative technique for evaluating flux leakage and proximity loss in electrical machines. In the proposed method, mesh-based MEC is exploited, yielding a result for both flux leakage and proximity loss. The copper loss comparison between the whole-machine model and the one-slot model illustrates that the one-slot model, in which the permanent magnet is not taken into account, can be adopted to predict the proximity loss of an electrical machine when the stator is not highly saturated. The individual conductor flux leakage, overall flux leakage, and proximity loss of each conductor calculated by the proposed method show a good alignment with FEA, which proves the

capacity of the proposed method in achieving similar accuracy in proximity loss estimation with FEA. In addition, an experimental test is carried out for further verification of the accuracy of the MEC model. The calculation error is within 4.9%, which remains in an acceptable range. This confirms the high viability and precision of the proposed method.

The application of the mesh-based MEC model for precise calculation of flux leakage and proximity loss of an electrical machine has promising prospects. The concept of linear superposition allows for fast flux leakage and proximity analysis in different input current situations. Although infinite stator permeability is assumed in the thesis, the proposed method still has the potential to involve stator saturation by adopting frozen linear permeability. The proposed method has considerable potential in solving issues related to flux leakage, including fast circulating current loss calculation and winding optimization aiming at AC copper loss minimization.

Chapter 4 Circulating Current Calculation With MEC

Except for proximity loss, the circulating current loss is another significant component of AC copper loss. In this chapter, an advanced methodology for circulating current calculation is introduced. Using the aforementioned mesh-based MEC model, strand inductance and back-EMF are calculated accounting for slot shapes and conductor positions. The modeling process is illustrated by applying it to a PMSM, while it also can be applied to diverse types of electrical machines.

The proposed method effectively addresses the need for extensive computation on circulating current in diverse winding structures in optimization processes aiming at loss reduction. Using mesh-based MEC model, the leakage inductance is calculated, accounting for slot shapes and conductor positions, achieving improved accuracy over conventional 1-D MEC method while its computational time slightly increases. Besides, for winding optimization which requires circulating current loss calculation on large scale of winding connections, the circulating current loss of each winding connection can be obtained by solving the associated electric circuit with new winding connection. In this process, leakage inductance only needs to be calculated once, substantially reducing the computational time and effectively catering to the requirements of winding optimization.

4.1 Problem Specification

4.1.1 Machine and Winding Configuration

The specification of the machine is shown in Table 3.1, the same machine used for illustration of proximity loss calculation. The difference is that in this case, the assumption of eliminated circulating current is not involved. The objective of the study is to develop a method for calculation of the strand current and copper loss in electrical machines with parallel strands. Figure 4.1 (b) specifies the detailed winding configuration, including the conductor shape and positions. Round conductors are utilized in the winding, with their strand number marked on it. The number of parallel strand m in this winding is 25, and the number of turns n is 2. Inward-directed winding is used as an example, and the number of conductors in the outward-directed winding should be mirror-reversed. The winding configuration of different phases are completely symmetrical. The connection between the conductors and the relationship between the conductors and the strands is depicted in Figure 4.1 (c). The elements in this circuit represent a conductor segment, and a strand is composed of the conductors connected in series.

It is worth noting that the skin effect loss and proximity loss in the study are not considered in the MEC model used in this study. This is because the primary focus of the study is the circulating current, and the AC resistance changed by skin effect loss and proximity loss may influence the circulating current. In this study, the diameter of the conductor is 1.5 mm, which is sufficiently small to ignore the impact of skin effect and proximity.
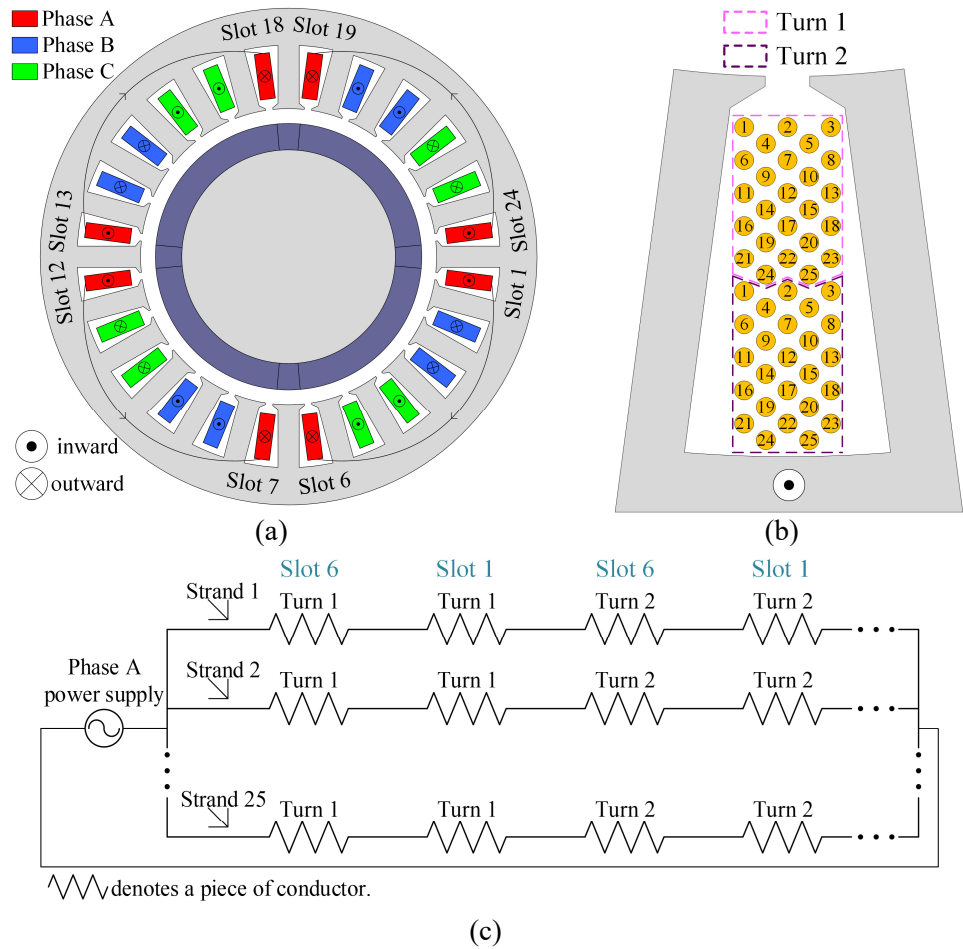
Figure 4.1 Baseline machine geometry. (a) Overall structure of baseline machine. (b) Conductor configuration in the slot. (c) Circuit connection of strands in Phase A.

4.1.2 Assumptions

In this study, the parameters which are related to the magnetic flux leakage, such as strand inductance and back-EMF, are calculated using MEC. The MEC model is developed involving the following assumptions:

1) The permeability of the stator and rotor core is infinite.

2) The influence of skin effect and proximity loss inside the conductor is ignored.

3) The magnetic properties of the PM are assumed to be linear and described as [123]:

$$B=\mu_0\mu_{\text{PM}}H+\mu_0 M_{\text{PM}} \qquad\qquad (4.1)$$

where H denotes the magnetic strength of the external field, M_{PM} is the

magnetization of the PM.

4) The direction of magnetization of the PM are radial.

5) The effect of end-winding is neglected.

Based on the assumptions, the parameters of the machine are calculated

using mesh-based MEC in the following discussion. The mesh-based MEC is

regarded to hold the potential to provide accurate analysis besides analytical

method and FEA [124]. The parameters can be calculated by solving it and the

summing linked magnetic flux.

4.2 Methodology

4.2.1 Electric Circuit

The uneven distribution of strand current is caused by the difference in

strand inductance and back-EMF, which is determined by their conductor

positions in the slot. To reflect the strand imbalance, an electric circuit involving

the strand branches is presented. By modelling each strand in Figure 4.1 (c) with

a branch, the electric circuit of the electrical machine is developed as shown in

Figure 4.2. In each strand branch, the circuit is composed of 1 resistance, $3m$

inductance and 1 voltage induced by back EMF. There is a mutual inductance

between any 2 strand branches. Consequently, the inductance of a strand branch

is composed of 1 self-inductance, m-1 mutual inductances caused by the strands

in the same phase, and $2m$ mutual inductances caused by the strands in other

phases.

In this circuit, R represents the resistance of the strand and E represents the back-EMF of the strand, and their subscript denotes the strand number. L denotes mutual inductances of 2 strands in the same phase and strand self-inductances. M denotes the mutual inductance of two strands in different phases. Subscripts of L and M denote the number of 2 strands.

Each strand corresponds to one equation, resulting in $3m$ equations in total. They can be written in matrix form as:

$$\begin{bmatrix} U_A \\ U_B \\ U_C \end{bmatrix} = \begin{bmatrix} R_A & & \\ & R_B & \\ & & R_C \end{bmatrix} \begin{bmatrix} I_A \\ I_B \\ I_C \end{bmatrix} + \begin{bmatrix} L_A & M_{AB} & M_{AC} \\ M_{AB} & L_B & M_{BC} \\ M_{AC} & M_{BC} & L_C \end{bmatrix} \begin{bmatrix} dI_A/dt \\ dI_B/dt \\ dI_C/dt \end{bmatrix} + \begin{bmatrix} E_A \\ E_B \\ E_C \end{bmatrix} \quad (4.2)$$

The expanded element matrices in (4.1) is expressed as:

$$U_A = [U_A(t) \quad U_A(t) \quad \cdots \quad U_A(t)]^T \quad (4.3)$$

$$R_A = \text{diag}[R_{A1} \quad R_{A2} \quad \cdots \quad R_{Am}] \quad (4.4)$$

$$I_A = [I_{A1}(t) \quad I_{A2}(t) \quad \cdots \quad I_{Am}(t)]^T \quad (4.5)$$

$$L_A = \begin{bmatrix} L_{A11} & L_{A12} & \cdots & L_{A1m} \\ L_{A12} & L_{A22} & \cdots & L_{A2m} \\ \vdots & \vdots & \ddots & \vdots \\ L_{A1m} & L_{A2m} & \cdots & L_{Amm} \end{bmatrix} \quad (4.6)$$

$$M_{AB} = \begin{bmatrix} M_{AB11} & M_{AB12} & \cdots & M_{AB1m} \\ M_{AB12} & M_{AB22} & \cdots & M_{AB2m} \\ \vdots & \vdots & \ddots & \vdots \\ M_{AB1m} & M_{AB2m} & \cdots & M_{ABmm} \end{bmatrix} \quad (4.7)$$

$$E_A = [E_{A1}(t) \quad E_{A2}(t) \quad \cdots \quad E_{Am}(t)]^T \quad (4.8)$$

The matrices in phase B and phase C resemble those in phase A.
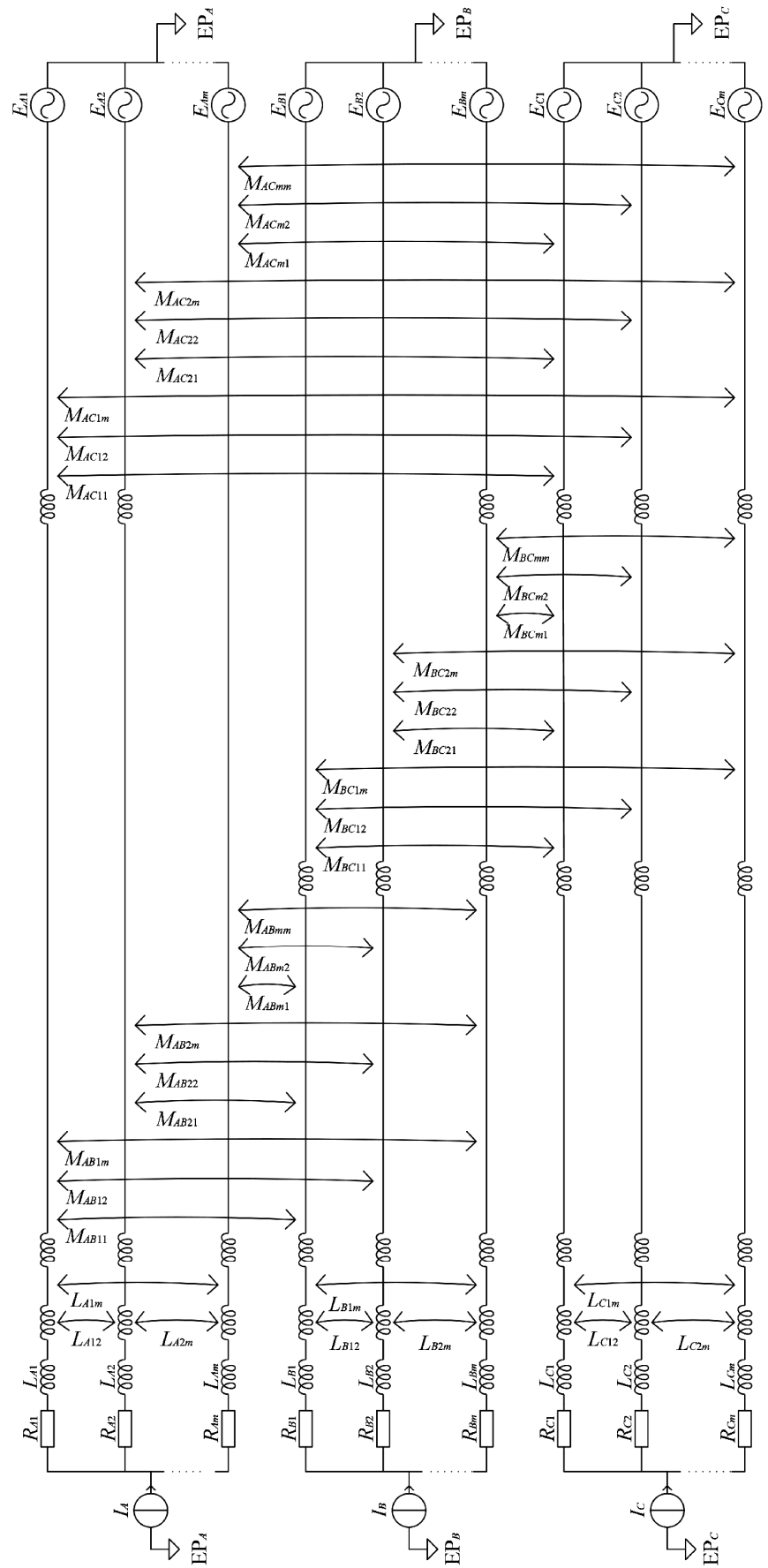
Figure 4.2 Electric circuit of the machine including individual strands.

If only consider the steady state, the terminal voltage, phase current and back-EMF can be expressed in phasor form using complex number. Subsequently, the fundamental component of (4.1) and (4.2) is written as:

$$\begin{bmatrix} U_A \\ U_B \\ U_C \end{bmatrix} = \left\{ \begin{bmatrix} R_A & & \\ & R_B & \\ & & R_C \end{bmatrix} + j\omega \begin{bmatrix} L_A & M_{AB} & M_{AC} \\ M_{AB} & L_B & M_{BC} \\ M_{AC} & M_{BC} & L_C \end{bmatrix} \right\} \begin{bmatrix} I_A \\ I_B \\ I_C \end{bmatrix} + \begin{bmatrix} E_A \\ E_B \\ E_C \end{bmatrix} \tag{4.9}$$

$$U_A = [U_A e^{j\omega t} \quad U_A e^{j\omega t} \quad \cdots \quad U_A e^{j\omega t}]^T \tag{4.10}$$

where j denotes the imaginary unit, $U_A^{(1)}$, $I_A^{(1)}$ and $E_A^{(1)}$ denotes the fundamental component of voltage, strand current and back EMF. By solving equation (4.9), the fundamental component of strand current can be obtained, while harmonics of strand current can also be obtained similarly.

In summary, the calculation process of the proposed method is illustrated in Figure 4.3.
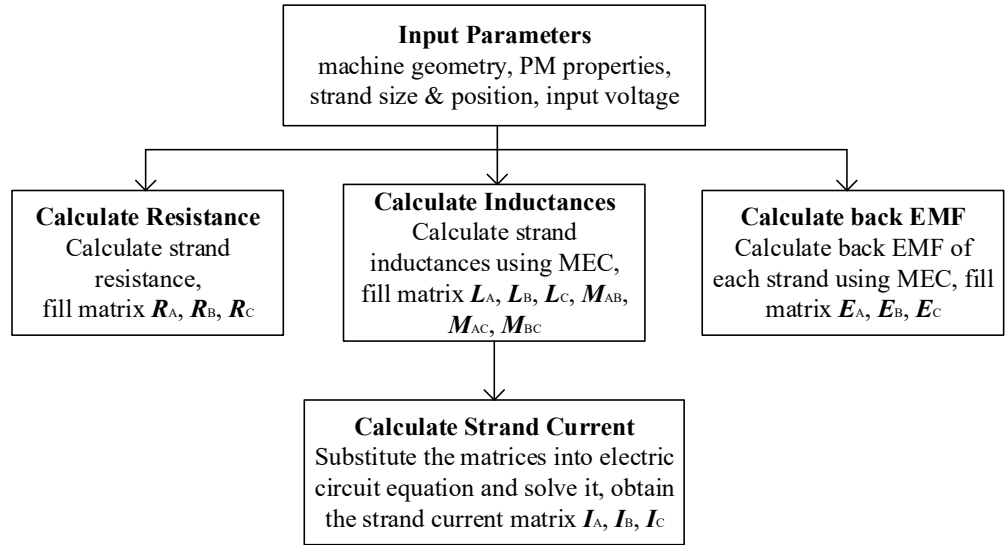
Figure 4.3 Circulating current calculation process of the proposed method.

4.2.2 Strand Parameter Calculation

To solve equation (4.9), the parameters of the strands, i.e. the elements in

matrix R, L, M, and E, need to be obtained first. After the value in these matrices are obtained, the strand current can be easily obtained. In this section, the calculation process of parameters in the matrices is illustrated.

a) Resistance R

The elements in resistance matrix R are calculated by:

$$R_{A1}=\cdots=R_{Am}=\frac{Q}{3}\frac{4nl}{\sigma\pi d_0{}^2} \tag{4.11}$$

The DC resistance is calculated and integrated into the equation. The skin and proximity effect are not considered in the study, so the AC resistance is equal to DC resistance.

b) Phase inductance matrix L

To calculate the inductance of a strand composed of multiple turns, it is more convenient to determine the inductance of one turn in the first place and then formulate the inductance of strand. In the following discussion, the MEC model used for inductance of one turn and the equation of forming the inductance of multiple turns using inductance of each single turn is presented.

The mesh division and corresponding MEC to calculate the inductance of one turn is shown in Figure 4.4 (a). According to area, the overall inductance is separated into airgap inductance L_δ and leakage inductance L_σ. The separation is feasible because despite the position of the conductor, the value of L_δ remains constant [79]. Only the leakage inductance varies with the conductor's positions. Besides, the inductance of airgap part can be calculated using the MEC model of the machine structure without PM. This is because the impact of surface-mounted PMs on the direction of the magnetic flux in the airgap area is negligible,

as well as the airgap inductance L_δ. The overall magnetic flux can be regarded as the linear superposition of the magnetic flux generated by each single conductor and by PM, therefore the inductances are calculated separately using different MEC.

In Figure 4.4 (b), the MEC of calculating L_δ is presented. The value of F is substituted with 1 A for convenience. After solving the MEC in Figure 4.4 (b), the value of L_δ can be obtained by summing up the magnetic flux in linked magnetic permeances, which are highlighted with red line in the direction noted with arrow. This is feasible only when the current in the conductor is 1 A and there is only one turn.

In Figure 4.4(c), the MEC model for L_σ calculation of two different conductors in a slot is presented. For the convenience of illustration, an example of rectangular slot is presented instead of the circular sector slot. In the model, the current in source conductor is 1 A and the current in probe conductor is 0. The dotted line in Figure 4.4(c) represents the mesh elements of the slot. The MMF source is added to the branches in tangential direction between the conductor position and the bottom of stator yoke as described in [125]. After solving the circuit, the self-inductance of the source conductor can be obtained by adding up the magnetic flux in the magnetic permeance linked to the source conductor, while the mutual inductance between the source conductor and probe conductor can be obtained by adding up the magnetic flux in magnetic permeance linked to the probe conductor. An example of magnetic permeance linked to the source conductor and probe conductor is highlighted with the arrow

in different colors in the Figure 4.4(c).

(a)

(b)

(c)
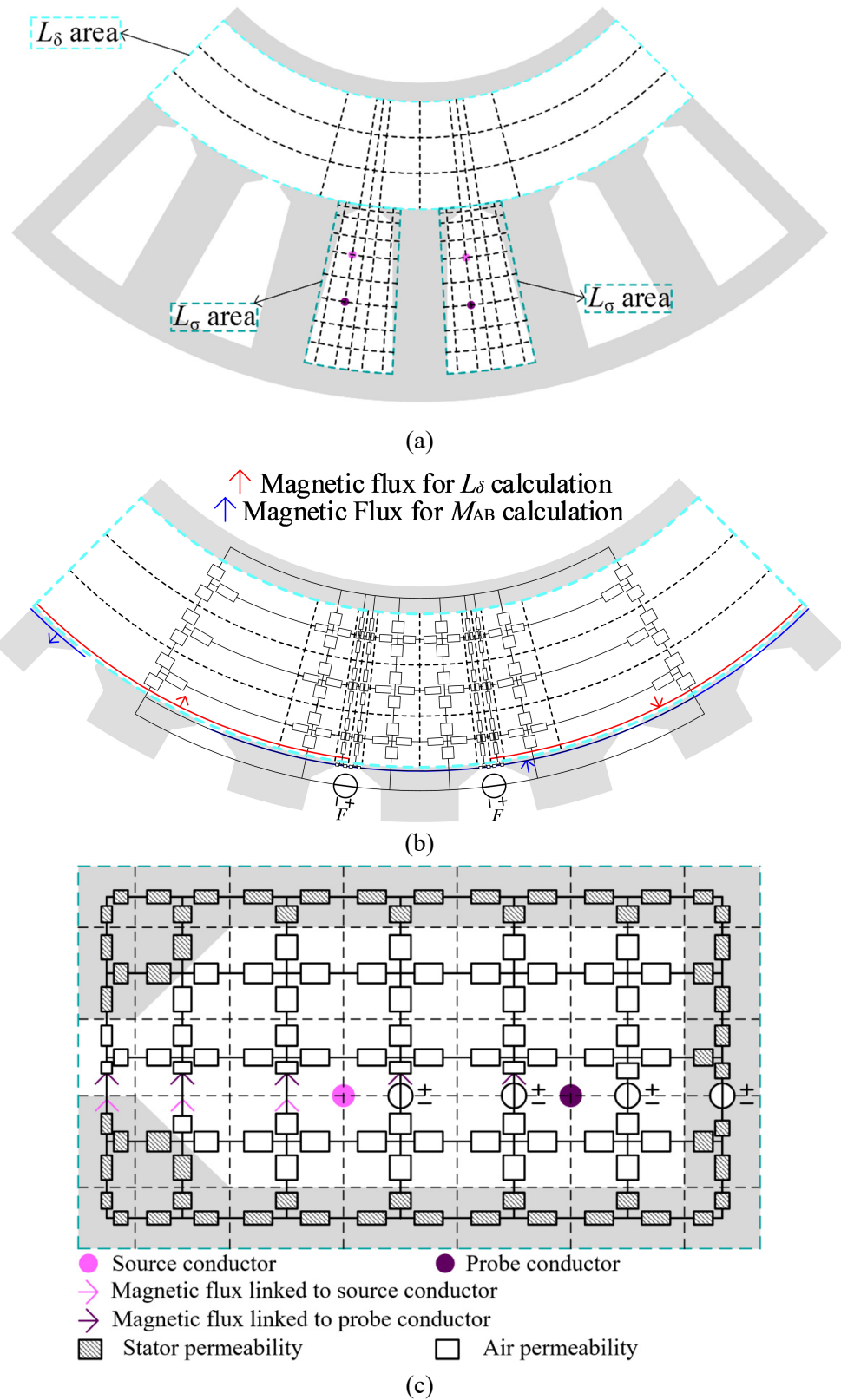
Figure 4.4 MEC for inductance of strands in the same phase. (a) Overall MEC for inductance calculation of one turn. (b) MEC for airgap inductance L_δ. (c) MEC for flux leakage inductance L_σ.

After the mutual and self-inductance between each single conductor is calculated by repeating the procedure above, the mutual and self-inductance between each single conductor is calculated, the mutual and self-inductance of the strands can be calculated. The mutual inductance between the conductor of strand u turn v and the conductor of strand p turn q can be expressed as the sum of airgap inductance and leakage inductance:

$$L_{uv\text{-}pq}=N_{\mathrm{p}}(L_{\delta}+2L_{\sigma\_uv\text{-}pq}) \tag{4.12}$$

where L_{σ} denotes the leakage inductance of conductors.

Subsequently, the mutual inductance between strand u and strand p in the same phase can be deduced by adding up the mutual inductance of each turn [24]:

$$L_{u\text{-}p}=\sum_{v=1}^{n}\sum_{q=1}^{n}L_{uv\text{-}pq} \tag{4.13}$$

Repeating the process, the elements in phase inductance matrix $\boldsymbol{L}$ are calculated.

c) Phase mutual inductance matrix $\boldsymbol{M}$

The MEC model used for calculating the mutual inductance of strands in different phases is presented in Figure 4.4(b). The MEC for airgap inductance L_{δ} calculation and for mutual inductance between two conductors in different phases $M_{\mathrm{conductor}}$ are identical. The difference is the linked magnetic permeance, because of the conductor in different phase are in different slot. The magnetic permeance linked to the conductor in another phase is highlighted with blue line and arrow. In the baseline machine, the strands in different phases are in different slots, so it is feasible to calculate the airgap inductance of these strands only and ignore the leakage inductance.

The mutual inductance between 2 strands in different phases, i.e. the element in matrix **M**, can be obtained using the equation simplified from equation (4.13):

$$M = n^2 M_{conductor} \tag{4.14}$$

It is worth mentioning that the proposed method could also be implemented on the windings of different phases in the same slot. In that case, the strand mutual inductance can be obtained by calculating the airgap and leakage mutual inductance of conductors separately, similar to equation (4.12) and (4.13).

d) Back-EMF matrix **E**

The MEC for calculation of back-EMF in different strands is illustrated in Figure 4.5. In the MEC, one pair of poles is modeled. The PM area is divided in tangential direction, and the value of the magnetic flux sources is calculated by integrating the magnetic flux through the mesh element [126]. The radial component of magnetic flux density on the surface of magnets, which determines the MMF source in the MEC model, is calculated as [127]:

$$B_r = \mu_0 \sum_{k=1,3,5,\ldots}^{\infty} (kN_p)(-C_k R_m^{kN_p-1} + D_k R_m^{-kN_p-1})\cos(kN_p\theta) \tag{4.15}$$

where C_k and D_k are constants to be determined by the characteristics of the machine.

For the conductor at different positions, the back EMF is obtained by adding up the magnetic flux in magnetic permeance linked to the conductor, as illustrated in Figure 4.5.
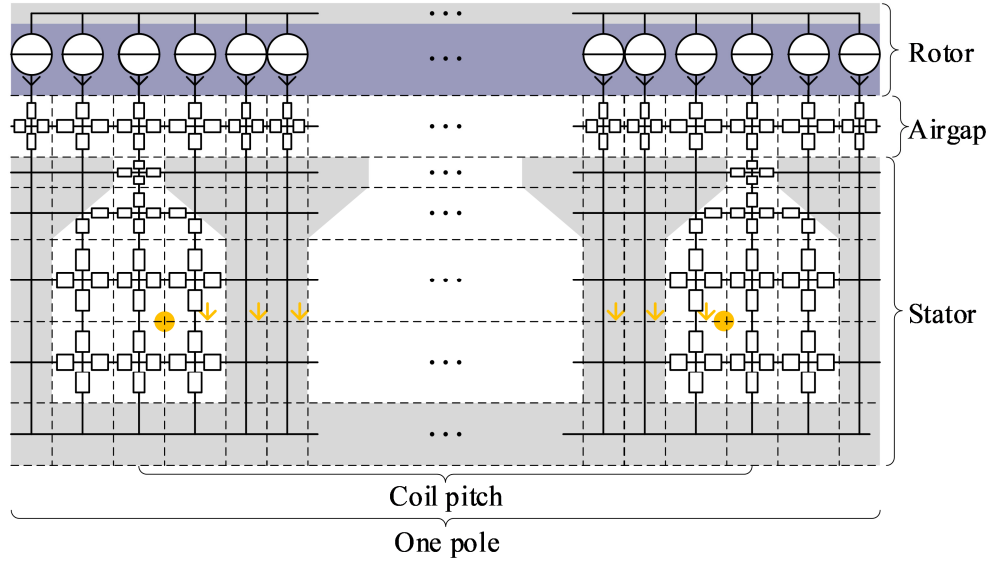
Figure 4.5 MEC for calculation of back-EMF in different strands.

After the flux linkage of conductor strand p turn q at k^{th} order $\lambda_{pq\text{-}k}$ is obtained, the harmonics of back EMF of the strand p can be obtained by adding up the back EMF linked to each turn:

$$E_{q\text{-}k}=N_{\text{p}}\times jk\omega \sum_{q=1}^{n} \lambda_{pq} \tag{4.16}$$

4.3 Calculation Results

In this section, the proposed method is implemented on the baseline machine, and the results are compared with FEA for validation. The analysis is conducted using MEC model, FEA model with linear stator permeability (linear FEA) and FEA model with nonlinear stator permeability (nonlinear FEA). The FEA model is shown in Figure 4.6. Besides, the computational time of MEC is apparently shorter than FEA. All these models are conducted on the same computer, and the computational time of these models are: MEC model for 18 seconds, linear FEA model for 20 minutes per period, and nonlinear FEA model for 23 minutes per time period.

88
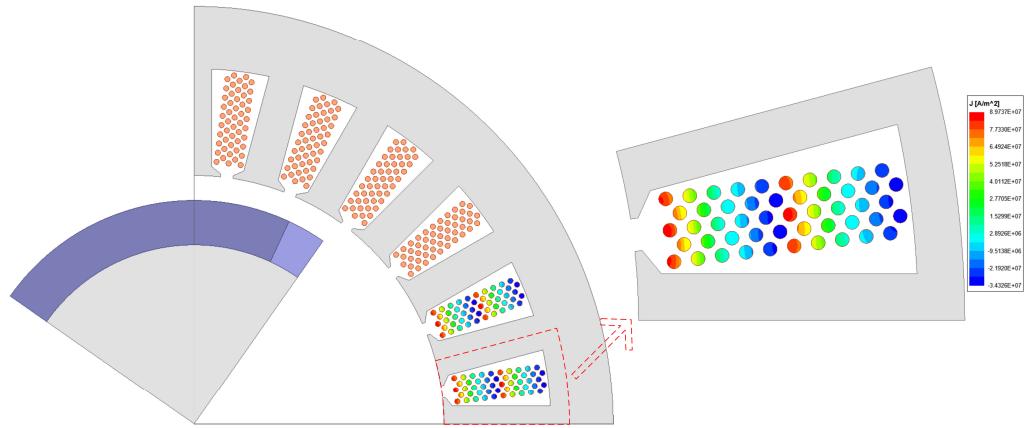
Figure 4.6 Instantaneous current density calculated from linear FEA model.

4.3.1 Strand Parameters

a) Phase Inductance Matrix **L**

The inductances of the strands in the same phase calculated by MEC and by linear FEA, as well as the error percentage, are illustrated in Figure 4.7. In Figure 4.7 (a) and Figure 4.7 (b), the height of the bar represents the value of mutual inductance between these 2 strands noted on x-axis and y-axis. In Figure 4.7 (c), it can be observed that the maximum error of the strand inductance calculated from MEC is within 2.5 %, showing close alignment of the inductances calculated from MEC and from linear FEA. The agreement validates the precision of leakage inductance calculation using MEC.
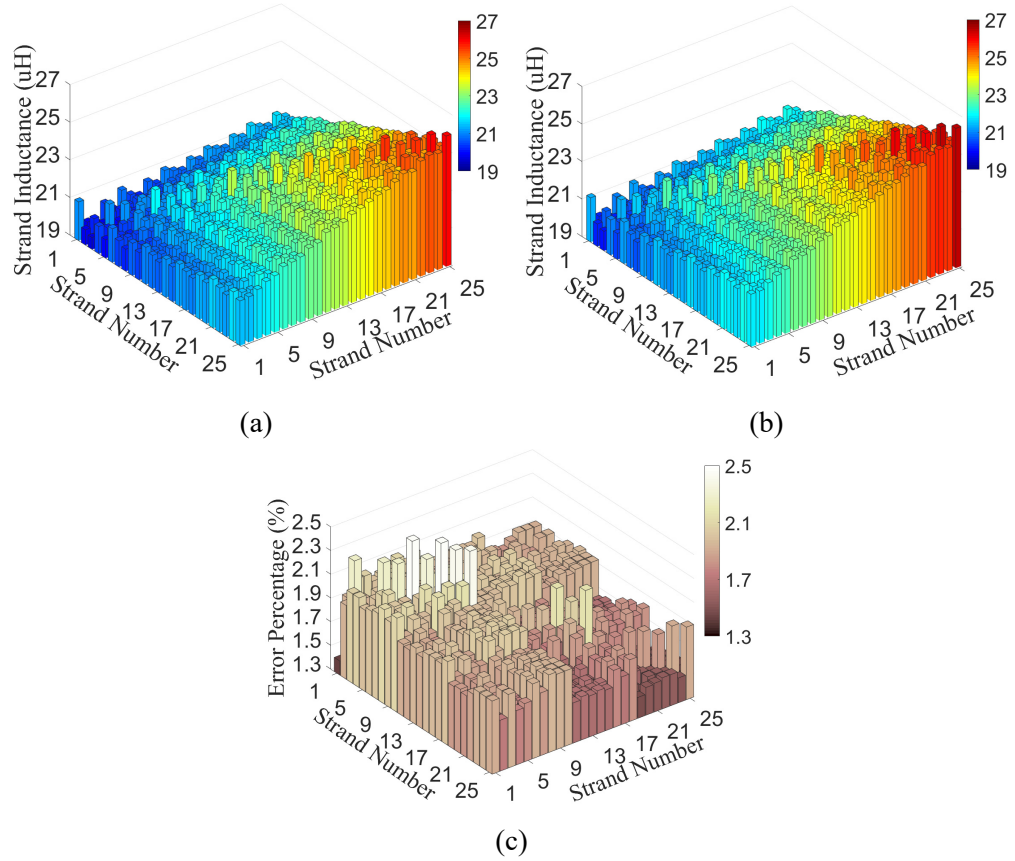
Figure 4.7 Inductance of the strands in the same phase (i.e. elements in self-inductance matrix **L**). (a) Result calculated by MEC. (b) Result calculated by FEA. (c) Error percentage of MEC result.

b) Phase Mutual Inductance Matrix **M**

The mutual inductances of strands in two different phases calculated by MEC and linear FEA are shown in Figure 4.8 (a). Since the leakage inductance is not considered, these inductances calculated from MEC are completely identical as it is highlighted with the grey bar. The difference of inductances calculated by linear FEA is almost negligible (within 0.3 %), validating the feasibility of ignoring the leakage inductance in the strand inductance in different phases. The maximum error of mutual inductance of strands in different phases is with 2.9 % as depicted in Figure 4.8 (b), showing a good agreement with FEA.
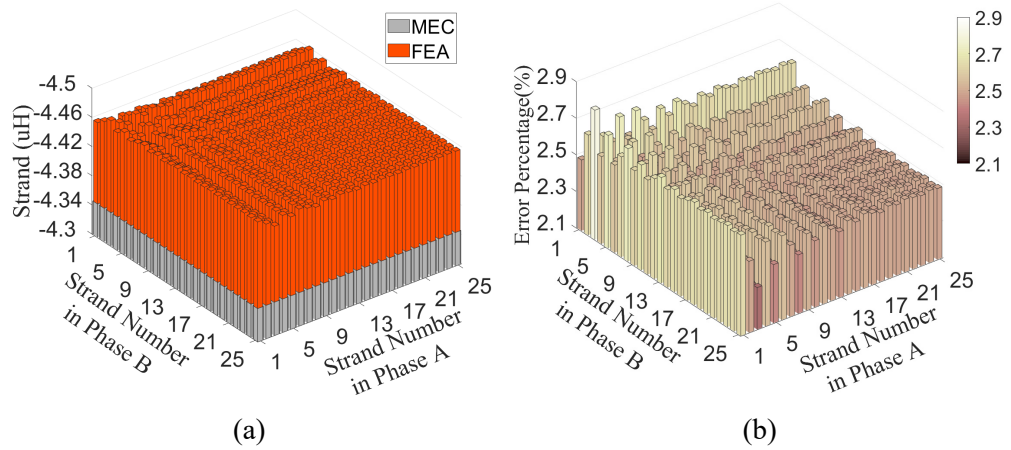
Figure 4.8 Comparison of strand mutual inductance of in different phases. (a) Result calculated by FEA and MEC. (b) Error percentage of MEC.

c) Back EMF Matrix **E**

The harmonics of back-EMF calculated by MEC and by FEA is shown in Figure 4.9. On the one hand, the back-EMF in different strands is almost identical in the baseline machine, which can be observed in both MEC and FEA. Therefore, in the baseline machine, the influence of PM on circulating current is negligible. The conclusion is also proved in [108], [128]. On the other hand, the value calculated by MEC is in good agreement with FEA. The error of 1st and 3rd component of back-EMF is 3 % and 8 %. For the other harmonics, the error percentage rises, but the magnitude of these harmonics is very small, reducing the impact on strand current to almost negligible.
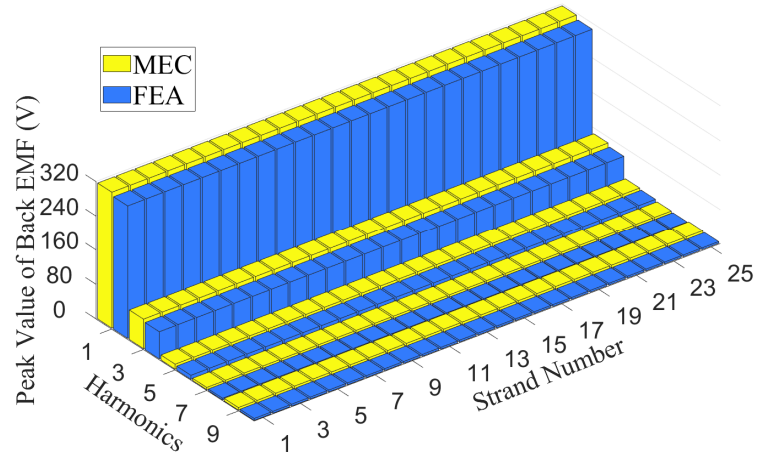
Figure 4.9 Harmonics of back EMF in different strands calculated in linear FEA model
and in MEC model.

4.3.2 Strand Current

Substitute the calculated strand parameters into equation (4.9) and solve it,
the magnitude and phase of the strand current can be obtained. Furthermore, the

RMS strand currents calculated by the proposed method, linear FEA model and

nonlinear FEA model are compared.

The currents in each strand calculated by the MEC model, linear and

nonlinear FEA models are shown in Figure 4.10. The strand current calculated

from the proposed method and linear FEA model are in very good agreement in

both magnitude and phase. It is also worth mentioning that the harmonics of the

strand current calculated from MEC model and linear FEA model are almost

negligible, while the harmonics in strand current in nonlinear FEA model is

significant. Therefore, it could be concluded that in this case, the harmonics of

strand currents are mainly caused by the saturation in the baseline machine.

Proper approaches such as frozen permeability method can be adopted to involve

the saturation effect to enhance the precision of the calculated strand current by

MEC.
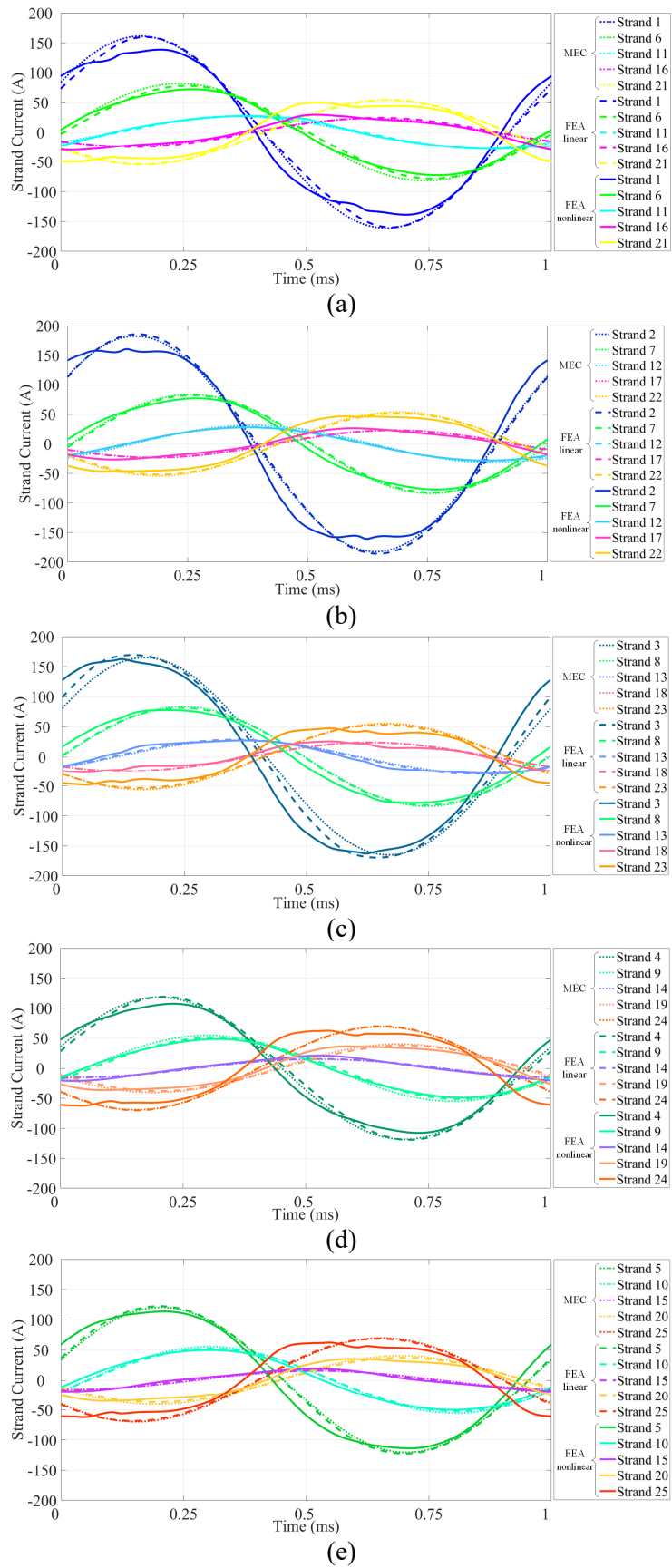
Figure 4.10 Strand current result calculated from MEC model, linear FEA model and nonlinear FEA model. (a) Strand 1, 6, 11, 16, 21. (b) Strand 2, 7, 12, 17, 22. (c) Strand 3, 8, 13, 18, 23. (d) Strand 4, 9, 14, 19, 24. (e) Strand 5, 10, 15, 20, 25.

The RMS current in each strand calculated from different models is shown in Figure 4.11. For strands with larger RMS current (strands 1 to 5), the average error between the MEC model and the linear FEA model is 2.4 %, and the average error with the nonlinear FEA model is 4.3%. This indicates high accuracy of the proposed method for these critical strands. For strands with lower RMS current (strands 6 to 25), the average error between the MEC model and the linear FEA model is 3.7 %, and the average error with the nonlinear FEA model is 7.4 %. Although these error percentages are relatively higher, the impact on the total copper loss is minimal due to the lower copper losses of these strands. Overall, it is sufficiently accurate to calculate loss caused by unevenly distributed strand current using MEC model.
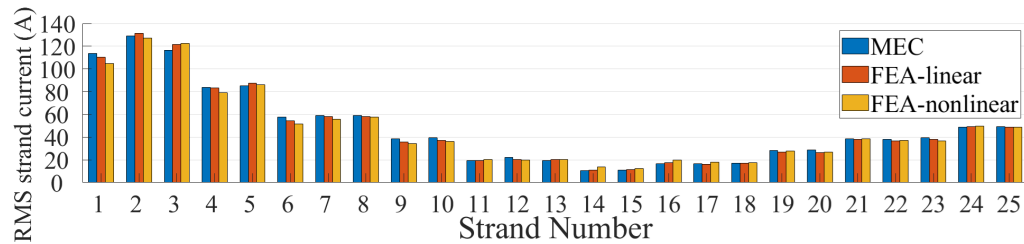
Figure 4.11 RMS strand current calculated by MEC model, linear FEA model and nonlinear FEA model.

4.4 Experimental Test

4.4.1 Experimental Setup

A part of the baseline machine stator (motorette) is built for experimental validation as it is shown in Figure 4.12. Using Motorette #2, the magnetic flux leakage and leakage inductance can be generated similarly to the baseline machine. The focus of the experiment is the verification of the critical procedures of the proposed model, including the electric circuit equation (4.9) for strand

current calculation and the MEC model for leakage inductance calculation. The influence of the rotor on circulating current is not involved in the experiment, because its impact on circulating current is insignificant [108], [75].

A long motorette (Motorette #2 Long) and A short motorette (Motorette #2 Short) are built. The axial length of Motorette #2 Long is 130 mm while that of Motorette #2 Short is 60 mm as shown in Figure 4.12(b), while the end-windings are identical as shown in Figure 4.12 (c) to extract the active length inductance.
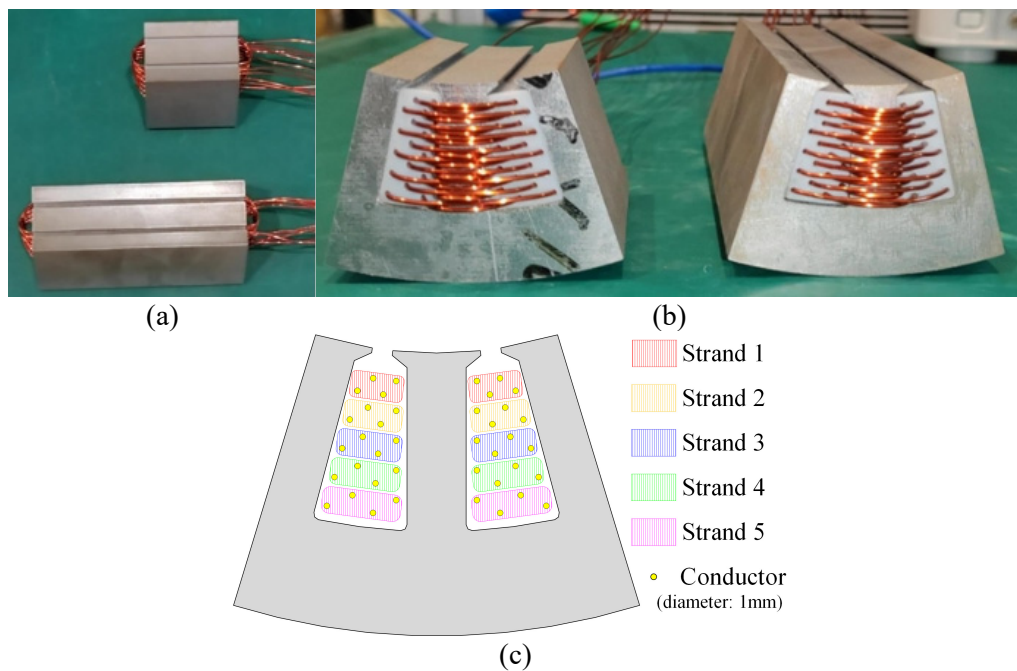
Figure 4.12 Motorette #2 for experimental validation. (a) Structure and strand distribution. (b) Axial view. (c) Radial view.

The conductor is made of copper, and its diameter is 1 mm, to keep skin effect and proximity negligible in the test and keep the experiment focus on circulating current. The Motorette #2 is made of B35A250 silicon iron (SiFe) steel with the thickness of 0.35 mm aimed to reduce the eddy current loss. Inside the slot, there are 3D-printed Nylon Fiberglass molds to hold the precise positions of individual conductors. These plastic molds are solid and can

withstand temperatures up to 180°C.

The experimental setup of inductance and strand current is shown in Figure 4.13. A variable frequency AC power supply, Chroma 61512, is used as the power source. A precise power analyzer, WT 333E, is used to measure the precise value of magnitude and phase of the voltage and current for inductance measurement. The oscilloscope KEYSIGHT DSOX2024A, which is connected to current probe FLUKE i400s and voltage differential probe KEYSIGHT N2791A, is used to collect the magnitude and phase data of strand current.
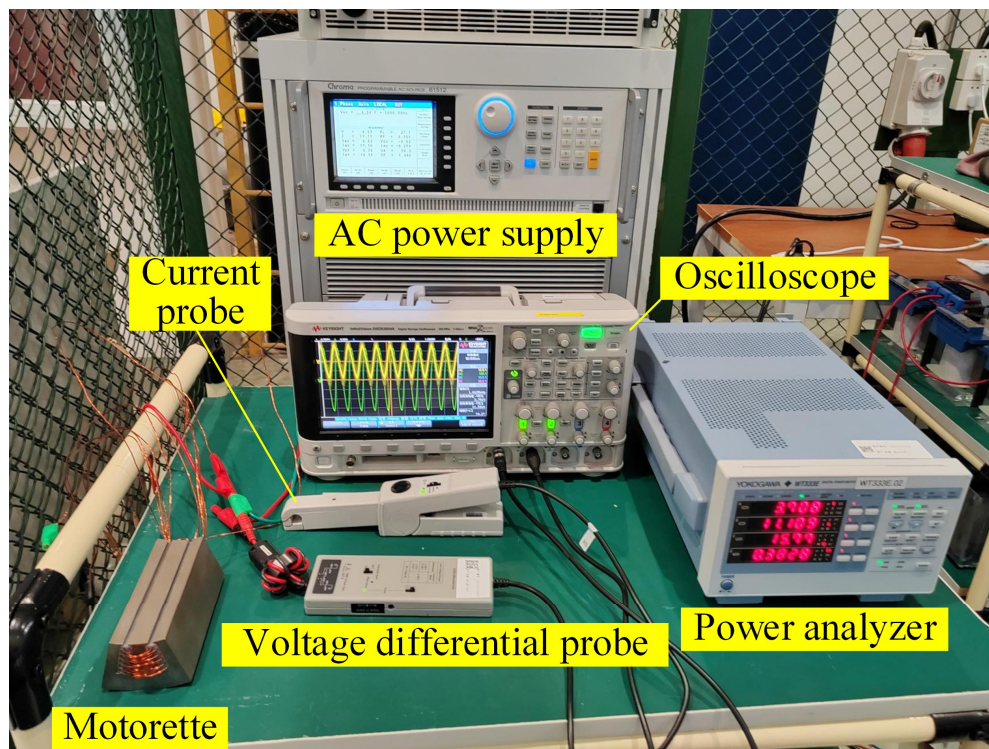
Figure 4.13 Inductance and circulating current experiment setup.

4.4.2 Experiment Procedure and Data Process

As shown in Figure 4.14, there are 2 tests in the experiment. The first part of the experiment is to measure the self- and mutual strand inductance. The first step of the test is measuring the self-inductance of the strands. For example, to measure the self-inductance of strand 1, connect strand 1 to the AC power source,

supply a sinusoidal voltage and then measure the voltage and current of this strand with power analyzer. Subsequently, the self-inductance of strand 1 could be obtained from:

$$L_{\text{self\_1}} = \frac{\sin(\theta_1)|U_1|}{2\pi f|I_1|}$$

(4.17)

where $L_{\text{self-1}}$ represents the measured inductance of strand 1, $|U_1|$ denotes the magnitude of the measured voltage, $|I_1|$ denotes the magnitude of the measured current, θ_1 denotes the phase shift between the measured voltage and measured current and f represents the frequency of the measured voltage and current. All these data can be directly acquired from the power analyzer.

As for the measurement of mutual inductance between 2 strands, the data is collected by connecting these 2 strands in series and obtain the total inductance L_{series} similar with equation (4.17). Subsequently, the mutual inductance between these 2 strands is obtained. For instance, the mutual inductance $L_{1\text{-}2}$ can be obtained by:

$$L_{1\text{-}2} = \frac{L_{\text{series\_1-2}} - L_{\text{self\_1}} - L_{\text{self\_2}}}{2}$$

(4.18)

The next step is to separate the inductance of active length and end-winding. Assume the measured inductance matrix of Motorette #2 Long and the Motorette #2 Short are $\boldsymbol{L}_{\text{long}}$ and $\boldsymbol{L}_{\text{short}}$, the axial lengths of the cores are l_{long} and l_{short}, the inductance of the active length and end-winding of the Motorette #2 Long can be obtained from:

$$\boldsymbol{L}_{\text{long\_active}} = \frac{\boldsymbol{L}_{\text{long}}\text{-}\boldsymbol{L}_{\text{short}}}{l_{\text{long}}\text{-}l_{\text{short}}} \times l_{\text{long}}$$

(4.19)

$$\boldsymbol{L}_{\text{end}} = \boldsymbol{L}_{\text{long}}\text{-}\boldsymbol{L}_{\text{long\_active}}$$

(4.20)
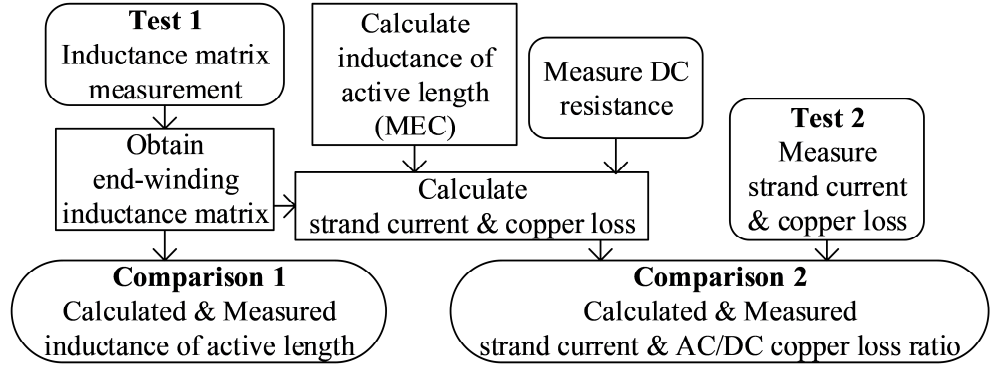
Figure 4.14 Experimental flowchart for validation of the proposed method.

The inductance of active length is compared with the value calculated from MEC for validation, while the inductance of end winding is introduced into the electric circuit equation for correction when the strand current is calculated. It is worth noticing that the inductance calculated by MEC model involves 2 leakage inductance components and 1 inductance component representing the air area above the slot opening, similar to Equation (4.12).

The second part of the experiment is to test the strand current. The strands are connected in parallel, and their terminal is connected to the AC power supply. The strand current is tested using the current probe, and the voltage is measured with the voltage differential probe to identify the phase of strand current.

After the test, tested and calculated values of the circulating current factor K_{cir} are obtained and compared. The circulating current factor K_{cir}, which is used to quantify the circulating current loss, is defined as:

$$K_{cir} = \frac{\sum_{p=1}^{m} I_p^2 R_p}{P_{DC}} \tag{4.21}$$

where I_p denotes the RMS value in strand No.p, R_p denotes the DC resistance of strand No.p, m denotes the strand number. In this case, m is set at 5. P_{DC} is calculated using the measured DC resistance of each strand.

As for the strand currents, Fourier decomposition is applied to identify the magnitudes and phases of the tested data. Subsequently, the tested magnitudes and phases are compared with those calculated from the electric circuit equation (4.9).

4.4.3 Result Comparison

The inductance matrix of active length calculated by MEC and tested in experiment is shown in Figure 4.15, as well as the error of results from MEC.

In Figure 4.15 (a) and Figure 4.15 (b), it can be observed that the strand at the bottom of the slot has the largest value of inductance. Besides, the tested inductance value is larger than the calculated value. This is because the value of the inductance is very small, and it is very sensitive to the length of the conductor. The length of conductor inside the motorettes is determined, while the influence of the conductor out of the motorettes is not negligible.

The error of the inductance calculated by MEC is shown in Figure 4.15 (c). The maximum error of inductance reaches 5.1 %, which is an acceptable considering the influence of the conductor outside the motorette. The inductance calculated by MEC closely aligns with the experiment, which proves the effectiveness of calculating inductance using MEC.
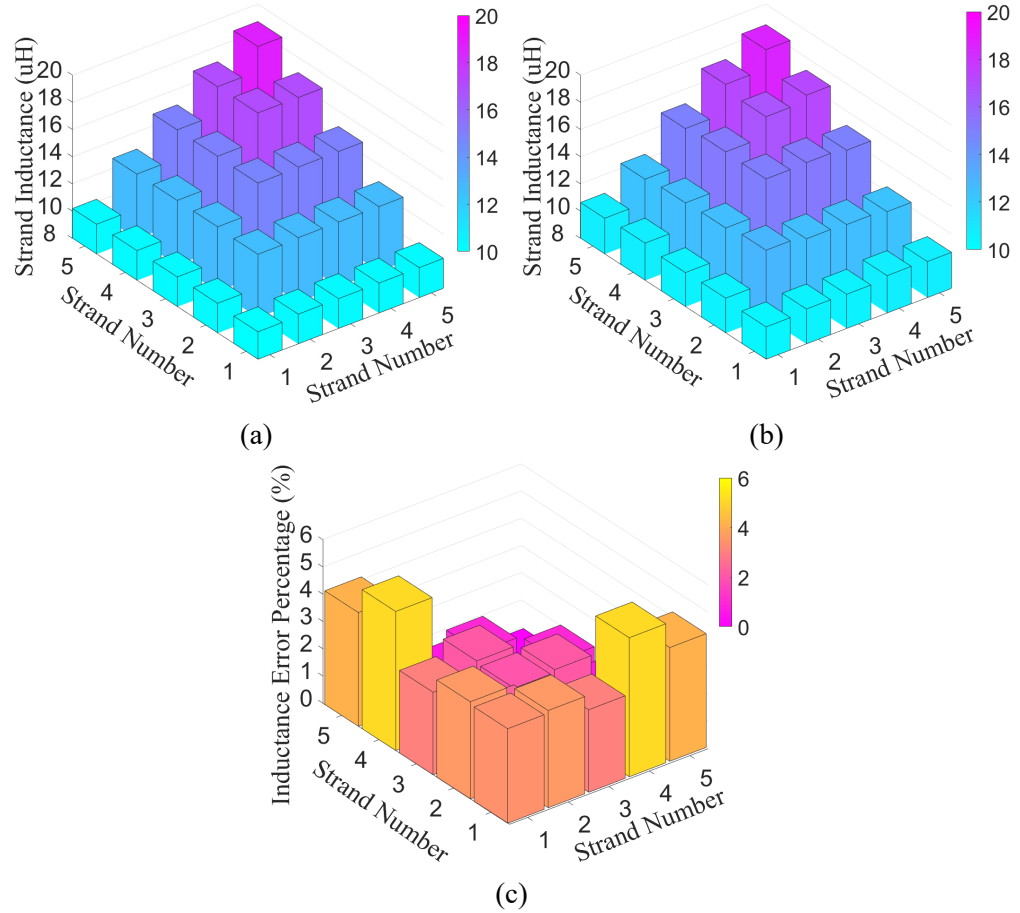
Figure 4.15. (a) Strand inductance of the experimental setup calculated by MEC. (b) Measured strand inductance. (c) Error percentage of MEC result.

The circulating current factor K_{cir} calculated by MEC and test in experiment is shown in Figure 4.16 (a). The calculated and tested results demonstrate a close match. At 600 Hz, the error is remarkably low at 1.4 %, while the error reaches its maximum at 5.6 % as the frequency increases to 1000 Hz, remaining within an acceptable margin. Besides, the calculated K_{cir} is larger than the tested value. The reason for this is that the long conductor results in larger tested impedance. Therefore, for the same total current, the tested strand current will be smaller than the calculated value. Above all, the alignment between the calculated and tested result convincingly validates the accuracy of the proposed method.
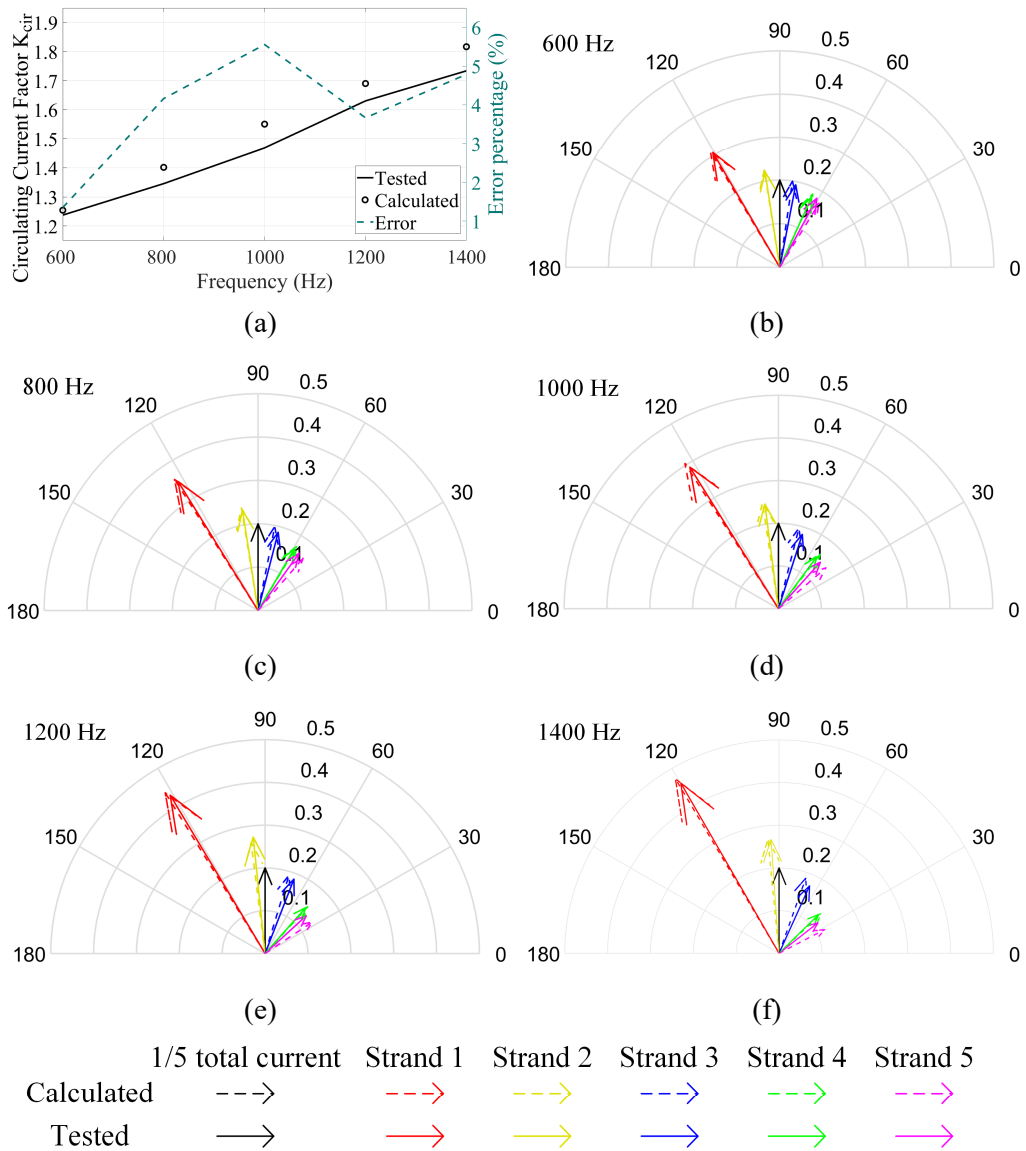
Figure 4.16. (a) Circulating current factors K_{cir} calculated by MEC and tested in experiment. Comparison of strand current calculated by MEC and tested in experiment at (b) 600 Hz, (c) 800 Hz, (d) 1000 Hz, (e) 1200 Hz, (f) 1400 Hz.

The strand current calculated by MEC and tested in experiment at different frequencies are shown in Figure 4.16 (b) to Figure 4.16 (f). The magnitude of the currents is normalized using the magnitude of the fundamental component of the total current as the benchmark. Setting the phase of the total current at 90 degrees, the phase of strand current can be determined accordingly. It is obvious that the difference in both magnitude and phase gets larger with the

101

increase of frequency, resulting in increasing K_{cir} as discussed above. Besides, the calculated strand current is in good agreement with experiment both in magnitude and phase, providing further evidence for the accuracy of the proposed method for strand current calculation.

4.5 Summary

A novel method based on MEC for circulating current loss calculation in electrical machines is proposed in this paper. Under the linear permeability assumption, the strand inductance and back EMF are calculated using mesh-based MEC and filled into the electric circuit equation, and subsequently the strand current is obtained by solving the electric circuit equation. The computational time of the proposed method is substantially shorter than the FEA without precision compromise.

It is proved to be efficient and precise for leakage inductance calculation based on conductor positions using MEC. Moreover, the proposed electric circuit involving the strands accurately represents the influence of the imbalance between the strands, providing a robust framework for circulating current analysis involving the harmonics.

The proposed method is applicable for diverse types of machines and various slot shapes. Although the circulating current is calculated based on the linear permeability assumption, the difference between RMS value of strand current by MEC and FEA model with nonlinear permeability is within acceptable margin. Besides, the saturation effect can be involved into the proposed method to improve the accuracy using methods such as frozen

permeability. Beyond the computational time for inductance and back EMF of each conductor, extra time is not required to calculate circulating current of different conductor connections. This efficiency enables rapid calculation of large number of windings in remarkably brief time. Consequently, the proposed method is highly suitable for winding optimization for circulating current loss reduction.

Chapter 5 Winding Optimization aiming at Reducing AC Copper Loss

In this chapter, a novel winding using rectangular bundles and rectangular conductors is proposed, specifically aiming at reducing AC copper loss in electrical machines. The winding optimization employs precise bundle transposition to minimize AC copper loss, given the difficulty of transposing each individual parallel strand. To demonstrate the winding optimization process, the copper loss on the baseline machine operating at a fundamental frequency of 1000 Hz is analyzed as an example. The optimization methodology integrates computational scope reduction and 2D FEA, revealing that increasing the number of parallel strands reduces the AC/DC copper loss ratio to approximately 1.03 at 1000 Hz, confirming the effectiveness of the transposition strategy in suppressing AC losses. Meanwhile, optimized winding also demonstrates significant potential for achieving high slot fill factor because the rectangular conductor can be compressed by improving manufacture technique. Experimental validation further proves the optimized winding's ability to suppress circulating current.

Due to the potential in both achieving high slot fill factor and minimized AC copper losses in electrical machines operating across a broad frequency spectrum (below 1400 Hz), the optimized winding shows promising application prospects in high-power-density electrical machines.

5.1 Problem Specification

5.1.1 Bundle Configuration

The purpose of this study is to develop a novel winding structure which can suppress the AC copper loss without significantly compromising the slot fill factor. The geometry of the baseline machine is shown in Figure 3.1 and specified in Table 3.1. The conductivity of the copper conductor is assumed to be constant, which means that the influence of temperature on conductivity is ignored.
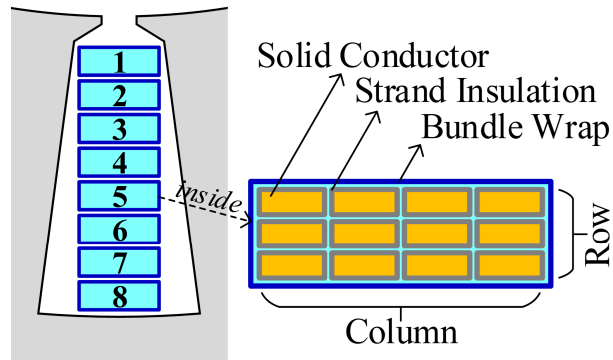
Figure 5.1. Bundle Schematic.

The structure of the bundle is shown in Figure 5.1 using a bundle with 12 strands as an example, and the number of strands in a bundle should be determined after optimization. There is no transposition for the strands within a bundle, and consequently the position of a strand in the bundle is fixed. The shape of the strand is determined to be rectangular because of the small gap between the conductors which is beneficial for the slot fill factor. The row and column number represents the number of rectangular conductors in tangential and radial direction in the bundle. There is a coat of insulation on the surface of the strands which insulates the strands in the same bundle. When the number of

strands in the bundle increases, the insulation coat will occupy more space in the slot and reduce the slot fill factor. The strands in a bundle are connected at the terminals of the winding, creating a parallel-connected circuit.

In the following discussion, the transposition of bundles is discussed instead of the transposition of each single strand. This is because it is very difficult to accomplish transposition by precisely placing each individual strand in the slot, and placing the bundle as an entity is much easier in contrast. Besides, the number of possible transposition schemes with bundles is much less than the strands and easier to discuss.

5.1.2 Bundle Transposition Table

To quickly describe large scale of complicated winding transposition schemes, a bundle placement table, Table 5.1, and an end-winding twist table, Table 5.2, are presented in the first place. In the following discussion, transposition is defined as the combination of placement and end-winding twist. Using these two tables, different winding transposition schemes can be discussed and compared easily.

Table 5.1 Bundle placement table.

Slot / Position	6	1	6	1	7	12	7	12	18	13	18	13	19	24	19	24
Bundle 1	►1	1	2	2	3	3	4	4	5	5	6	6	7	7	8	8
Bundle 2	7	7	8	8	►1	1	2	2	3	3	4	4	5	5	6	6
...	...															

Table 5.2 End-winding twist table.

Slot / Twist	6	1	6	1	7	12	7	12	18	13	18	13	19	24	19	24
Bundle 1	►+	-	-	+	+	-	-	+	+	-	-	+	+	-	-	+
Bundle 2	+	-	-	+	►+	-	-	+	+	-	-	+	+	-	-	+
…	…															

Firstly, the meaning of bundle placement table is illustrated. The bundle placement table is used to systematically describe the bundle placement, and an example is presented in Table 5.1 and Figure 5.2 to explain the correlation. The bundle placement of Table 5.1 is presented in Figure 5.2(a), and its connection circuit is presented in Figure 5.2(a) and Figure 5.2(b). As described in Figure 5.2(a), the precise bundle positions can be described using the slot number combined with pre-defined bundle position number. The pre-defined bundle positions are identical in all the slots, and they are numbered in order from the first bundle position near the slot opening to the last bundle position at the bottom of the slot. In addition, the number of bundle position in the slot is determined by slot number of the phase and number of turns. For the baseline machine, there are 8 slots in phase A, which means that the bundle can be placed in 8 different positions in the slot at maximum. Considering that there are 2 turns in this winding and 2 possible twisting angles which will be discussed later, 8 different bundle positions are placed in the slot area.

The placement of Bundle 1 and Bundle 2 different slots in Figure 5.2 (a) are transferred into the connection circuit in Figure 5.2(b). The placement, which is described using the slot number and position number in Figure 5.2 (a), is converted into an element in the connection circuit in Figure 5.2(b). The placements of a bundle in Figure 5.2(a) in different slots are converted into a branch in Figure 5.2(b). For example, in Figure 5.2(a), Bundle 1 is placed at Position 1 in Slot 6 in the beginning, and then placed at Position 1 in Slot 1, and then placed at Position 2 in Slot 6. Correspondingly, in Figure 5.2(b), the first

element in Bundle 1 branch is Position 1 Slot 6, followed with the second element of Position 1 Slot 1 and third element of Position 2 Slot 6. Using the same principle, the placements of Bundle 1 in Figure 5.2(a) can be transferred into Bundle 1 branch in Figure 5.2(b). Similarly, the placements of the other bundles can also be expressed as a branch in the connection circuit, and subsequently the placement of the winding can be described.

The connection circuit in Figure 5.2(b) can be further transferred into the placement table in Table 5.1 by extracting the slot and position to heading. The start insert of the bundle is noted with a black triangle, and the sequence in the connection circuit is in order from left to right in the table. Each branch in Figure 5.2(b) represents a different row in the table. The values in the table represents the position number in the slot, while the slot number in its column represents the slot it is in. For example, Bundle 1 branch in connection circuit in Figure 5.2(b) is transferred into the row named "Bundle 1" in Table 5.1.
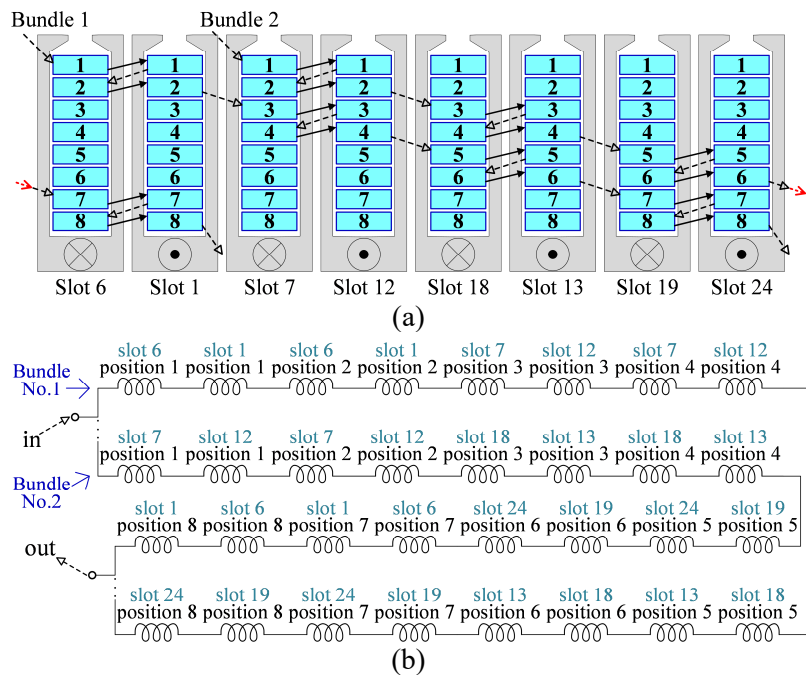
Figure 5.2. Transposition of Bundle No.1 in phase A. (a) Schematic figure. (b) Connection circuit.

108

Secondly, the meaning of end-winding twist table is illustrated taking Table 5.2 as an example. An example of a bundle with 12 strands is presented in Figure 5.3 to illustrate the difference in bundle twist angle. The strands in the bundle are noted with different number, and the positions of these strands after 0° and 180° bundle twist are shown in Figure 5.3 (a) and Figure 5.3 (b). It can be observed that the strand position in the bundle remains the same, but the strand position in the slot can be different with different twist angle of end-winding.
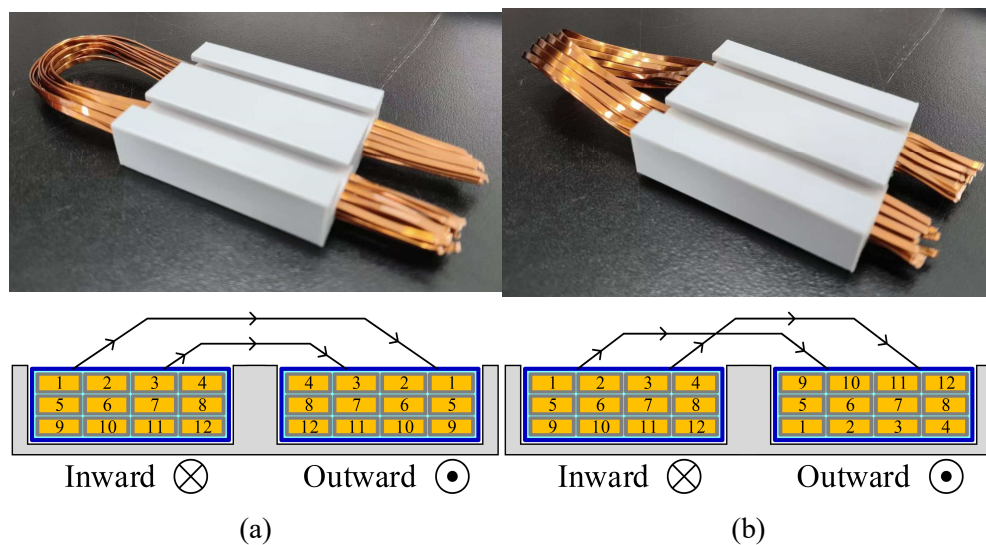
Figure 5.3 Illustration model and schematic figure of bundle twist of (a) 0° twist angle and (b) 180° twist angle.

To describe the twist angle of end-winding between the slots, end-winding twist table is presented in Table 5.2. The twist angle at the end-winding is derived by comparing 2 adjacent elements of a bundle. If the 2 adjacent elements in a row are the same, the twist angle is 0°; if the 2 adjacent elements in a row are not the same, the twist angle is 180°. For example, the first 3 elements in the row of "Bundle 1" are "➤+", "-" and "-". It represents that the Bundle No.1 is inserted in Slot No.6 in the beginning, then the bundle is twisted for 180° and inserted into Slot No.1, and then twisted for 0° and inserted into Slot No.6.

The bundle placement table and end-winding twist table can be integrated into a transposition table, in which each element contains a number and a symbol. For example, the first 3 elements in the first row in the table integrated from Table 5.1 and Table 5.2 is "▸1+", "1-" and "2+".

Using the total number of strands (row×column) and bundle transposition table, different transposition schemes can be described. Each different combination of strand number and transposition table has a corresponding winding structure and copper loss at rated working condition. Subsequently, the purpose of the study is converted to find out the combination with the minimum copper loss at rated working condition.

5.2 Winding Optimization Design

5.2.1 Narrow the Calculation Scope

The total number of all the possible bundle placements is numerous, and it is impossible to calculate the copper loss of all the different schemes, even with analytical methods. Therefore, instead of calculating the copper loss of all the possible transposition schemes, principles are proposed to narrow the scope of calculation.
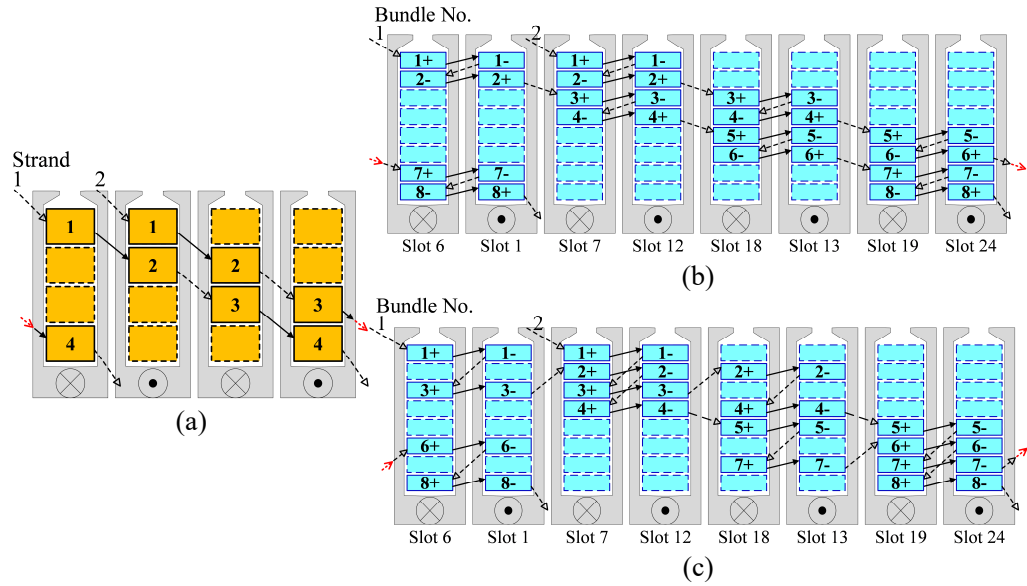
Figure 5.4 (a) Hairpin winding transposition. (b) One bundle transposition scheme of bundle resembling hairpin winding. (c) Another bundle transposition scheme.

Firstly, the placement pattern between the slots of a bundle can be determined to narrow the scale of different bundle placements. It is already known that circulating current is caused by imbalanced leakage inductances between the strands, and the difference in leakage inductance is caused by different strand positions in the slot. Therefore, to minimize the circulating current, a bundle should be placed at as many different slot positions as possible, similar to the transposition used in hairpin winding [116] as shown in Figure 5.4(a). The difference between the hairpin winding and the bundle is that it is not necessary to consider the twist angle for the hairpin winding because it is solid, but for the bundle the twist angle is essential because of the strands inside as illustrated in Figure 5.3 . Therefore, for the transposition of the bundle, it should be placed at each different position twice, once for "+" and once for "-" in Table 5.2. Two different transposition schemes following the pattern are shown in Figure 5.3   (b) and Figure 5.3 (c). Therefore, once the position and twist angle

in the initial slot of a bundle is determined, transposition of this bundle in the rest of the slots can be determined accordingly.

Secondly, all the bundles should be transposed in the same pattern, meaning that the bundles should be symmetrical to each other. The reason for this is to minimize the circulating current between different bundles. For example, the transposition of Bundle 2 in Figure 5.4(b) follows the same pattern with Bundle 1, and the only difference is the position in the initial slot. Therefore, once the transposition of the first bundle is determined, the transposition of rest of the bundles can be determined by translating the first bundle to the other slots.

Thirdly, eliminate the twist angles which are virtually repeated. For example, in the transposition scheme illustrated in Figure 5.4(b), Bundle 1 is placed at "1+" and "2-" in Slot 1. It is completely identical with the case where Bundle 1 is placed at "1-" and "2+" in Slot 1. Taking the bundle with 12 strands in Figure 5.5 as an example, it can be observed that the only difference between these 2 cases is the serial number of the strand. Similarly, the "1+" plus "2+" in Slot 6 is identical with "1-" plus "2-" in this slot. Therefore, in this case, only "+" plus "+" and "+" plus "-" are discussed.
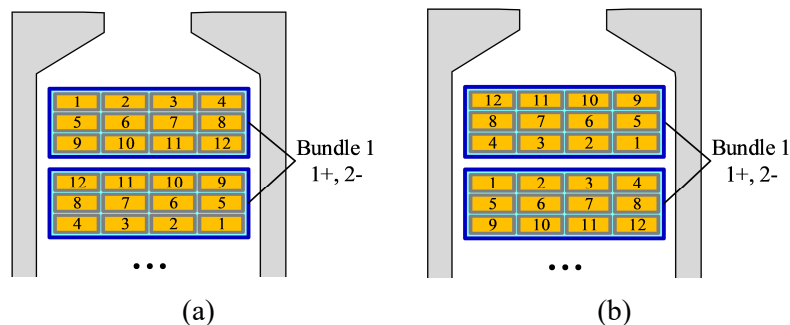
Figure 5.5 Strand distribution of (a)"1+" plus "2-" and (b) "1-" plus "2+" with 12 strands in a bundle.

After the discussions on narrowing the calculation scope, most of the

transposition schemes are eliminated. Different schemes of the placement and

twist angle in the initial slot of the first bundle which follow the aforementioned

principles are illustrated in Figure 5.6.
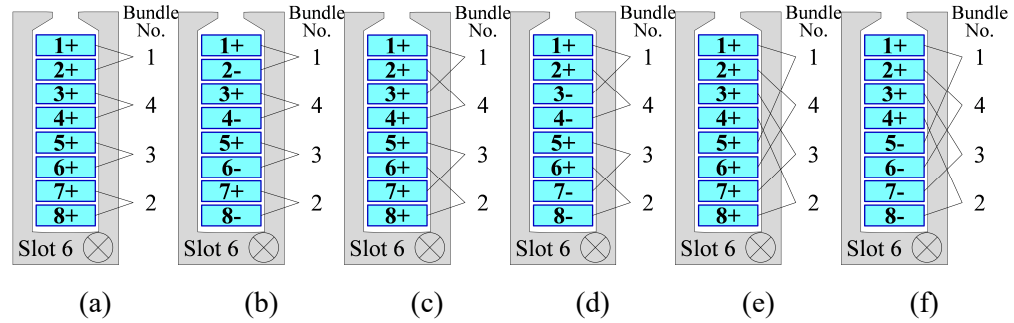
Figure 5.6 Placement and twist angle in the Slot 6 of transposition scheme (a) 1, (b) 2, (c) 3, (d) 4, (e) 5, (f) 6.

5.2.2 Bundle Transposition

The final optimized winding configuration consists of two parts: bundle

transposition and strand number in a bundle. Calculating all the combinations of

bundle transpositions and strand numbers using FEA is excessively time-

consuming. Therefore, to streamline this process, the bundle transposition is

determined in the first step by comparing the circulating current loss in various

schemes using an analytical method. This approach effectively reduces

computational time by initially narrowing down the range of winding cases, and

subsequently FEA is employed for precise calculations of the winding cases

within this narrowed scope.

To evaluate the circulating current loss of various bundle transposition

schemes, the circulating current factor K_{cir} is introduced. This factor is defined

as the ratio of copper loss due to unevenly distributed strand current to DC

copper loss:

$$K_{cir}=P_{cir}/P_{DC}=\frac{(I_{A1}{}^2+I_{A2}{}^2+...+I_{Am}{}^2)}{m\times(I_A/m)^2}$$ (5.1)

where m denotes the number of strands. Apparently, when there is no circulating current between the strands (i.e. currents in all strands are identical), K_{cir} equals 1. Consequently, a K_{cir} close to 1 indicates more effective suppression of circulating currents, and (K_{cir} -1) can be regarded as the ratio of additional circulating current loss to DC copper loss.

The method of comparing K_{cir} values among different bundle transposition schemes is illustrated in Figure 5.7. For each bundle transposition scheme, the K_{cir} for varying number of strands (3×4 to 10×10) are calculated and organized into a matrix, as illustrated in the dashed box in Figure 5.7(a). This process is repeated to generate and compare K_{cir} matrices for the bundle transposition schemes illustrated in Figure 5.6. It is worth mentioning that the bundle transposition schemes with very few strand numbers are not calculated due to the significant skin effect and proximity loss in those cases which cannot be precisely calculated using the analytical method. Besides, the iron core saturation is not considered in this analytical model.
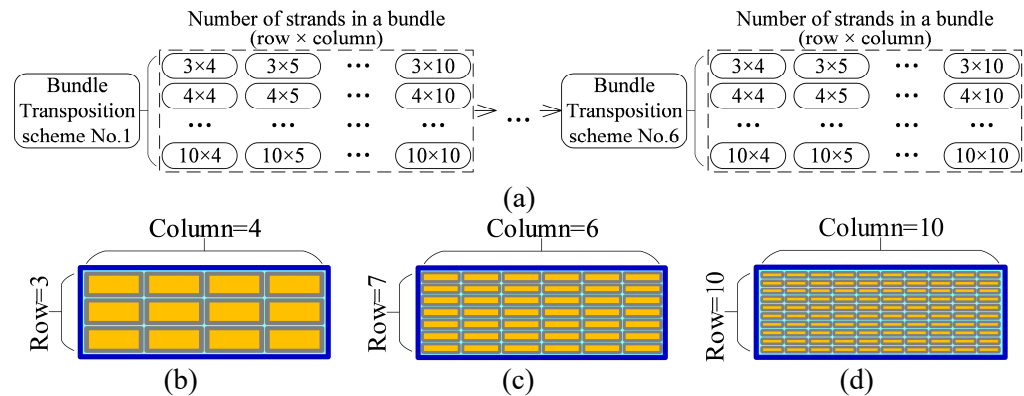
Figure 5.7 (a) Calculation and comparison of different bundle transposition schemes. (b) Row 3 column 4, 12 strands in a bundle. (b) Row 7 column 6, 24 strands in a bundle. (c) Row 10 column 10, 100 strands in a bundle.

The K_{cir} matrix of the bundle transposition schemes in Figure 5.6 is demonstrated in Figure 5.8. The K_{cir} matrix of all the transposition schemes in Figure 5.6 are completely identical, indicating that each bundle transposition scheme possesses an equivalent ability to suppress circulating current. The reason for the same performance of reducing circulating current loss is the identical strand inductances. Strand inductance is primarily determined by its position in the slot. In each transposition configuration, the bundles follow an identical pattern that occupies all available slot positions, meaning that a bundle occupies all different slot positions in different the transposition schemes. Consequently, this uniformity in slot position ensures equivalent strand inductances and, by extension, identical suppression of circulating current loss in all 6 transposition schemes. Furthermore, it is evident that the optimized bundle transposition schemes are highly effective in minimizing circulating current loss. The maximum K_{cir} recorded is 1.029, while its minimum is 1.010, suggesting that the circulating current loss in those windings is reduced to almost negligible with these bundle transposition schemes. In general, it can be concluded that all the transposition schemes in Figure 5.6 demonstrate robust capability in suppressing circulating current loss, regardless of the number of strands.
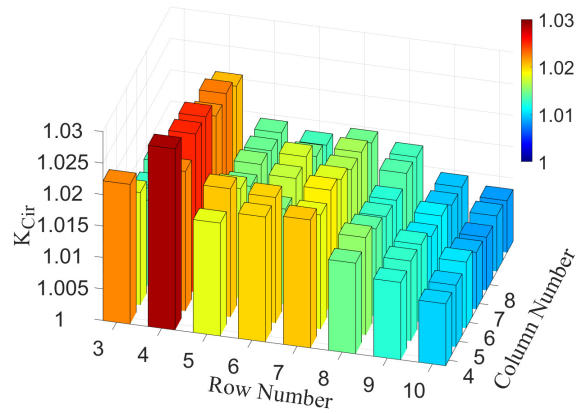
Figure 5.8 Circulating current factor of the proposed bundle transposition schemes with different strand numbers calculated by analytical method.

Considering the intersect and bending of end-winding, transposition scheme No.2 in Figure 5.6(b) is selected for further discussion. The complete description of this scheme is illustrated in Table 5.3, a combination of bundle placement table and end-winding twist table.

Table 5.3 Optimized bundle transposition.

Slot / Transp.	6	1	6	1	7	12	7	12	18	13	18	13	19	24	19	24
Bundle 1	►1+	1-	2-	2+	3+	3-	4-	4+	5+	5-	6-	6+	7+	7-	8-	8+
Bundle 2	7+	7-	8-	8+	►1+	1-	2-	2+	3+	3-	4-	4+	5+	5-	6-	6+
Bundle 3	5+	5-	6-	6+	7+	7-	8-	8+	►1+	1-	2-	2+	3+	3-	4-	4+
Bundle 4	3+	3-	4-	4+	5+	5-	6-	6+	7+	7-	8-	8+	►1+	1-	2-	2+

5.2.3 Strand Number

FEA simulations are performed to precisely calculate the copper loss of the bundle transposition scheme described in Table 5.3 across a range of strand numbers. These FEA simulations incorporate skin effect and proximity loss, which are not addressed in the analytical method. The simulations cover the bundle with the strand number ranging from 3×2 to 10×10. The gap between the strands within a bundle is set at 0.15mm, and the gap between the bundles is set at 0.3mm. To reduce the computational time, the strands in Phase A are modeled

as solid conductors, whereas windings in Phase B and C are simulated as stranded winding.

(a)   (b)
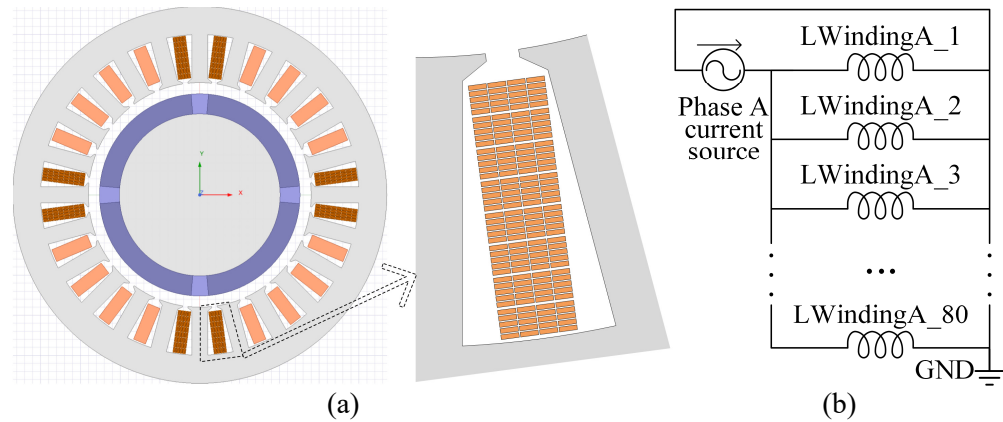
Figure 5.9 (a) FEA model and (b) External circuit of the baseline machine with 5×4 strands in a bundle.

As an example, the FEA model of 20 strands (5×4) in a bundle and its external circuit are shown in Figure 5.9(a) and Figure 5.9(b). There are 20 strands in a bundle and 4 bundles connected in parallel in this case, resulting in 80 parallel strands in total in the external circuit.

The AC loss factor K_{AC} and copper loss in phase A calculated by FEA with different strand number in a bundle are depicted in Figure 5.10(a) and Figure 5.10(b). The AC copper loss factor K_{AC}, defined as the ratio of copper loss to DC copper loss, serves as a metric to evaluate the effectiveness in suppressing AC copper loss. As shown in Figure 5.10(a), K_{AC} peaks at 3 when the strand number is 3×2 and then decreases rapidly as the strand number increases, eventually stabilizing at around 1.03. This trend suggests that as the number of strands increases, the winding transposition scheme becomes more effective at suppressing AC copper loss.

In contrast, the trend in copper loss for phase A, as observed in Figure 5.10(b), does not mirror the K_{AC} trend. With the strand number increasing, the

117

copper loss in phase A dramatically decreases from its peak of 280 W when the strand number is 3×2, to about 150 W when the strand number reaches 7×6, followed by a slight increase after that. For strand numbers within the range of 6×4 to 7×7, the copper losses are relatively constant, ranging between 149.7 W and 153.2 W.

The comparison between Figure 5.10(a) and Figure 5.10(b) reveals that although the suppression of AC copper loss improves with increasing strand numbers, there is a simultaneous increase in DC copper loss. Therefore, the selection of the strand number should be made with careful consideration on the trade-off between managing AC and DC copper loss.
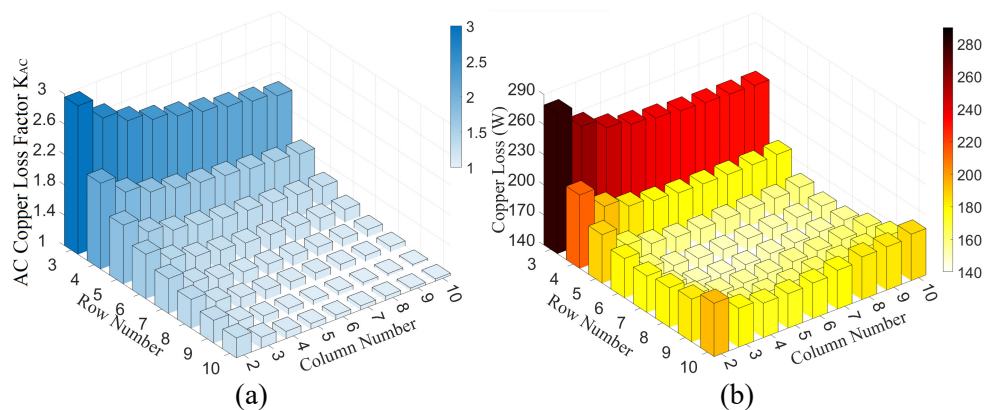
Figure 5.10 (a) AC copper loss factor and (b) Copper loss in phase A with different strand number calculated by FEA.

Considering complexities in implementation associated with the increasing strand number, the strand number of 6×5 is selected for the bundle transposition scheme. The copper loss of this winding is 150.8W while its AC copper loss factor is 1.26. The slot fill factor achieved is 0.4, based on strand and bundle gaps of 0.15 mm and 0.3 mm. It should be noted that this fill factor could potentially be enhanced with advancements in manufacturing techniques that allow for smaller gaps.

To further illustrate the relation between the AC copper loss and strand number, the AC copper loss factor K_{AC} and copper loss of different strand number for the bundle transposition scheme in Table 5.3 at varying frequencies are presented in Figure 5.11. It can be observed in Figure 5.11(a) that the K_{AC} increases as the frequency of input current increases across all the strand numbers, but the increase rate diminishes dramatically as the strand number grows. This pattern suggests that the AC copper loss in the baseline machine at higher frequencies can be effectively mitigated by employing the bundle transposition scheme with a larger strand number.

Meanwhile, as shown in Figure 5.11(b), an increase in DC copper loss correlated with higher strand numbers is an unavoidable trade-off. It is obvious that the reduction in AC copper loss comes at the expense of increased DC copper loss. Therefore, for electrical machines operating at high frequencies, a larger number of strands is advantageous for reducing AC copper loss, while a smaller number of strands is desirable for machines operating at lower frequencies.

(a)   (b)
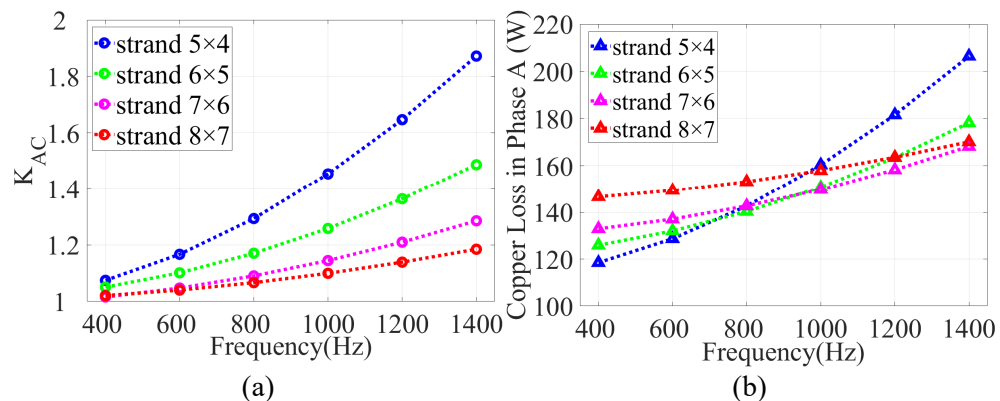
Figure 5.11 (a) Ratio of total copper loss to DC copper loss and (b) copper loss in phase A at different frequencies for different strand numbers.

5.2.3 Comparison with Random-Wound Winding

To further illustrate the effect of the bundle transposition, FEA model of a random-wound winding in the same baseline machine is simulated as shown in Figure 5.12. The slot fill factor of the random-wound winding is set at 0.4, identical to the optimized winding with strand number of 6×5. To save the computational time, Phase B and Phase C windings in the FEA model are set as stranded winding, ignoring their AC copper losses. The conductor noted with the same number are connected in series, and the conductor configuration of all slots in Phase A is identical.

The copper loss of the random-wound winding in Phase A at 1000 Hz is 1.67 kW, much larger than that of the optimized winding at 150.8 W. Such comparison effectively proves the suppression ability of the bundle transposition.
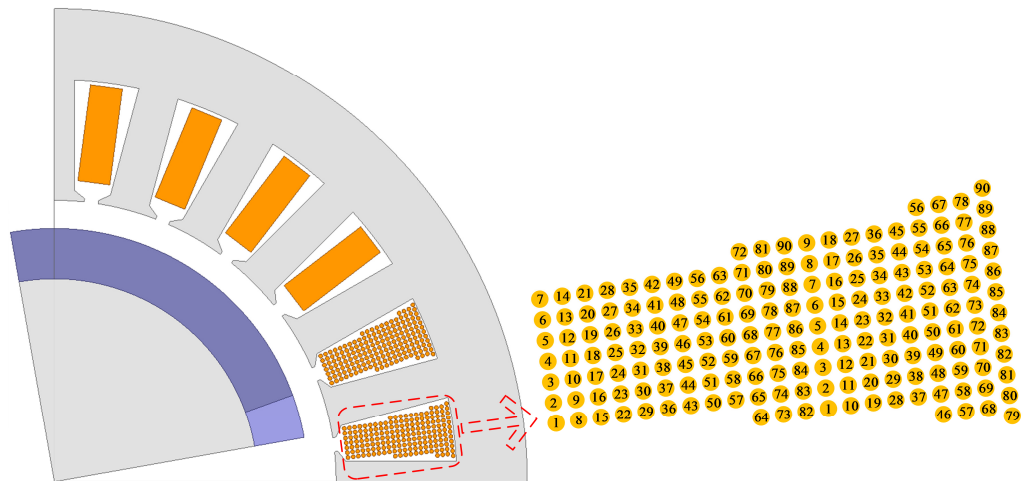
Figure 5.12 FEA model and winding configuration of the random-wound winding.

5.3 Experimental Validation

5.3.1 Experimental Setup

An experiment is conducted to validate the suppression ability of the optimized winding on circulating current.

The structure of Motorette #3 and the details of the winding is shown in Figure 5.13, and its schematic is shown in Figure 5.14. It is worth mentioning that the permanent magnet of the baseline machine is not implemented on the Motorette #3 because it does not influence the current distribution in each strand. Besides, the winding is implemented the same with Bundle No.1 described in Table 5.3, and the strand number is 5×4. This is because all the 4 bundles are completely identical and there is no circulating current between the bundles, and it is easier to implement the bundle with less strand number. In addition, 3D-printed plastic pieces are filled in the slot to fix the bundle at certain positions, and they are also used to keep the rotor core at center position.

(a)   (b)   (c)
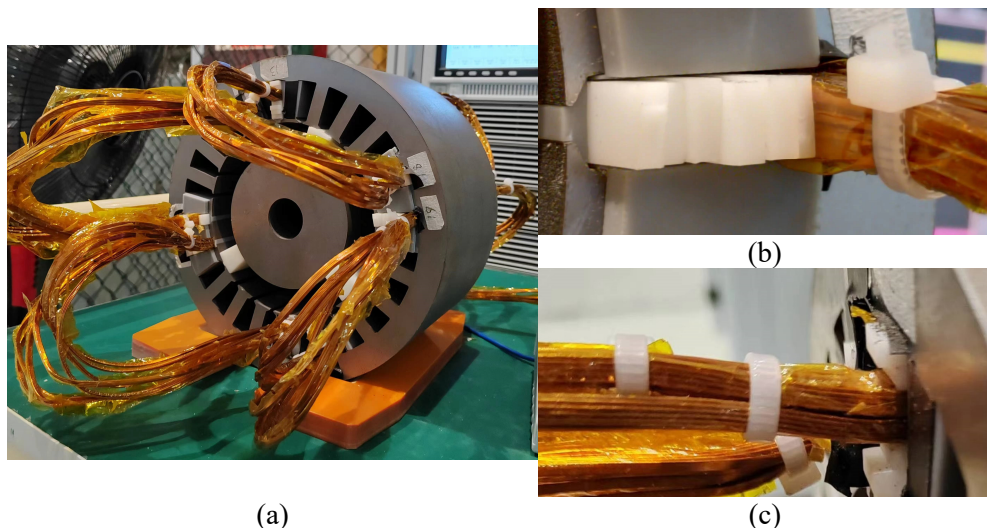
Figure 5.13 (a) Overview of the Motorette #3. (b) Top view of the slot. (c) Side view of the slot.
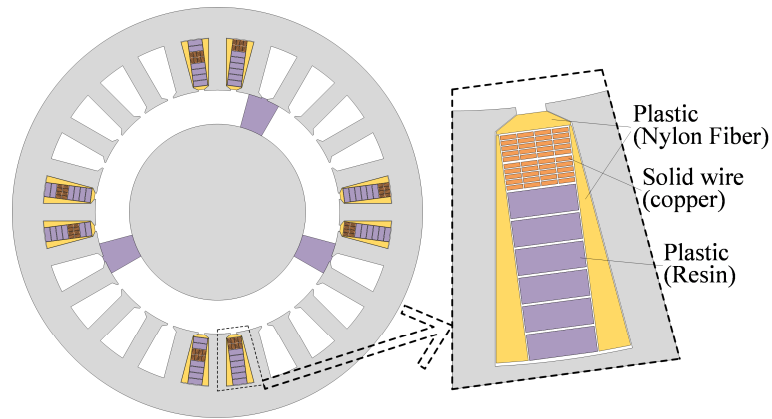
Figure 5.14 Structure drawing of the Motorette #3.

The experimental setup and its electrical circuit are shown in Figure 5.15. The current probes and voltage differential probes are connected to the oscilloscope to collect instantaneous data. Due to the limited number of channels of the oscilloscope, the strand current is measured separately. During the test, there is always one channel measuring the terminal voltage of the bundle and a channel measuring the total current and the rest of 2 channels are used to measure the current in each strand in turn. The measured voltage and total current are used as the reference of magnitude and phase of the strand current.

(a)   (b)
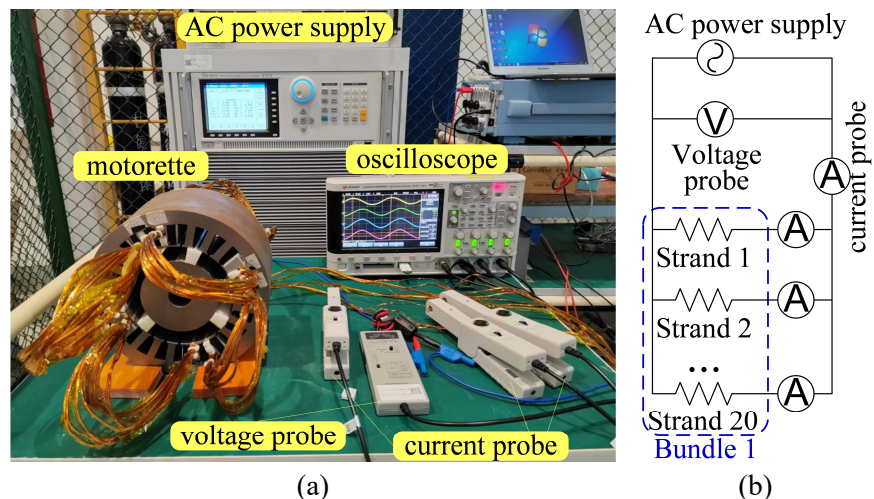
Figure 5.15 (a) Test bench and (b) electrical circuit of the experimental setup.

5.3.2 Results and Discussion

The normalized magnitude of the tested current in each strand at different

frequencies is shown in Figure 5.16. It can be observed that as the frequency increases, the tested strand currents become less evenly distributed. At 400 Hz, the maximum and minimum normalized strand current are 1.05 and 0.97 respectively, and as frequency grows to 1400 Hz these values change to 1.14 and 0.89. Furthermore, the tested circulating current factor K_{cir} at various frequencies is shown in Figure 5.17. It can be observed that the maximum K_{cir} reaches 1.04 at 1400 Hz, indicating that the circulating current loss is reduced effectively at all tested frequencies. Above all, the experiment validates the aforementioned effectiveness of the winding on suppressing circulating current at various frequencies.
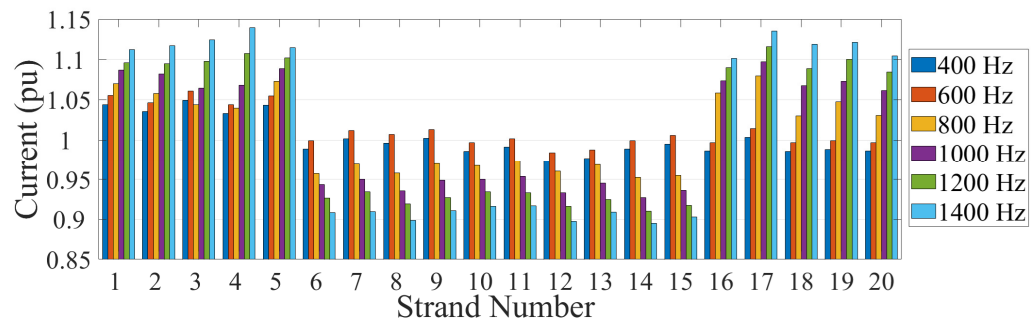
Figure 5.16 Magnitude of tested strand current taking the 1/20 of the input current as normalization unit.
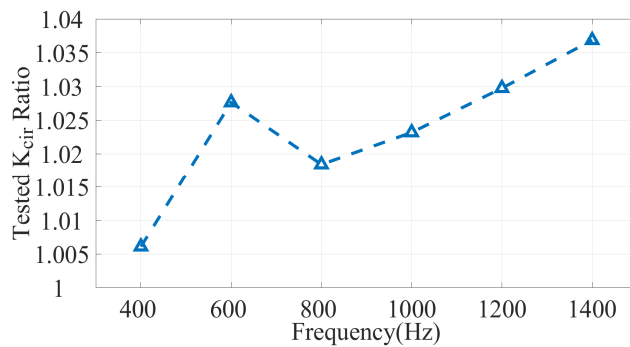
Figure 5.17 Tested K_{cir} ratio of the winding at different frequencies.

5.3 Summary

A novel winding using rectangular bundle transposition aiming at reducing

AC copper loss in electrical machines is proposed in this paper. The process of winding optimization is illustrated in detail using the baseline machine as an example, demonstrating the strong capability of the winding to suppress AC copper loss.

The circulating current factor K_{cir} of the optimized bundle transposition schemes, calculated by analytical method, shows significant effectiveness in suppressing circulating current at 1000 Hz in the baseline machine, regardless of strand number. Moreover, the ability of the optimized bundle transposition to suppress AC copper loss increases with the number of strands in the bundle across various frequencies. However, a higher strand number also results in a lower slot fill factor due to the gaps between the strands and the bundles, highlighting a crucial trade-off between AC and DC copper loss that must be carefully managed during the optimization process.

Overall, the optimized bundle transpositions exhibit strong capabilities in suppressing AC copper loss in electrical machines, which can be further enhanced by increasing strand number in the bundle. Thus, the winding composed of rectangular bundles are highly promising for use in electrical machines operating at high frequencies, especially if advancements are made in manufacturing techniques to reduce the gaps between the strands and bundles.

Chapter 6 Conclusion and Future Work

6.1 Conclusion

This study is driven by emerging needs of enhancing the power density of electrical machines. Given the limitations of aircraft load and space capacities, it is crucial to reduce AC copper loss in electrical machines. However, the winding options available for achieving low AC copper loss are limited, particularly at frequencies below 1400 Hz. Therefore, this research aimed to develop a winding configuration that minimizes AC copper loss without significantly compromising the slot fill factor and finally achieve higher power density.

To achieve the objective of winding optimization design targeting low AC copper loss, a rapid proximity calculation method and a rapid circulating current calculation method have been developed. In Chapter 3, a mesh-based MEC method capable of fast and accurate estimation of proximity and flux leakage in electrical machines have been proposed. This approach demonstrates high computational efficiency while maintaining accuracy comparable to 2D FEA under linear permeability assumptions. Chapter 4 extends the method to enable rapid circulating current calculation, providing a practical solution for winding optimization involving AC copper loss calculation on large scale of various winding structures, significantly reducing computational time compared to FEA. These methodologies have potential applications across a variety of machine types, particularly for those operating within frequency below 1400 Hz.

In Chapter 5, a winding optimization method has been explored aiming at

reducing AC copper loss. A systematic winding transposition table has been introduced to describe different winding transpositions, effectively narrowing the calculation scope and shortening computational time, proving the necessity of the winding transposition table. Notably, the bundle transpositions following the same pattern to transpose to as many slot positions as possible have shown equivalent ability to suppress the circulating current loss. Moreover, the bundle transposition has exhibited strong capabilities on suppressing AC copper loss at various frequencies. The effectiveness in reducing AC copper loss increased with the number of strands, with the AC copper loss decreasing to as low as 3% of the DC copper loss at 1000 Hz in the baseline machine according to 2D FEA result. With optimized winding, AC copper loss can be effectively reduced, which is beneficial for the thermal management system of the electrical machines, thus enhancing their overall power density, benefiting the development of more electric aircraft.

6.2 Future Work

Firstly, the proposed method can be further improved by incorporating the saturation effect. The primary limitation of the proposed analytical methods is the assumption of linear permeability of the iron core, which excludes consideration of saturation effects. This problem can be involved by incorporating proper methods, such as frozen permeability method and segmental linearizing of permeability. In addition, this limitation can be addressed by integrating Finite Element Analysis (FEA) simulations to complement the analytical methods in the optimization process, allowing for

more precise copper loss calculations in various winding configurations, at the cost of an acceptable increase in computational time.

Secondly, further research should also focus on integrating the proposed winding into the electrical machine design process. Manufacture techniques such as minimizing the gap between strands and bundles should be explored to reduce DC copper loss, especially when large strand numbers are employed. Additionally, designing an appropriate thermal management system for the novel rectangular bundle winding could be essential. If necessary, comprehensive design including both winding and thermal management systems are recommended. Furthermore, the application of these winding in various types of machines should be investigated, other than the type of baseline machine, permanent magnet synchronous machines with full pitch winding.

References

[1] D. L. Greene, H. H. Baker Jr, and S. E. Plotkin, "Reducing greenhouse gas emissions from US transportation," 2010.

[2] D. S. Lee *et al.*, "The contribution of global aviation to anthropogenic climate forcing for 2000 to 2018," *Atmos Environ*, vol. 244, p. 117834, Jan. 2021, doi: 10.1016/j.atmosenv.2020.117834.

[3] H. Sasa *et al.*, "Electromagnetic-thermal coupled analysis considering AC losses in REBCO windings of 10 MW fully superconducting synchronous generators cooled by subcooled liquid nitrogen for electric aircraft," *IEEE Transactions on Applied Superconductivity*, vol. 32, no. 6, pp. 1–6, 2022.

[4] S. A. S. Airbus, "Global Market Forecast, Global Networks, Global Citizens 2018-2037," 2018, *AirBus Blagnac Cedex*.

[5] J. K. Noland, M. Leandro, J. A. Suul, and M. Molinas, "High-Power Machines and Starter-Generator Topologies for More Electric Aircraft: A Technology Outlook," *IEEE Access*, vol. 8, pp. 130104–130123, 2020, doi: 10.1109/ACCESS.2020.3007791.

[6] S. Bozhko *et al.*, "Development of aircraft electric starter–generator system based on active rectification technology," *IEEE Transactions on Transportation Electrification*, vol. 4, no. 4, pp. 985–996, 2018.

[7] M. Hirst, A. McLoughlin, P. J. Norman, and S. J. Galloway, "Demonstrating the more electric engine: A step towards the power optimised aircraft," *IET Electr Power Appl*, vol. 5, no. 1, pp. 3–13, Jan. 2011, doi: 10.1049/iet-epa.2009.0285.

[8] W. Cao, B. C. Mecrow, G. J. Atkinson, J. W. Bennett, and D. J. Atkinson, "Overview of electric motor technologies used for more electric aircraft (MEA)," *IEEE Transactions on Industrial Electronics*, vol. 59, no. 9, pp. 3523–3531, 2012, doi: 10.1109/TIE.2011.2165453.

[9] X. Roboam, B. Sareni, and A. De Andrade, "More electricity in the air: Toward optimized electrical networks embedded in more-electrical aircraft," *IEEE industrial electronics magazine*, vol. 6, no. 4, pp. 6–17, 2012.

[10] M. Sinnett, "787 no-bleed systems: saving fuel and enhancing operational efficiencies," *Aero Quarterly*, vol. 18, pp. 6–11, 2007.

[11] J. Jiang *et al.*, "A review on insulation challenges towards electrification of aircraft," Apr. 01, 2023, *John Wiley and Sons Inc*. doi: 10.1049/hve2.12304.

[12] L. Setlak, "Review, Analysis and Simulation of Advanced Technology Solutions of Selected Components in Power Electronics Systems (PES) of More Electric Aircraft," 2015. [Online]. Available: https://www.researchgate.net/publication/289533146

[13] W. R. Canders, J. Ho, and M. Henke, "Cooling technologies for high power density electrical machines for aviation applications," *Energies (Basel)*, vol. 12, no. 23, Dec. 2019, doi: 10.3390/en12234579.

[14] K. S. Haran *et al.*, "High power density superconducting rotating machines—development status and technology roadmap," *Supercond Sci Technol*, vol. 30, no. 12, p. 123002, Dec. 2017, doi: 10.1088/1361-6668/aa833e.

[15]   N. A. of Sciences *et al.*, *Commercial aircraft propulsion and energy systems research: reducing global carbon emissions*. National Academies Press, 2016.

[16]   X. Zhang, C. L. Bowman, T. C. O'Connell, and K. S. Haran, "Large electric machines for aircraft electric propulsion," *IET Electr Power Appl*, vol. 12, no. 6, pp. 767–779, Jul. 2018, doi: 10.1049/iet-epa.2017.0639.

[17]   F. Edition and S. J. Chapman, "Electric machinery fundamentals," 2012.

[18]   M. Liu, Y. Li, H. Ding, and B. Sarlioglu, "Thermal management and cooling of windings in electrical machines for electric vehicle and traction application," in *2017 IEEE Transportation Electrification Conference and Expo (ITEC)*, 2017, pp. 668–673. doi: 10.1109/ITEC.2017.7993349.

[19]   G. Du, W. Ye, Y. Zhang, L. Wang, T. Pu, and N. Huang, "Comprehensive Analysis of the AC Copper Loss for High Speed PM Machine With Form-Wound Windings," *IEEE Access*, vol. 10, pp. 9036–9047, 2022, doi: 10.1109/ACCESS.2022.3143817.

[20]   G. Du, W. Ye, Y. Zhang, L. Wang, and T. Pu, "Comprehensive Analysis of Influencing Factors of AC Copper Loss for High-Speed Permanent Magnet Machine with Round Copper Wire Windings," *Machines*, vol. 10, no. 9, Sep. 2022, doi: 10.3390/machines10090731.

[21]   E. Sayed *et al.*, "Review of Electric Machines in More-/Hybrid-/Turbo-Electric Aircraft," Dec. 01, 2021, *Institute of Electrical and Electronics Engineers Inc.* doi: 10.1109/TTE.2021.3089605.

[22]   T. Dong, X. Zhang, F. Zhou, and B. Zhao, "Correction of Winding Peak Temperature Detection in High-Frequency Automotive Electric Machines," *IEEE Transactions on Industrial Electronics*, vol. 67, no. 7, pp. 5615–5625, Jul. 2020, doi: 10.1109/TIE.2019.2931513.

[23]   X. Chen, H. Fang, X. Fan, H. Hu, D. Li, and R. Qu, "Suppression of winding AC copper loss in high-speed electrical machines by a practical transposition technique," *IEEE Trans Ind Appl*, vol. 58, no. 6, pp. 7121–7130, 2022.

[24]   B. S. Guru and H. R. Hiziroglu, *Electromagnetic Field Theory Fundamentals*. 2004. doi: 10.1017/cbo9781139165297.

[25]   A. Bardalai, "Winding AC loss reduction techniques in the slot of high-frequency electrical machines," 2019. [Online]. Available: http://eprints.nottingham.ac.uk/57246/

[26]   P. N. Murgatroyd, "Calculation of proximity losses in multistranded conductor bunches," *IEE Proceedings A (Physical Science, Measurement and Instrumentation, Management and Education)*, vol. 136, no. 3, pp. 115–120, May 1989, doi: 10.1049/ip-a-2.1989.0021.

[27]   O. Gassab *et al.*, "Fast and Accurate Semi-Analytical Solution to Skin and Proximity Effects in Shielded Cable Systems," *IEEE Trans Electromagn Compat*, vol. 65, no. 6, pp. 1632–1646, Dec. 2023, doi: 10.1109/TEMC.2023.3298809.

[28]   P. H. Mellor, R. Wrobel, and N. McNeill, "Investigation of proximity losses in a high speed brushless permanent magnet motor," in *Conference Record - IAS Annual Meeting (IEEE Industry Applications Society)*, 2006, pp. 1514–1518. doi: 10.1109/IAS.2006.256730.

[29]   C. R. Sullivan, "Winding loss calculation with multiple windings, arbitrary waveforms, and two-dimensional field geometry," in *Conference Record of the 1999 IEEE Industry Applications Conference. Thirty-Forth IAS Annual Meeting (Cat. No.99CH36370)*, IEEE, 1999, pp. 2093–2099. doi: 10.1109/IAS.1999.806024.

[30]   J. Pyrhönen, T. Jokinen, and V. Hrabovcová, *Design of Rotating Electrical Machines*. Wiley, 2013. doi: 10.1002/9781118701591.

[31]   P. Mellor, R. Wrobel, and N. Simpson, "AC losses in high frequency electrical machine windings formed from large section conductors," in *2014 IEEE Energy Conversion Congress and Exposition, ECCE 2014*, Institute of Electrical and Electronics Engineers Inc., Nov. 2014, pp. 5563–5570. doi: 10.1109/ECCE.2014.6954163.

[32]   M. Ibrahim and P. Pillay, "A hybrid model for improved hysteresis loss prediction in electrical machines," in *2013 IEEE Energy Conversion Congress and Exposition*, 2013, pp. 4348–4355. doi: 10.1109/ECCE.2013.6647282.

[33]   W. L. Soong, "Bh curve and iron loss measurements for magnetic materials".

[34]   S. Xue, J. Feng, S. Guo, J. Peng, W. Q. Chu, and Z. Q. Zhu, "A New Iron Loss Model for Temperature Dependencies of Hysteresis and Eddy Current Losses in Electrical Machines," *IEEE Trans Magn*, vol. 54, no. 1, pp. 1–10, 2018, doi: 10.1109/TMAG.2017.2755593.

[35]   M. Kazimierczuk, *High-Frequency Magnetic Components*. Wiley, 2013. doi: 10.1002/9781118717806.

[36]   A. Bermudez, D. Gomez, and P. Salgado, "Eddy-Current Losses in Laminated Cores and the Computation of an Equivalent Conductivity," *IEEE Trans Magn*, vol. 44, no. 12, pp. 4730–4738, 2008, doi: 10.1109/TMAG.2008.2005118.

[37]   Z. Q. Zhu *et al.*, "Evaluation of Iron Loss Models in Electrical Machines," *IEEE Trans Ind Appl*, vol. 55, no. 2, pp. 1461–1472, Mar. 2019, doi: 10.1109/TIA.2018.2880674.

[38]   R. Wrobel, G. Vainel, C. Copeland, T. Duda, D. Staton, and P. Mellor, "Investigation of mechanical loss and heat transfer in an axial-flux PM machine," in *2013 IEEE Energy Conversion Congress and Exposition*, 2013, pp. 4372–4379. doi: 10.1109/ECCE.2013.6647285.

[39]   T. A. Harris and M. N. Kotzalas, *Advanced Concepts of Bearing Technology*. CRC Press, 2006. doi: 10.1201/9781420006582.

[40]   R. Wrobel, G. Vainel, C. Copeland, T. Duda, D. Staton, and P. H. Mellor, "Investigation of mechanical loss components and heat transfer in an axial-flux PM machine," *IEEE Trans Ind Appl*, vol. 51, no. 4, pp. 3000–3011, 2015.

[41]   J. E. Vrancik, "Prediction of windage power loss in alternators," 1968.

[42]   D. A. Howey, A. S. Holmes, and K. R. Pullen, "Measurement and CFD prediction of heat transfer in air-cooled disc-type electrical machines," *IEEE Trans Ind Appl*, vol. 47, no. 4, pp. 1716–1723, 2011.

[43]   C. Debruyne, B. Corne, P. Sergeant, J. Desmet, and L. Vandevelde, "Evaluation of the additional loss due to supply voltage distortion in relation to induction motor efficiency rating," in *2015 IEEE International Electric Machines & Drives*

Conference (IEMDC), 2015, pp. 1881–1887. doi: 10.1109/IEMDC.2015.7409321.

[44]   D. Gerling, "Approximate analytical calculation of the skin effect in rectangular wires," in *2009 International Conference on Electrical Machines and Systems*, IEEE, Nov. 2009, pp. 1–6. doi: 10.1109/ICEMS.2009.5382786.

[45]   P. Silvester, "The Accurate Calculation of Skin Effect in Conductors of Complicated Shape," *IEEE Transactions on Power Apparatus and Systems*, vol. PAS-87, no. 3, pp. 735–742, Mar. 1968, doi: 10.1109/TPAS.1968.292187.

[46]   R. Wrobel, A. Mlot, and P. H. Mellor, "Contribution of end-winding proximity losses to temperature variation in electromagnetic devices," *IEEE Transactions on Industrial Electronics*, vol. 59, no. 2, pp. 848–857, Feb. 2012, doi: 10.1109/TIE.2011.2148686.

[47]   Q. Chen and X. Yang, "Calculation analysis of thermal loss and temperature field of in-wheel motor in micro-electric vehicle," *Journal of Mechanical Science and Technology*, vol. 28, no. 8, pp. 3189–3195, 2014, doi: 10.1007/s12206-014-0728-8.

[48]   G. Du, W. Xu, J. Zhu, and N. Huang, "Power loss and thermal analysis for high-power high-speed permanent magnet machines," *IEEE Transactions on Industrial Electronics*, vol. 67, no. 4, pp. 2722–2733, Apr. 2020, doi: 10.1109/TIE.2019.2908594.

[49]   N. Simpson and P. H. Mellor, "Additive manufacturing of shaped profile windings for minimal AC loss in gapped inductors," in *2017 IEEE International Electric Machines and Drives Conference, IEMDC 2017*, Institute of Electrical and Electronics Engineers Inc., Aug. 2017. doi: 10.1109/IEMDC.2017.8002337.

[50]   D. Winterborne, S. Jordan, L. Sjoberg, and G. Atkinson, "Estimation of AC copper loss in electrical machine windings with consideration of end effects," in *Proceedings - 2020 International Conference on Electrical Machines, ICEM 2020*, Institute of Electrical and Electronics Engineers Inc., Aug. 2020, pp. 847–853. doi: 10.1109/ICEM49940.2020.9270816.

[51]   A. Tessarolo, F. Agnolet, F. Luise, and M. Mezzarobba, "Use of time-harmonic finite-element analysis to compute stator winding eddy-current losses due to rotor motion in surface permanent-magnet machines," *IEEE Transactions on Energy Conversion*, vol. 27, no. 3, pp. 670–679, 2012, doi: 10.1109/TEC.2012.2192498.

[52]   G. Volpe, M. Popescu, F. Marignetti, and J. Goss, "AC Winding Losses in Automotive Traction E-Machines: A New Hybrid Calculation Method," in *2019 IEEE International Electric Machines & Drives Conference (IEMDC)*, IEEE, May 2019, pp. 2115–2119. doi: 10.1109/IEMDC.2019.8785409.

[53]   A. Fatemi, D. M. Ionel, N. A. O. Demerdash, D. A. Staton, R. Wrobel, and Y. C. Chong, "Computationally efficient strand eddy current loss calculation in electric machines," in *IEEE Transactions on Industry Applications*, Institute of Electrical and Electronics Engineers Inc., Jul. 2019, pp. 3479–3489. doi: 10.1109/TIA.2019.2903406.

[54]   T. El Hajji, S. Hlioui, F. Louf, M. Gabsi, G. Mermaz-Rollet, and M. Belhadi, "Hybrid model for AC Losses in High Speed PMSM for arbitrary flux density waveforms,"

in *2020 International Conference on Electrical Machines (ICEM)*, IEEE, Aug. 2020, pp. 2426–2432. doi: 10.1109/ICEM49940.2020.9271017.

[55]   X. Fan, D. Li, W. Kong, L. Cao, R. Qu, and Z. Yin, "Fast Calculation of Strand Eddy Current Loss in Inverter-Fed Electrical Machines," *IEEE Transactions on Industrial Electronics*, vol. 70, no. 5, pp. 4640–4650, May 2023, doi: 10.1109/TIE.2022.3183338.

[56]   P. L. Dowell, "Effects of eddy currents in transformer windings," *Proceedings of the Institution of Electrical Engineers*, vol. 113, no. 8, p. 1387, 1966, doi: 10.1049/piee.1966.0236.

[57]   R. P. Wojda and M. K. Kazimierczuk, "Analytical Optimization of Solid–Round-Wire Windings," *IEEE Transactions on Industrial Electronics*, vol. 60, no. 3, pp. 1033–1041, Mar. 2013, doi: 10.1109/TIE.2012.2189543.

[58]   D. Whitman and M. K. Kazimierczuk, "An Analytical Correction to Dowell's Equation for Inductor and Transformer Winding Losses Using Cylindrical Coordinates," *IEEE Trans Power Electron*, vol. 34, no. 11, pp. 10425–10432, Nov. 2019, doi: 10.1109/TPEL.2019.2904582.

[59]   H. Hämäläinen, J. Pyrhonen, and J. Nerg, "AC resistance factor in one-layer form-wound winding used in rotating electrical machines," *IEEE Trans Magn*, vol. 49, no. 6, pp. 2967–2973, 2013, doi: 10.1109/TMAG.2013.2240008.

[60]   C. R. Sullivan, "Computationally efficient winding loss calculation with multiple windings, arbitrary waveforms, and two-dimensional or three-dimensional field geometry," *IEEE Trans Power Electron*, vol. 16, no. 1, pp. 142–150, Jan. 2001, doi: 10.1109/63.903999.

[61]   M. Spang and M. Albach, "Optimized Winding Layout for Minimized Proximity Losses in Coils With Rod Cores," *IEEE Trans Magn*, vol. 44, no. 7, pp. 1815–1821, 2008, doi: 10.1109/TMAG.2008.920149.

[62]   H. Shinagawa, T. Suzuki, M. Noda, Y. Shimura, S. Enoki, and T. Mizuno, "Theoretical Analysis of AC Resistance in Coil Using Magnetoplated Wire," *IEEE Trans Magn*, vol. 45, no. 9, pp. 3251–3259, 2009, doi: 10.1109/TMAG.2009.2021948.

[63]   A.-T. Phung, G. Meunier, O. Chadebec, X. Margueron, and J.-P. Keradec, "High-Frequency Proximity Losses Determination for Rectangular Cross-Section Conductors," *IEEE Trans Magn*, vol. 43, no. 4, pp. 1213–1216, 2007, doi: 10.1109/TMAG.2007.892303.

[64]   A. D. Podoltsev, I. N. Kucheryavaya, and B. B. Lebedev, "Analysis of effective resistance and eddy-current losses in multiturn winding of high-frequency magnetic components," *IEEE Trans Magn*, vol. 39, no. 1, pp. 539–548, 2003, doi: 10.1109/TMAG.2002.806337.

[65]   A. S. Thomas, Z. Q. Zhu, and G. W. Jewell, "Proximity Loss Study In High Speed Flux-Switching Permanent Magnet Machine," *IEEE Trans Magn*, vol. 45, no. 10, pp. 4748–4751, 2009, doi: 10.1109/TMAG.2009.2021666.

[66]   P. B. Reddy, Z. Q. Zhu, S.-H. Han, and T. M. Jahns, "Strand-level proximity losses in PM machines designed for high-speed operation," in *2008 18th International Conference on Electrical Machines*, IEEE, Sep. 2008, pp. 1–6. doi:

10.1109/ICELMACH.2008.4800172.

[67] L. J. Wu and Z. Q. Zhu, "Simplified analytical model and investigation of open-circuit AC winding loss of permanent-magnet machines," *IEEE Transactions on Industrial Electronics*, vol. 61, no. 9, pp. 4990–4999, 2014, doi: 10.1109/TIE.2013.2272284.

[68] F. Birnkammer, J. Chen, D. B. Pinhal, and D. Gerling, "Influence of the Modeling Depth and Voltage Level on the AC Losses in Parallel Conductors of a Permanent Magnet Synchronous Machine," *IEEE Transactions on Applied Superconductivity*, vol. 28, no. 3, Apr. 2018, doi: 10.1109/TASC.2018.2801292.

[69] A. Lehikoinen and A. Arkkio, "Efficient Finite-Element Computation of Circulating Currents in Thin Parallel Strands," *IEEE Trans Magn*, vol. 52, no. 3, Mar. 2016, doi: 10.1109/TMAG.2015.2481934.

[70] L. Li *et al.*, "A Computationally Efficient Semi-Analytical Method for Circulating Current Loss of High Speed Permanent Magnet Machines," *IEEE Transactions on Energy Conversion*, 2023, doi: 10.1109/TEC.2023.3312648.

[71] M. Van Der Geest, H. Polinder, J. A. Ferreira, and D. Zeilstra, "Current sharing analysis of parallel strands in low-voltage high-speed machines," *IEEE Transactions on Industrial Electronics*, vol. 61, no. 6, pp. 3064–3070, 2014, doi: 10.1109/TIE.2013.2251741.

[72] Y. Jiang, J. Chen, X. Teng, and D. Wang, "Circulating current analysis for high-speed motors with stranded windings by considering end and temperature effect," *Journal of Magnetics*, vol. 23, no. 4, pp. 659–664, Dec. 2018, doi: 10.4283/JMAG.2018.23.4.659.

[73] Y. Jiang, Y. Guo, Q. Yang, J. Chen, K. Bo, and D. Wang, "A Computationally Efficient Method for Modelling of Circulating Current Loss in Electrical Machines with Stranded Windings," in *2022 IEEE 20th Biennial Conference on Electromagnetic Field Computation-Long Papers, CEFC-LONG 2022 - Proceedings*, Institute of Electrical and Electronics Engineers Inc., 2022. doi: 10.1109/CEFC-LONG57069.2022.10107549.

[74] Y. Jiang, J. Chen, H. Wang, and D. Wang, "Semi-Analytical Method of Form-Wound Winding Loss Considering Circulating Current Effect," *IEEE Trans Magn*, vol. 58, no. 2, Feb. 2022, doi: 10.1109/TMAG.2021.3086265.

[75] D. Golovanov and C. Gerada, "Analytical Methodology for Modelling of Circulating Current Loss in Synchronous Electrical Machines with Permanent Magnets," *IEEE Transactions on Energy Conversion*, vol. 37, no. 1, pp. 220–231, Mar. 2022, doi: 10.1109/TEC.2021.3091811.

[76] D. Golovanov, A. Galassini, T. Transi, and C. Gerada, "Analytical Methodology for Eddy Current Loss Simulation in Armature Windings of Synchronous Electrical Machines With Permanent Magnets," *IEEE Transactions on Industrial Electronics*, vol. 69, no. 10, pp. 9761–9770, Oct. 2022, doi: 10.1109/TIE.2022.3161818.

[77] X. Bian, Y. Zhao, and Y. Liang, "Electromagnetic Network Method for Transient Circulating Current Calculation of Stator Transposition Windings in Large Synchronous Compensator Based on Equivalence of Local Magnetic Field," *IEEE*

Transactions on Energy Conversion, vol. 37, no. 3, pp. 1825–1833, Sep. 2022, doi: 10.1109/TEC.2022.3146321.

[78]   F. Chai, Z. Li, and Y. Yu, "Analysis of AC Losses in High-Speed Permanent Magnet Motors Based on the Equivalent Modeling Method," in *2018 XIII International Conference on Electrical Machines (ICEM)*, IEEE, Sep. 2018, pp. 1061–1066. doi: 10.1109/ICELMACH.2018.8506900.

[79]   F. Jiancheng, L. Xiquan, B. Han, and K. Wang, "Analysis of circulating current loss for high-speed permanent magnet motor," *IEEE Trans Magn*, vol. 51, no. 1, Jan. 2015, doi: 10.1109/TMAG.2014.2302412.

[80]   C. R. Sullivan and R. Y. Zhang, "Simplified design method for litz wire," in *2014 IEEE Applied Power Electronics Conference and Exposition - APEC 2014*, IEEE, Mar. 2014, pp. 2667–2674. doi: 10.1109/APEC.2014.6803681.

[81]   H. Rossmanith, M. Doebroenti, M. Albach, and D. Exner, "Measurement and characterization of high frequency losses in nonideal litz wires," *IEEE Trans Power Electron*, vol. 26, no. 11, pp. 3386–3394, 2011, doi: 10.1109/TPEL.2011.2143729.

[82]   J. Lyu, H. Chen, Y. Zhang, Y. Du, and Q. S. Cheng, "Fast Simulation of Litz Wire Using Multilevel PEEC Method," *IEEE Trans Power Electron*, vol. 35, no. 12, pp. 12612–12616, Dec. 2020, doi: 10.1109/TPEL.2020.2991483.

[83]   C. R. Sullivan, "Optimal choice for number of strands in a litz-wire transformer winding," *IEEE Trans Power Electron*, vol. 14, no. 2, pp. 283–291, Mar. 1999, doi: 10.1109/63.750181.

[84]   P. B. Reddy, T. M. Jahns, and T. P. Bohn, "Transposition effects on bundle proximity losses in high-speed PM machines," in *2009 IEEE Energy Conversion Congress and Exposition, ECCE 2009*, 2009, pp. 1919–1926. doi: 10.1109/ECCE.2009.5316037.

[85]   C. R. Sullivan, J. D. McCurdy, and R. A. Jensen, "Analysis of minimum cost in shape-optimized Litz-wire inductor windings," in *2001 IEEE 32nd Annual Power Electronics Specialists Conference (IEEE Cat. No.01CH37230)*, 2001, pp. 1473–1478 vol. 3. doi: 10.1109/PESC.2001.954327.

[86]   M. van der Geest, H. Polinder, J. A. Ferreira, and D. Zeilstra, "Stator winding proximity loss reduction techniques in high speed electrical machines," in *2013 International Electric Machines & Drives Conference*, IEEE, May 2013, pp. 340–346. doi: 10.1109/IEMDC.2013.6556273.

[87]   S. Nategh, S. Ovrebo, S. Mahdavi, and O. Wallmark, "Thermal modeling of a permanent magnet machine built using Litz wire," in *2015 International Conference on Electrical Systems for Aircraft, Railway, Ship Propulsion and Road Vehicles (ESARS)*, IEEE, Mar. 2015, pp. 1–6. doi: 10.1109/ESARS.2015.7101462.

[88]   X. Yi, T. Yang, J. Xiao, N. Miljkovic, W. P. King, and K. S. Haran, "Equivalent Thermal Conductivity Prediction of Form-Wound Windings with Litz Wire including Transposition Effects," *IEEE Trans Ind Appl*, vol. 57, no. 2, pp. 1440–1449, Mar. 2021, doi: 10.1109/TIA.2021.3053500.

[89]   T. Dimier, M. Cossale, and T. Wellerdieck, "Comparison of stator winding

technologies for high-speed motors in electric propulsion systems," *Proceedings - 2020 International Conference on Electrical Machines, ICEM 2020*, pp. 2406–2412, Aug. 2020, doi: 10.1109/ICEM49940.2020.9270943.

[90] H. C. Born *et al.*, "Development of a Production Process for Formed Litz Wire Stator Windings," in *2022 12th International Electric Drives Production Conference, EDPC 2022 - Proceedings*, Institute of Electrical and Electronics Engineers Inc., 2022. doi: 10.1109/EDPC56367.2022.10019746.

[91] A. Selema, M. N. Ibrahim, and P. Sergeant, "Electrical Machines Winding Technology: Latest Advancements for Transportation Electrification," Jul. 01, 2022, *MDPI*. doi: 10.3390/machines10070563.

[92] H. Sugimoto, Y. Yamada, and K. Imae, "Analysis of Winding AC Loss in a Permanent Magnet Synchronous Machine With High Slot Fill Aluminum Winding," in *2022 International Power Electronics Conference (IPEC-Himeji 2022- ECCE Asia)*, IEEE, May 2022, pp. 2741–2745. doi: 10.23919/IPEC-Himeji2022-ECCE53331.2022.9807088.

[93] J. D. Widmer, C. M. Spargo, G. J. Atkinson, and B. C. Mecrow, "Solar plane propulsion motors with Precompressed aluminum stator windings," *IEEE Transactions on Energy Conversion*, vol. 29, no. 3, pp. 681–688, 2014, doi: 10.1109/TEC.2014.2313642.

[94] C. R. Sullivan, "Aluminum windings and other strategies for high-frequency magnetics design in an era of high copper and energy costs," *IEEE Trans Power Electron*, vol. 23, no. 4, pp. 2044–2051, Jul. 2008, doi: 10.1109/TPEL.2008.925434.

[95] M. Popescu, J. Goss, D. A. Staton, D. Hawkins, Y. C. Chong, and A. Boglietti, "Electrical Vehicles - Practical Solutions for Power Traction Motor Systems," in *IEEE Transactions on Industry Applications*, Institute of Electrical and Electronics Engineers Inc., May 2018, pp. 2751–2762. doi: 10.1109/TIA.2018.2792459.

[96] J. D. Widmer, R. Martin, and B. C. Mecrow, "Precompressed and Stranded Aluminum Motor Windings for Traction Motors," *IEEE Trans Ind Appl*, vol. 52, no. 3, pp. 2215–2223, May 2016, doi: 10.1109/TIA.2016.2528226.

[97] R. Wrobel and B. Mecrow, "Additive Manufacturing in Construction of Electrical Machines – A Review," in *2019 IEEE Workshop on Electrical Machines Design, Control and Diagnosis (WEMDCD)*, 2019, pp. 15–22. doi: 10.1109/WEMDCD.2019.8887765.

[98] A. Selema, M. N. Ibrahim, and P. Sergeant, "Metal Additive Manufacturing for Electrical Machines: Technology Review and Latest Advancements," Feb. 01, 2022, *MDPI*. doi: 10.3390/en15031076.

[99] H. Tiismus, A. Kallaste, T. Vaimann, and A. Rassõlkin, "State of the art of additively manufactured electromagnetic materials for topology optimized electrical machines," Jul. 01, 2022, *Elsevier B.V.* doi: 10.1016/j.addma.2022.102778.

[100] F. Wu and A. M. EL-Refaie, "Additively Manufactured Hollow Conductors with Integrated Cooling for High Specific Power Electrical Machines," in *2020 International Conference on Electrical Machines (ICEM)*, IEEE, Aug. 2020, pp.

1497–1503. doi: 10.1109/ICEM49940.2020.9270871.

[101] F. Wu, A. M. El-Refaie, and A. Al-Qarni, "Additively Manufactured Hollow Conductors for High Specific Power Electrical Machines: Aluminum vs Copper," in *2021 IEEE Energy Conversion Congress and Exposition, ECCE 2021 - Proceedings*, Institute of Electrical and Electronics Engineers Inc., 2021, pp. 4397–4404. doi: 10.1109/ECCE47101.2021.9595470.

[102] C. Wohlers, P. Juris, S. Kabelac, and B. Ponick, "Design and direct liquid cooling of tooth-coil windings," *Electrical Engineering*, vol. 100, no. 4, pp. 2299–2308, Dec. 2018, doi: 10.1007/s00202-018-0704-x.

[103] N. Simpson, D. J. North, S. M. Collins, and P. H. Mellor, "Additive Manufacturing of Shaped Profile Windings for Minimal AC Loss in Electrical Machines," *IEEE Trans Ind Appl*, vol. 56, no. 3, pp. 2510–2519, May 2020, doi: 10.1109/TIA.2020.2975763.

[104] S. Ayat, N. Simpson, B. Daguse, J. Rudolph, F. Lorenz, and D. Drury, "Design of Shaped-Profile Electrical Machine Windings for Multi-Material Additive Manufacture," in *2020 International Conference on Electrical Machines (ICEM)*, IEEE, Aug. 2020, pp. 1554–1559. doi: 10.1109/ICEM49940.2020.9270945.

[105] R. Wrobel and B. Mecrow, "A Comprehensive Review of Additive Manufacturing in Construction of Electrical Machines," *IEEE Transactions on Energy Conversion*, vol. 35, no. 2, pp. 1054–1064, Jun. 2020, doi: 10.1109/TEC.2020.2964942.

[106] I. Petrov, M. Polikarpova, P. Ponomarev, P. Lindh, and J. Pyrhonen, "Investigation of additional AC losses in tooth-coil winding PMSM with high electrical frequency," in *Proceedings - 2016 22nd International Conference on Electrical Machines, ICEM 2016*, Institute of Electrical and Electronics Engineers Inc., Nov. 2016, pp. 1841–1846. doi: 10.1109/ICELMACH.2016.7732774.

[107] D. Bauer, P. Mamuschkin, H. C. Reuss, and E. Nolle, "Influence of parallel wire placement on the AC copper losses in electrical machines," in *Proceedings - 2015 IEEE International Electric Machines and Drives Conference, IEMDC 2015*, Institute of Electrical and Electronics Engineers Inc., Feb. 2016, pp. 1247–1253. doi: 10.1109/IEMDC.2015.7409221.

[108] A. Bardalai *et al.*, "Reduction of Winding AC Losses by Accurate Conductor Placement in High Frequency Electrical Machines," in *IEEE Transactions on Industry Applications*, Institute of Electrical and Electronics Engineers Inc., Jan. 2020, pp. 183–193. doi: 10.1109/TIA.2019.2947552.

[109] J. Liu, X. Fan, D. Li, R. Qu, and H. Fang, "Minimization of AC Copper Loss in Permanent Magnet Machines by Transposed Coil Connection," *IEEE Trans Ind Appl*, vol. 57, no. 3, pp. 2460–2470, May 2021, doi: 10.1109/TIA.2021.3066966.

[110] X. Chen, H. Fang, X. Fan, H. Hu, D. Li, and R. Qu, "Suppression of Winding AC Copper Loss in High-Speed Electrical Machines by a Practical Transposition Technique," in *IEEE Transactions on Industry Applications*, Institute of Electrical and Electronics Engineers Inc., 2022, pp. 7121–7130. doi: 10.1109/TIA.2022.3193904.

[111] J. Hoole, P. H. Mellor, and N. Simpson, "Designing for Conductor Lay and AC Loss Variability in Multistrand Stator Windings," *IEEE Trans Ind Appl*, vol. 59, no.

2, pp. 1394–1404, Mar. 2023, doi: 10.1109/TIA.2022.3202762.

[112] D. A. Gonzalez and D. M. Saban, "Study of the copper losses in a high-speed permanent-magnet machine with form-wound windings," *IEEE Transactions on Industrial Electronics*, vol. 61, no. 6, pp. 3038–3045, 2014, doi: 10.1109/TIE.2013.2262759.

[113] J. Haldemann, "Transpositions in stator bars of large turbogenerators," *IEEE Transactions on Energy Conversion*, vol. 19, no. 3, pp. 553–560, Sep. 2004, doi: 10.1109/TEC.2004.832067.

[114] D. Wang, Y. Liang, L. Gao, X. Bian, and C. Wang, "A New Global Transposition Method of Stator Winding and Its Loss Calculation in AC Machines," *IEEE Transactions on Energy Conversion*, vol. 35, no. 1, pp. 149–156, Mar. 2020, doi: 10.1109/TEC.2019.2947082.

[115] M. Fujita, Y. Kabata, T. Tokumasu, K. Nagakura, M. Kakiuchi, and S. Nagano, "Circulating currents in stator coils of large turbine generators and loss reduction," *IEEE Trans Ind Appl*, vol. 45, no. 2, pp. 685–693, 2009, doi: 10.1109/TIA.2009.2013572.

[116] Y. Zhao, D. Li, T. Pei, and R. Qu, "Overview of the rectangular wire windings AC electrical machine," *CES Transactions on Electrical Machines and Systems*, vol. 3, no. 2, pp. 160–169, Jun. 2019, doi: 10.30941/cestems.2019.00022.

[117] T. Zou *et al.*, "A Comprehensive Design Guideline of Hairpin Windings for High Power Density Electric Vehicle Traction Motors," *IEEE Transactions on Transportation Electrification*, vol. 8, no. 3, pp. 3578–3593, Sep. 2022, doi: 10.1109/TTE.2022.3149786.

[118] X. Ju, Y. Cheng, B. Du, M. Yang, D. Yang, and S. Cui, "AC Loss Analysis and Measurement of a Hybrid Transposed Hairpin Winding for EV Traction Machines," *IEEE Transactions on Industrial Electronics*, vol. 70, no. 4, pp. 3525–3536, Apr. 2023, doi: 10.1109/TIE.2022.3179571.

[119] E. Preci *et al.*, "Segmented Hairpin Topology for Reduced Losses at High-Frequency Operations," *IEEE Transactions on Transportation Electrification*, vol. 8, no. 1, pp. 688–698, Mar. 2022, doi: 10.1109/TTE.2021.3103821.

[120] C. J. Carpenter, "Magnetic equivalent circuits," *Proceedings of the Institution of Electrical Engineers*, vol. 115, no. 10, p. 1503, 1968, doi: 10.1049/piee.1968.0265.

[121] V. Ostović, *Dynamics of Saturated Electric Machines*. New York, NY: Springer New York, 1989. doi: 10.1007/978-1-4613-8933-0.

[122] L. Ding, G. Liu, Q. Chen, and G. Xu, "A Novel Mesh-Based Equivalent Magnetic Network for Performance Analysis and Optimal Design of Permanent Magnet Machines," *IEEE Transactions on Energy Conversion*, vol. 34, no. 3, pp. 1337–1346, 2019, doi: 10.1109/TEC.2019.2900263.

[123] Z. P. Xia, Z. Q. Zhu, and D. Howe, "Analytical magnetic field analysis of halbach magnetized permanent-magnet machines," *IEEE Trans Magn*, vol. 40, no. 4 I, pp. 1864–1872, Jul. 2004, doi: 10.1109/TMAG.2004.828933.

[124] L. Ding, G. Liu, Q. Chen, and G. Xu, "A Novel Mesh-Based Equivalent Magnetic Network for Performance Analysis and Optimal Design of Permanent Magnet Machines," *IEEE Transactions on Energy Conversion*, vol. 34, no. 3, pp. 1337–

1346, Sep. 2019, doi: 10.1109/TEC.2019.2900263.

[125] Y. Yuan, M. A. Darmani, Y. Bao, X. Zhang, D. Gerada, and H. Zhang, "Analysis of Proximity Loss of Electrical Machines Using Mesh-Based Magnetic Equivalent Circuit," *IEEE Transactions on Transportation Electrification*, p. 1, 2024, doi: 10.1109/TTE.2024.3383845.

[126] A. Hemeida and P. Sergeant, "Analytical modeling of surface PMSM using a combined solution of Maxwell-s equations and magnetic equivalent circuit," *IEEE Trans Magn*, vol. 50, no. 12, Dec. 2014, doi: 10.1109/TMAG.2014.2330801.

[127] P. Kumar and P. Bauer, "Improved analytical model of a permanent-magnet brushless DC motor," *IEEE Trans Magn*, vol. 44, no. 10, pp. 2299–2309, Oct. 2008, doi: 10.1109/TMAG.2008.2001450.

[128] E. Preci *et al.*, "Experimental Statistical Method Predicting AC Losses on Random Windings and PWM Effect Evaluation," *IEEE Transactions on Energy Conversion*, vol. 36, no. 3, pp. 2287–2296, Sep. 2021, doi: 10.1109/TEC.2020.3040265.